NOAA Technical Report NOS CS 13

DEVELOPMENT OF AN EAST COAST WATER LEVEL DATA ASSIMILATION MODEL

Silver Spring, Maryland
March 2002

noaa National Oceanic and Atmospheric Administration

U.S. DEPARTMENT OF COMMERCE
National Ocean Service
Coast Survey Development Laboratory

Office of Coast Survey
National Ocean Service
National Oceanic and Atmospheric Administration
U.S. Department of Commerce

The Office of Coast Survey (CS) is the Nation's only official chartmaker. As the oldest United States scientific organization, dating from 1807, this office has a long history. Today it promotes safe navigation by managing the National Oceanic and Atmospheric Administration's (NOAA) nautical chart and oceanographic data collection and information programs.

There are four components of CS:

> The Coast Survey Development Laboratory develops new and efficient techniques to accomplish Coast Survey missions and to produce new and improved products and services for the maritime community and other coastal users.
>
> The Marine Chart Division collects marine navigational data to construct and maintain nautical charts, Coast Pilots, and related marine products for the United States.
>
> The Hydrographic Surveys Division directs programs for ship and shore-based hydrographic survey units and conducts general hydrographic survey operations.
>
> The Navigation Services Division is the focal point for Coast Survey customer service activities, concentrating predominantly on charting issues, fast-response hydrographic surveys and Coast Pilot updates.

NOAA Technical Report NOS CS 13

DEVELOPMENT OF AN EAST COAST WATER LEVEL DATA ASSIMILATION MODEL

Aijun Zhang
Bruce B. Parker
Eugene Wei

March 2002

noaa National Oceanic and Atmospheric Administration

U.S. DEPARTMENT
OF COMMERCE
Donald Evans, Secretary

Office of Coast Survey
Captain David MacFarland

National Oceanic and
Atmospheric Administration
Conrad C . Lautenbacher, Jr.,
VADM USN (Ret.), Under Secretary

National Ocean Service
Margaret A. Davidson
Acting Assistant Administrator

Coast Survey Development
Laboratory
Bruce B. Parker

NOTICE

TABLE OF CONTENTS

LIST OF FIGURES

LIST OF TABLES

EXECUTIVE SUMMARY

An East Coast Data Assimilation (ECDA) model based on the two-dimensional Princeton Ocean Model (POM) with orthogonal curvilinear grid has been developed. The primary objective of ECDA is to simulate water levels along the east coast and provide optimal open boundary conditions for the regional and estuarine nowcast/forecast systems. In ECDA, cost function is defined with differences between the simulated water levels and observations along the coastal water level gauge stations. Elevations along the open ocean boundary and surface wind drag coefficients are chosen as the control variables. An adjoint approach is used to calculate the gradient of the cost function. The limited memory Broyden-Fletcher-Goldfarb-Shannon(BFGS) quasi-Newton method is then used to minimize the cost function. The tidal open boundary conditions are determined by assimilating tidal predictions at the coastal stations. The wind drag coefficients are estimated by assimilating either observed subtidal water levels or total water levels at coastal stations. The Eta Data Assimilation (EDAS) analyzed surface winds are used in nowcast model runs and Eta wind forecasts are used in forecast model runs.

The results for the following experiments are presented:

Identical Twin Experiments:

In the identical twin experiment, the pseudo-observations were generated by the numerical model with a set of predetermined control variables. The twin experiments of recovering the "true" tidal boundary conditions and the "true" wind drag coefficients were performed, respectively. The results show that the pseudo "true" tidal open boundary conditions and the pseudo "true" wind drag coefficients can be successfully recovered by this system through assimilating water level observations along the coast. The water level observational errors inhibit the optimal control variables from converging to their true solution. The number and spatial distribution of the observations also affect the results of optimization process. The optimal tidal open boundary conditions can be determined by assimilating water levels from 9 coastal stations.

Optimal Tidal Open Boundary Conditions:

Elevations of 5 major tidal constituents (M_2, S_2, N_2, K_1, O_1) along the open boundary are estimated by assimilating tidal predictions from 9 coastal stations with individual and combined methods. Similar results were obtained from the two methods but the combined method is more efficient than the individual method. Using data assimilation to compute the optimal tidal forcing along the boundary led to better results than using the tidal open boundary conditions from Schwiderski's global model. For this case, RMS errors at coastal stations are less than 5 cm.

Subtidal Water Level Nowcasts:

Subtidal water level nowcast experiments with one, eight, and sixteen control variables of the wind drag coefficients (C_d) and with/without penalty terms were performed in which surface wind drag coefficients were computed by assimilating observed subtidal water levels. The results showed that the simulated subtidal water levels were improved even with one control variable. The most accurate simulated subtidal water levels were obtained with 16 control variables (using x- and y-direction pairs in 8 regions). In this case, the correlation coefficients at 18 stations were greater than 0.93, and the RMS errors were less than 5.3 cm. Both the magnitude and direction of the wind stress need to be adjusted in order to minimize the cost function. Penalty terms should also be included in the cost function to assure the smoothness of the estimated optimal wind drag coefficient in space and time. Results from the experiments with the penalty terms indicate that the estimated optimal values of C_d are smoother in space and time than those without the penalty terms. However, the RMS error differences between the simulated subtidal water levels with and without the penalty terms are very small. Thus, adding the penalty terms leads to smoother solutions that still preserve the physical features of subtidal water levels.

Subtidal Water Level Forecasts:

Followed subtidal water level nowcast experiments, subtidal water level forecasts are performed from the initial file generated from nowcast model to examine model performance of subtidal water level forecasts. The following five subtidal water level forecast experiments were performed:

SWL_F1:

No data assimilation was included in the nowcast mode. The wind drag coefficients for both the nowcast and forecast modes were calculated with the Large-Pond formulation (denoted as the baseline run or without data assimilation case).

SWL_F2:

A 24-hour water level data assimilation with 16 control variables and without penalty terms was performed in the nowcast mode to obtain optimal values of C_d. The wind drag coefficients are calculated with the Large and Pond formulation in the forecast mode.

SWL_F3:

Same experiment as SWL_F2 was performed in the nowcast mode, but the optimal values of C_d from the previous day's nowcast were applied to the next day's forecast.

SWL_F4:

A 24-hour water level data assimilation with 16 control variables and penalty terms was performed in the nowcast mode, and the wind drag coefficients are calculated with the Large and Pond formulation in the forecast mode.

SWL_F5:

Same experiment as SWL_F4 was performed in the nowcast mode, but the optimal values of C_d from the previous day's nowcast were applied to the next day's forecast.

The results demonstrated that most of the improvement in water level forecasts by applying water level data assimilation into the nowcast/forecast system occurred within the first 6 hours. The optimal values of C_d from the previous day's water level data assimilation cannot be directly applied in the next day's water level forecast due to changes in the surface wind field. These values can only be reasonably extended about 3-6 hours into the forecast.

Total Water Level Forecasts:
In practice, total water levels which include both astronomical tides and subtidal water levels can be directly measured by water level gauges. Total water levels are important and have direct impacts on the activities of people. Our ultimate goal is therefore to produce total water level forecast guidance. The following three experiments were performed to compute total water level forecasts:

TWL_F1:
The nowcast and forecast runs were forced along the open boundary with the optimal harmonic constants of M_2, S_2, N_2, K_1, and O_1 obtained from the data assimilation. The nowcast run was forced with EDAS surface winds and the forecast run was forced with ETA wind forecasts. The wind drag coefficients for both nowcast and forecast runs were calculated with the Large and Pond formulation.

TWL_F2:
The same tidal open boundary conditions as TWL_F1 were used to force both the nowcast and forecast runs. The nowcast run was forced by EDAS surface winds with the optimal wind drag coefficients obtained through the water level data assimilation. The forecast run was forced by ETA wind forecasts with wind drag coefficients calculated with the Large and Pond formulation.

TWL_F3:
At coastal stations, astronomical tides were calculated using harmonic tidal prediction and subtidal water level forecasts were obtained from experiment SWL_F4. Total water level forecasts were then derived by simply superimposing the simulated subtidal water level forecasts to the tidal predictions.

For total water level forecasts, the best results were obtained from TWL_F3 that simply adds the tidal predictions to the optimal simulated subtidal water levels. The average RMS errors of 24-hour water level forecasts over 18 stations vary from 10-16 cm, and the average correlation coefficients are greater than 0.96. However, such forecasts can only be made where observations are available. For the model forecasted total water levels (TWL_F2). The average RMS errors of the 24-hour forecasts are in the range of 12-22 cm, and the average correlation coefficients are greater than 0.94.

1. INTRODUCTION

Information of water levels and currents plays an important role in coastal management, exploitation and navigation (for example, maritime traffic, response to oil spills, fisheries, tourism, recreational sports). Two factors generally affect water level variation. The first factor is astronomical tides, produced by the gravitational attraction of the moon and sun acting upon the rotating earth. The second is nontidal water level variation which is primarily generated by the surface wind, but which also includes the effects of changing atmospheric pressure and changing water density (due to temperature and salinity variation). Astronomical tides can be predicted using either harmonic or response techniques. For over a century, mariners who needed information on water levels and currents have relied on astronomical tide and tidal current prediction tables. However, tide and tidal current prediction can not tell mariners what real water levels and currents will be in the future since they do not include the often important effects of wind, river flow, atmospheric pressure, or water density which sometimes may be significant and completely overwhelm the tidal signal. Real-time observing systems provide instant measured water level and current measurements and thus are more accurate than tidal predictions, but such information can not be extended into the future nor given at locations other than those that are instrumented.

Numerical models have been widely applied to simulations of ocean coastal circulation. Several ocean nowcast/forecast systems have been developed: Coastal Ocean Forecast System (Aikman et al., 1996); Experimental Real-Time North Pacific Ocean Nowcast/Forecast System (Kuo, personal communication); Chesapeake Bay Operational Forecast System (Gross et al., 2000); Lower Columbia River Nowcast/Forecast Systems (Baptista et al., 1998). Some Nowcast/Forecast estuary systems are under development and are running under experimental mode in Coast Survey Development Laboratory, National Ocean Service (Parker, 1998; Wei and Chen, 2001; Schmalz, 2000). These systems not only provide water level and current information at particular locations, but they also provide two-dimensional water level fields, and/or three-dimensional current fields. Numerical modeling can also help to understand the oceanographic physical dynamics of some special phenomena. However, even the highest resolution ocean circulation model cannot resolve all of the dynamically important physical processes in the ocean. There are always some processes that are not represented directly (Malanotte-Rizzoli and Tziperman, 1996), but rather are parameterized. These tunable parameterizations are always uncertain both in form and magnitude (i.e. eddy coefficients, wind drag coefficients, bottom friction coefficients, etc.). Many of the tunable parameters are often difficult to be directly measured or theoretically defined. Open boundary conditions play an important role in the accuracy of a regional tidal model. Solutions in the interior of the domain are uniquely determined by the open boundary conditions. Traditionally, tidal open boundary conditions can be obtained from either available observations near the open boundaries (tidal gauge data or satellite data) or from large-scale numerical models such as Schwiderski's global tidal model (Schwiderski, 1980) and TPX0.3 global tide model (Egbert et al., 1994). Unfortunately, the observations at open waters are often scarce, and global tidal model results are less accurate in shallow waters. Therefore, determination of the open boundary conditions can be the limiting factor in developing a regional tidal simulation. However, oceanographic data in the interior of the domain can be used to help estimate the tunable model parameters and boundary conditions. Combination of numerical model and observations for determination of the poorly known model parameters and for improvement of the ocean model performance can be formulated as an optimization problem. Such an optimization would search for a set of model parameters and for an optimal ocean state which together satisfy the model equations and fit the available data as well as possible. This may be done by formulating a cost function, which represents the differences between the model results and the observations. The cost function is then minimized with model governing equations as strong or weak constraints by adjusting the control variables using unconstrained optimization algorithms. These algorithms, such as the conjugate gradient method and the limited memory quasi-Newton method, require the gradients of the cost function with respect to the control variables. For a large number of control variables, computation of the gradients is computationally expensive and therefore needs to be carried out using efficient methods.

Adjoint technique provides an efficient method for gradient computation of the cost function. In recent years, the adjoint technique has been developed and widely applied in meteorological and oceanographic fields, especially for data assimilation, model tuning, model sensitivity analysis, and parameter estimation. As early as the 1970's, the adjoint approach with the governing equations as strong constraints was described by Sasaki (1970), who gave a framework that is readily applicable to a set of steady or unsteady state equations. Bennett and McIntosh (1982) and Bennett (1985) used the adjoint variational method to determine the open boundary conditions in tidal model and array design. Hall et al. (1982) and Cacuci (1988) used the adjoint method to estimate sensitivity of model forecasts to changes in boundary conditions and model parameters. Zou et al. (1993) examined the sensitivity of a blocking index in a two-layer primitive equation isentropic spectral model. Yu and O'Brien (1991, 1992) used the adjoint method in a one-dimensional vertical model to estimate the wind stress drag coefficient, the oceanic eddy viscosity profile, and initial conditions from observed velocity observations. Panchang and O'Brien (1989) applied the adjoint variational method to a one- dimensional hydraulic model to determine the bottom friction coefficients in a tidal river. Das and Lardner (1991) and Lardner (1993) implemented the adjoint method for a two-dimensional tidal model to determine the bottom friction coefficients, water depths and open boundary conditions from periodic tidal data. Similarly, Lardner et al. (1993) estimated the bottom drag coefficient and bathymetry correction for a two-dimensional tidal model of the Arabian Gulf. Lardner and Song (1995) used the adjoint method in the optimal estimation of viscosity and friction coefficients for a quasi-three dimensional numerical tidal model. Seiler (1993) used the adjoint method to estimate open boundary conditions for a quasi-geostrophic ocean model. These studies using the adjoint technique are mainly concerned with examining the method rather than applying it to operational nowcast/forecast system.

In this study, we describe the East Coast Data Assimilation (ECDA) model which has been developed using the adjoint technique with the two-dimensional Princeton Ocean Model (POM). The primary object of ECDA is to simulate water levels along the east coast and provide optimal open boundary conditions for the regional and estuarine nowcast/forecast systems. In ECDA model, an orthogonal curvilinear model grid system is implemented. Elevations along the open ocean boundary and surface wind drag coefficients are chosen as the control variables. An adjoint approach is used to calculate the gradient of the cost function, and a limited memory Broyden-Fletcher-Goldfarb-Shannon(BFGS) quasi-Newton method is then implemented to minimize the cost function. The tidal open boundary conditions are determined by assimilating tidal predictions at the coastal tide stations and wind drag coefficients are estimated by assimilating observed subtidal water level data at coastal tide stations.

Section 2 describes the two-dimensional POM, the model grid, and bathymetry. Derivation of the discrete adjoint equations for the two-dimensional POM is described in Section 3. In order to verify and evaluate the adjoint model, identical twin experiments are conducted in Section 4. The practical application of ECDA to water level data along the East Coast is described in Section 5.

2. FORWARD MODEL

The barotropic two-dimensional POM (Blumberg and Mellor, 1987; Mellor, 1996) is used to make the operational real-time water level nowcast/forecast system as efficient as possible since optimal adjoint data assimilation requires substantial computer resources to perform numerical computation. A 120×85 curvilinear grid (Figure 2.1) is used, with grid sizes ranging from 5 km in shallow regions to 32 km in deep regions. The discrete continuity and momentum equations are as follows,

$$h^n_{i,j} - \overline{h}^{n-1}_{i,j} + O_{i,j}\left(A_{i+1,j}U^{n-1}_{i+1,j} - A_{i,j}U^{n-1}_{i,j} + B_{i,j+1}V^{n-1}_{i,j+1} - B_{i,j}V^{n-1}_{i,j}\ \right) = 0 \tag{2.1}$$

$$\begin{aligned} &U^n_{i,j} - \overline{U}^{n-1}_{i,j} + L_{i,j}F_{x_{i,j}} - \frac{P_{i,j}}{4}\left[f_{i,j}H_{i,j}\left(V^{n-1}_{i,j} + V^{n-1}_{i,j+1}\right) + f_{i-1,j}H_{i-1,j}\left(V^{n-1}_{i-1,j+1} + V^{n-1}_{i-1,j}\right)\right] \\ &+ Q_{i,j}\left[(1-2\alpha)\left(h^{n-1}_{i,j} - h^{n-1}_{i-1,j}\right) + \alpha\left(h^n_{i,j} - h^n_{i-1,j} + \overline{h}^{n-1}_{i,j} - \overline{h}^{n-1}_{i-1,j} - P^n_{a_{i,j}} + P^n_{a_{i-1,j}}\right)\right] \\ &+ P_{i,j}(-10^{-6}Cd_{i,j}\left|W^n_{s_{i,j}}\right|W^n_{u_{i,j}} + C_{b_{i,j}}\sqrt{\overline{U}^{n-1^2}_{i,j} + \overline{V}^{n-1^2}_{i,j}}\,\overline{U}^{n-1}_{i,j}) = 0 \end{aligned} \tag{2.2}$$

$$\begin{aligned} &V^n_{i,j} - \overline{V}^{n-1}_{i,j} + M_{i,j}F_{y_{i,j}} + \frac{R_{i,j}}{4}\left[f_{i,j}H_{i,j}\left(U^{n-1}_{i,j} + U^{n-1}_{i+1,j}\right) + f_{i,j-1}H_{i,j-1}\left(U^{n-1}_{i+1,j-1} + U^{n-1}_{i,j-1}\right)\right] \\ &+ S_{i,j}\left[(1-2\alpha)\left(h^{n-1}_{i,j} - h^{n-1}_{i,j-1}\right) + \alpha\left(h^n_{i,j} - h^n_{i,j-1} + \overline{h}^{n-1}_{i,j} - \overline{h}^{n-1}_{i,j-1} - P^n_{a_{i,j}} + P^n_{a_{i,j-1}}\right)\right] \\ &+ R_{i,j}(-10^{-6}Cd_{i,j}\left|W^n_{s_{i,j}}\right|W^n_{v_{i,j}} + C_{b_{i,j}}\sqrt{\overline{U}^{n-1^2}_{i,j} + \overline{V}^{n-1^2}_{i,j}}\,\overline{V}^{n-1}_{i,j}) = 0 \end{aligned} \tag{2.3}$$

$$\overline{h}^n_{i,j} = h^{n-1}_{i,j} + 0.5\cdot\beta\cdot\left(h^n_{i,j} + \overline{h}^{n-1}_{i,j} - 2h^{n-1}_{i,j}\right) \tag{2.4}$$

$$\overline{U}^n_{i,j} = U^{n-1}_{i,j} + 0.5\cdot\beta\cdot\left(U^n_{i,j} + \overline{U}^{n-1}_{i,j} - 2U^{n-1}_{i,j}\right) \tag{2.5}$$

$$\overline{V}^n_{i,j} = V^{n-1}_{i,j} + 0.5\cdot\beta\cdot\left(V^n_{i,j} + \overline{V}^{n-1}_{i,j} - 2V^{n-1}_{i,j}\right) \tag{2.6}$$

where

$$\begin{aligned} F_{x_{i,j}} = &F_{1_{i,j}}\Delta y_{i,j} - F_{1_{i-1,j}}\Delta y_{i-1,j} + (F_{2_{i,j+1}} - F_{3_{i,j+1}})\Delta\overline{x}_{i,j+1} - (F_{2_{i,j}} - F_{3_{i,j}})\Delta\overline{x}_{i,j} \\ &- \frac{ARU_{i,j}}{4}\left[F_{6_{i,j}}H_{i,j}\left(V^{n-1}_{i,j+1} + V^{n-1}_{i,j}\right) + F_{6_{i-1,j}}H_{i-1,j}\left(V^{n-1}_{i-1,j+1} + V^{n-1}_{i-1,j}\right)\right] \end{aligned}$$

$$\begin{aligned} F_{y_{i,j}} = &F_{5_{i,j}}\Delta x_{i,j} - F_{5_{i,j-1}}\Delta x_{i,j-1} + (F_{4_{i+1,j}} - F_{3_{i+1,j}})\Delta\overline{y}_{i+1,j} - (F_{4_{i,j}} - F_{3_{i,j}})\Delta\overline{y}_{i,j} \\ &+ \frac{ARV_{i,j}}{4}\left[F_{6_{i,j}}H_{i,j}\left(U^{n-1}_{i+1,j} + U^{n-1}_{i,j}\right) + F_{6_{i,j-1}}H_{i,j-1}\left(U^{n-1}_{i+1,j-1} + U^{n-1}_{i,j-1}\right)\right] \end{aligned}$$

$$F_{1_{i,j}} = \frac{1}{8}\left[(H_{i+1,j} + H_{i,j})U^{n-1}_{i+1,j} + (H_{i,j} + H_{i-1,j})U^{n-1}_{i,j}\right]\left(U^{n-1}_{i+1,j} + U^{n-1}_{i,j}\right) - 2H_{i,j}A_M\frac{\overline{U}^{n-1}_{i+1,j} - \overline{U}^{n-1}_{i,j}}{\Delta x_{i,j}}$$

$$F_{2_{i,j}} = \frac{1}{8}\left[(H_{i,j} + H_{i,j-1})V^{n-1}_{i,j} + (H_{i-1,j} + H_{i-1,j-1})V^{n-1}_{i-1,j}\right]\left(U^{n-1}_{i,j} + U^{n-1}_{i,j-1}\right)$$

$$F_{3_{i,j}} = \overline{H}_{i,j}\overline{A}_M(\frac{\overline{U}^{n-1}_{i,j} - \overline{U}^{n-1}_{i,j-1}}{\Delta\overline{y}_{i,j}} + \frac{\overline{V}^{n-1}_{i,j} - \overline{V}^{n-1}_{i-1,j}}{\Delta\overline{x}_{i,j}})$$

$$F_{4_{i,j}} = \frac{1}{8}\left[(H_{i,j} + H_{i-1,j})U^{n-1}_{i,j} + (H_{i,j-1} + H_{i-1,j-1})U^{n-1}_{i,j-1}\right]\left(V^{n-1}_{i-1,j} + V^{n-1}_{i,j}\right)$$

$$F_{5_{i,j}} = \frac{1}{8}\left[(H_{i,j+1} + H_{i,j})V^{n-1}_{i,j+1} + (H_{i,j} + H_{i,j-1})V^{n-1}_{i,j}\right]\left(V^{n-1}_{i,j+1} + V^{n-1}_{i,j}\right) - 2H_{i,j}A_M\frac{\overline{V}^{n-1}_{i,j+1} - \overline{V}^{n-1}_{i,j}}{\Delta y_{i,j}}$$

$$F_{6_{i,j}} = \frac{1}{4\Delta x\Delta y}[\left(V^{n-1}_{i,j+1} + V^{n-1}_{i,j}\right)\left(\Delta y_{i+1,j} - \Delta y_{i-1,j}\right) - \left(U^{n-1}_{i+1,j} + U^{n-1}_{i,j}\right)\left(\Delta x_{i,j+1} - \Delta x_{i,j-1}\right)]$$

i and j are the horizontal grid index, and n is the index of integration time. *h*, *U* and *V* are the surface elevation and horizontal velocities, f is the Coriolis parameter, α and β are temporal smoothing parameters, H is the water depth at rest, C_b is the coefficient of bottom friction and C_d is the wind drag coefficient. W_s is the surface wind speed, and W_u and W_v are the wind components in i and j direction. P_a is surface atmospheric pressure. The other coefficients are defined as:

$$A_{i,j} = \frac{H_{i,j} + H_{i-1,j}}{2} \cdot \frac{\Delta y_{i,j} + \Delta y_{i-1,j}}{2} \text{ and } B_{i,j} = \frac{H_{i,j} + H_{i,j-1}}{2} \cdot \frac{\Delta x_{i,j} + \Delta x_{i,j-1}}{2}$$

$$O_{i,j} = \frac{2\Delta t}{ART_{i,j}} \quad P_{i,j} = \frac{4\Delta t}{H_{i,j} + H_{i-1,j}} \quad \textit{and} \quad Q_{i,j} = \frac{4g\Delta t A_{i,j}}{ARU_{i,j}\left(H_{i,j} + H_{i-1,j}\right)}$$

$$R_{i,j} = \frac{4\Delta t}{H_{i,j} + H_{i,j-1}} \quad \textit{and} \quad S_{i,j} = \frac{4g\Delta t B_{i,j}}{ARV_{i,j}\left(H_{i,j} + H_{i,j-1}\right)}$$

$$L_{i,j} = \frac{Q_{i,j}}{gA_{i,j}}, \quad M_{i,j} = \frac{S_{i,j}}{gB_{i,j}}$$

$$\overline{H}_{i,j} = \frac{H_{i,j} + H_{i-1,j} + H_{i,j-1} + H_{i-1,j-1}}{4}$$

$$\overline{A}_{M\,i,j} = \frac{A_{M\,i,j} + A_{M\,i-1,j} + A_{M\,i,j-1} + A_{M\,i-1,j-1}}{4}$$

$$\Delta\overline{x}_{i,j} = \frac{\Delta x_{i,j} + \Delta x_{i-1,j} + \Delta x_{i,j-1} + \Delta x_{i-1,j-1}}{4}$$

$$\Delta\overline{y}_{i,j} = \frac{\Delta y_{i,j} + \Delta y_{i-1,j} + \Delta y_{i,j-1} + \Delta y_{i-1,j-1}}{4}$$

where Δt is the model time step, and Δx and Δy are the model grid spacings, and g is the acceleration due to gravity. *ART*, *ARU*, and *ARV* are the area of a grid cell centered at a depth point, a U velocity point and a V velocity point, respectively. The open lateral boundary conditions are specified as, in subtidal simulation model,

$$h^n_{i,1} = h^n_{i,2} \tag{2.7}$$

in tidal simulation model for one tidal constituent,

$$h^n_{i,1} = \chi_i A_i \cos\left(\omega t^n + E_i - \Theta_i\right) \tag{2.8}$$

in which, i is grid index along the open boundary, χ_i is node factor, A_i is mean amplitude, Θ_i is epoch, ω is angular speed and E_i is value of equilibrium argument when t=0. Velocities are specified using a radiation open boundary formulation as,

$$V^n_{i,1} = -0.1\sqrt{\frac{g}{H_{i,2}}}\left(h^{n-1}_{i,1} - h^n_{i,1}\right), \quad V^n_{i,2} = V^n_{i,1} \tag{2.9}$$

$$U^n_{i,1} = U^{n-1}_{i,1} - \frac{(V^{n-1}_{i,2} - V^{n-1}_{i-1,2})\Delta t}{\Delta y_{i,1} + \Delta y_{i,2}}(U^{n-1}_{i,2} - U^{n-1}_{i,1}) \tag{2.10}$$

Figure 2.2 shows the bathymetry and tidal gauge locations which name are listed in Table 2.1. The bathymetry in the model domain is based on DBDB5(National Geophysical Data Center, 1985) 5 arcminute bathymetry data except in coastal regions (water depth less than 200m) where the NOS15 15 arcsecond (National Geophysical Data Center, 1988) bathymetry data is used because of better resolution and accuracy of bottom topography and coastal geometry. The model is driven by surface atmospheric pressure and ETA Data Assimilation System (EDAS) analyzed surface wind fields (Black, 1994; Rogers et al., 1995) that are bilinearly interpolated onto the model grid.

Table 2.1. The tidal gauge stations used in this study. The station number is used to identify the stations in Figure 2.2.

Station #	Station Name	Latitude	Longitude
1	Newport, RI	41.51	-71.33
2	New London, CT	41.36	-72.09
3	Bridgeport, CT	41.17	-73.18
4	Montauk, NY	41.05	-71.96
5	Willets Point, NY	40.79	-73.78
6	Sandy Hook, NJ	40.47	-74.00
7	Atlantic City, NJ	39.35	-74.42
8	Cape May, NJ	38.97	-74.96
9	Lewes, DE	38.78	-75.13
10	Gloucester, VA	37.25	-76.50
11	Chesapeake Bay Bridge Tunnel (CBBT), VA	36.97	-76.11
12	Duck, NC	36.18	-75.75
13	Cape Hatteras	35.22	-75.63
14	Springmaid, SC	33.66	-78.92
15	Charleston, SC	32.78	-79.93
16	Mayport, FL	30.39	-81.43
17	St. Augustine, FL	29.86	-81.26
18	Trident Pier, FL	28.42	-80.59

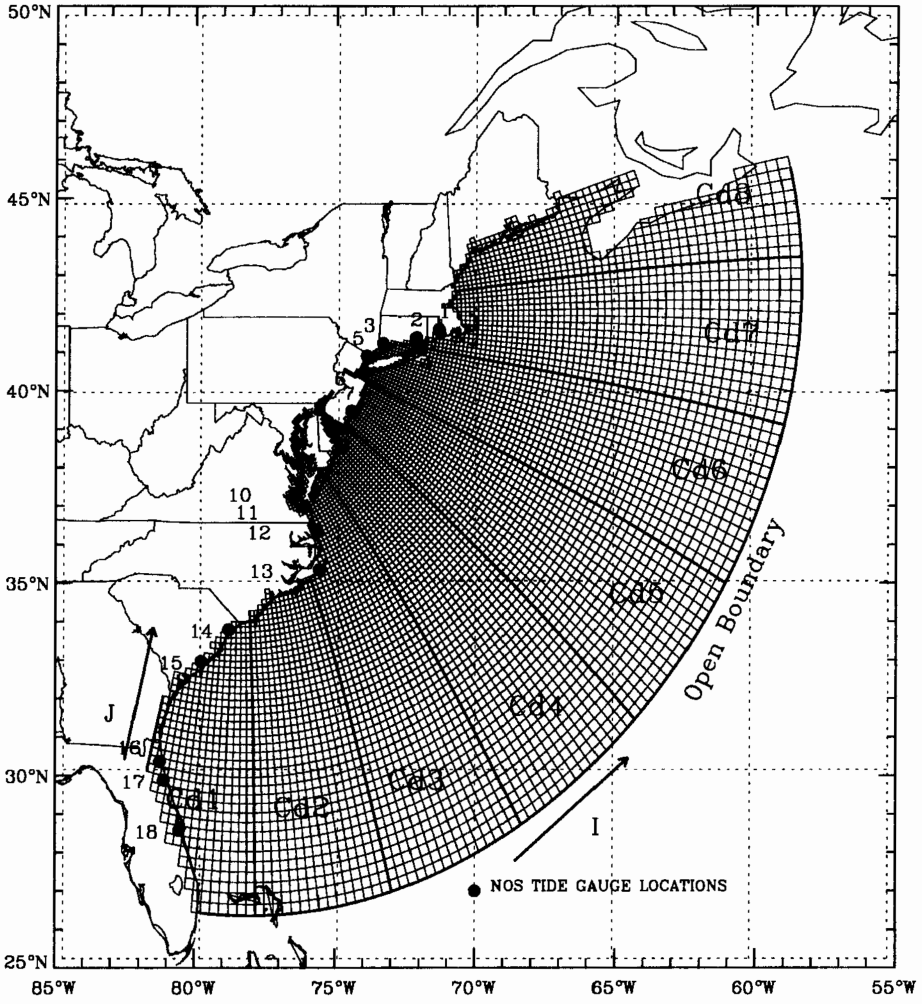

Figure 2.1. Model grid, and eight subregions for surface wind drag coefficients distribution. I and J are the grid indices in the X and Y directions, respectively.

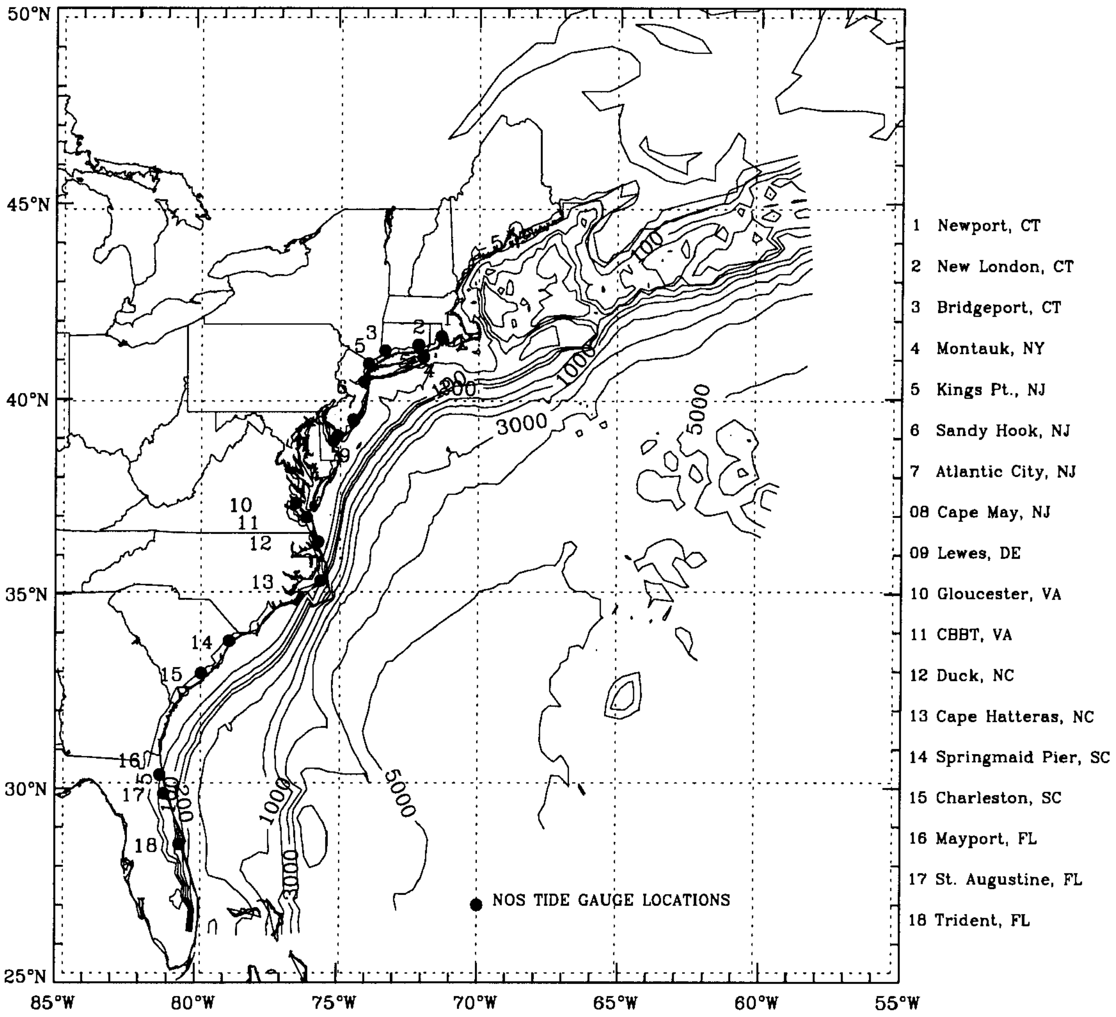

Figure 2.2. Bathymetry in the model domain (in meters) and selected tide gauge locations from the National Water Level Observation Network (NWLON). The station names are listed at right side.

3. ADJOINT MODEL

3.1. Control Variables

For the tidal simulation in the ECDA model, first of all, elevations along the open boundary are considered to be control variables and are estimated by assimilating tidal predictions along the coast, and the optimal open boundary conditions are used in total water level simulations. And then surface wind drag coefficients are considered to be control variables in subtidal and total water level nowcast/forecast simulations.

In tidal simulation model, the elevation values of each tidal constituent along the open boundary can be calculated using Eq.2.8 if the tidal harmonic constants at open boundary grid (A_i and Θ_i) are determined. In order to reduce the number of the control variable, A_i and Θ_i of each tidal constituent are taken as a quadratic polynomials (the shape is based on the results of Schwiderski's tidal model):

$$A_i = a_1 + a_2 \cdot i + a_3 \cdot i^2 \tag{3.1}$$

$$\Theta_i = a_4 + a_5 \cdot i + a_6 \cdot i^2 \tag{3.2}$$

where A_i and Θ_i are the amplitude and the phase of a tidal constituent at open boundary grid, a_1 to a_6 are coefficients of the quadratic polynomials and are used as control variables, i is index of the model grid along the open boundary.

There are 6 control variables for each tidal constituent. Because of the physical nature of these control variables, each has different units and magnitudes. Therefore, these parameters are scaled so that all control variables have the same order of magnitude during the optimization. This avoids ill-conditioning of the Hessian matrix which is mostly used in minimization algorithms such as the quasi-Newton method.

In subtidal simulation model, from sensitivity experiments, we found that the surface wind forcing has a predominant effect on the low-frequency nontidal water level variations along the East Coast. Therefore, It is assumed that errors in the model-produced nontidal water levels will most likely be due to errors in the wind stress field (or to its resolution being too coarse compared with the ocean model grid resolution), and that all other parameters are perfect. For convenience we use changes in the wind drag coefficients to represent (and correct for) any systematic "errors" in the wind field (whatever the cause). Figure 3.1 shows the differences between the observed and EDAS analyzed winds (as interpolated EDAS) at Eastport, CBBT, Duck, and Cape Hatteras. It shows that, in general, the EDAS winds matched the observed winds in speed and direction reasonably well at CBBT, Duck, and Cape Hatteras, yet the match at Eastport was less accurate during this time period. However, most EDAS wind speeds are smaller than the observations, and the EDAS directions deviate from the observations during the strong wind periods. The wind direction deviation has an important impact on the variation of subtidal water levels along the East Coast, which are very sensitive to wind direction. Wind observations from a moored buoy 44014 (at 36.58 °N, 74.83 °W), which is close to CBBT, were also compared with EDAS-interpolated winds. Most of the EDAS wind directions are different from the buoy measured winds, and the observed wind speeds are greater than those of EDAS during the strong wind period. In addition to the errors in surface wind fields, it is possible that there could be errors in the wind drag coefficient, whose behavior as wind speed increases is still not well understood (especially at high wind speeds). A problem with the wind drag coefficient can also occur if the effect of atmospheric stability is not included in its formulation, in which case changing air and water temperature could affect wind stress in an unaccounted manner.

The most widely applied wind stress formulation at the sea surface may be conveniently expressed in terms of the wind speed $\vec{W}_{10}$ at the 10-meter level, the air density, ρ_a, and a non-dimensional drag coefficient, C_d, i. e.,

$$\vec{\tau}_s = \rho_a C_d |\vec{W}_{10}| \vec{W}_{10} \tag{3.3}$$

for the formulation developed by Large and Pond (1981),

$$10^3 C_d = \begin{cases} 1.2 & 0 \le |W_{10}| \le 11 \, m/s \\ 0.49 + 0.065 W_{10} & 11 < |W_{10}| \le 25 \, m/s \end{cases} \tag{3.4}$$

The problem of evaluating the surface wind stress is therefore reduced to estimating the drag coefficient, C_d, at different wind speeds if $\vec{W}_{10}$ and ρ_a are known. Most estimates of C_d have been obtained by indirect observations. The dependence of C_d on wind speed has not been completely resolved, even for lower wind speeds. Thus, by assimilating the observed subtidal water level into the model, it is possible to improve both the wind stress field estimates and the simulated subtidal water levels by adjusting the wind drag coefficient C_d.

Eq.3.4 shows that surface wind drag coefficients vary in both space and time (since wind speed varies with time and space). However, due to the limitation of available water level observations (number and spatial distribution), the wind drag coefficients are assumed to be constant or piecewise constant in the model domain. In this study, the model domain is evenly divided into eight subregions along the J-direction (see the thick line in Figure 2.1), and the value of C_d is assumed to be constant in each subregion within a data assimilation window. The order of magnitude of C_d is about 10^{-3}. For the purpose of convenience and computational accuracy, C_d is scaled by a factor of 10^{-3} (i.e., the scaled $C_d^* = C_d \times 10^3$). Hereafter, the scaled C_d^* is still written as C_d.

3.2. Cost Function

The optimal adjoint method attempts to find a set of undetermined parameters (i.e., control variables) that minimize the cost function in a least-squares sense over a given period of time (the window of data assimilation). Thus, the first task is to define a suitable cost function for a given problem. In a general sense, the cost function measures the distances between the observations and the numerical model results. With the increasing ability to acquire real-time water level observations along the coast, it is feasible to assimilate such real-time data into a numerical model to improve water level nowcasts and forecasts. According to Courtier and Talarand (1990), Zou et al. (1992) and Lardner et al. (1993), it is necessary to add penalty terms in the cost function expression to suppress the high-frequency variations in the state variable simulations and solution of the optimal control variables. The cost function is therefore defined as,

$$J = \frac{1}{2}\sum_{n=2}^{N}\sum_{i=1}^{M} W_i\left(h_i^n - h_{o_i}^n\right)^2 + \frac{1}{2}\gamma_1\sum_{k=1}^{Nc}(C_{d_k} - C_{d_k}^{p})^2 + \frac{1}{2}\gamma_2\sum_{k=1}^{Nc-1}(C_{d_{k+1}} - C_{d_k})^2 \tag{3.5}$$

where $h_{o_i}^n$ *and* h_i^n are observed and simulated water levels at *n*th time step and *i*th tide station; W_i is the corresponding weighting factor (taken as 1.0 here) and *M* is number of observing stations. The second and third terms are the penalty terms that measure the variance of the optimal C_d with time and space, respectively. C_d and C_d^p are the new and previous C_d values, N_c is the total control variable number of C_d, and γ_1 and γ_2 are weighting coefficients which represent the relative influence of these penalty terms and are empirically determined. Sensitivity experiments on γ_1 and γ_2 showed that the better results were obtained from γ_1 and γ_2 being 0.001.

3.3. Discrete Adjoint Equations

The optimal variational problem is to minimize the cost function J (Eqn. 3.5) subject to the governing equations (2.1)-(2.6). The Lagrangian multipliers $\lambda_h, \lambda_u, \lambda_v, \lambda_{\bar{h}}, \lambda_{\bar{u}}, \lambda_{\bar{v}}$ (also called adjoint variables) for the constraint equations (Lawson et al., 1995) are introduced to form an augmented Lagrange function. And then applying the variational operator to the augmented Lagrange function, the first order variational of the cost function is written as,

$$\begin{aligned}
\delta J = &\sum_{n=2}^{N}\sum_{i=2}^{IM-1}\sum_{j=3}^{JM-1}\left(h_{i,j}^n - h_{o_{i,j}}^n\right)\delta h_{i,j}^n + \gamma_1\sum_{k=1}^{N_c}\left(C_{d_k} - C_{d_k}^{p}\right)\delta C_{dk} \\
&+\gamma_2\sum_{k=2}^{N_c-1}\left(2C_{d_k} - C_{d_{k+1}} - C_{d_{k-1}}\right)\delta C_{dk} - \gamma_2\left(C_{d_2} - C_{d_1}\right)\delta C_{d_1} + \gamma_2\left(C_{d_{N_c}} - C_{d_{N_c-1}}\right)\delta C_{d_{N_c}} \\
&+\sum_{n=2}^{N}\sum_{i=2}^{IM-1}\sum_{j=3}^{JM-1}\lambda_{hi,j}^{n}\delta\left\{h_{i,j}^n - \bar{h}_{i,j}^{n-1} + O_{i,j}\left(\ A_{i+1,j}U_{i+1,j}^{n-1} - A_{i,j}U_{i,j}^{n-1} + B_{i,j+1}V_{i,j+1}^{n-1} - B_{i,j}V_{i,j}^{n-1}\ \right)\right\} \\
&+\sum_{n=2}^{N}\sum_{i=2}^{IM-1}\sum_{j=2}^{JM-1}\lambda_{ui,j}^{n}\delta\Big\{U_{i,j}^n - \bar{U}_{i,j}^{n-1} + L_{i,j}F_{xi,j} - \frac{P_{i,j}}{4}\left[f_{i,j}H_{i,j}\left(V_{i,j}^{n-1} + V_{i,j+1}^{n-1}\right) + f_{i-1,j}H_{i-1,j}\left(V_{i-1,j+1}^{n-1} + V_{i-1,j}^{n-1}\right)\right] \\
&+Q_{i,j}\left[(1-2\alpha)\left(h_{i,j}^{n-1} - h_{i-1,j}^{n-1}\right) + \alpha\left(h_{i,j}^n - h_{i-1,j}^n + \bar{h}_{i,j}^{n-1} - \bar{h}_{i-1,j}^{n-1} - Pa_{i,j}^n + Pa_{i-1,j}^n\right)\right] \\
&+P_{i,j}(-10^{-6}Cd_{i,j}\left|W_{si,j}^n\right|W_{ui,j}^n + C_{bi,j}\sqrt{\bar{U}_{i,j}^{n-1^2} + \bar{V}_{i,j}^{n-1^2}}\bar{U}_{i,j}^{n-1})\ \Big\} \\
&+\sum_{n=2}^{N}\sum_{i=2}^{IM-1}\sum_{j=3}^{JM-1}\lambda_{vi,j}^{n}\delta\Big\{V_{i,j}^n - \bar{V}_{i,j}^{n-1} + M_{i,j}F_{y_{i,j}} + \frac{R_{i,j}}{4}\left[f_{i,j}H_{i,j}\left(U_{i,j}^{n-1} + U_{i+1,j}^{n-1}\right) + f_{i,j-1}H_{i,j-1}\left(U_{i+1,j-1}^{n-1} + U_{i,j-1}^{n-1}\right)\right] \\
&+S_{i,j}\left[(1-2\alpha)\left(h_{i,j}^{n-1} - h_{i,j-1}^{n-1}\right) + \alpha\left(h_{i,j}^n - h_{i,j-1}^n + \bar{h}_{i,j}^{n-1} - \bar{h}_{i,j-1}^{n-1} - Pa_{i,j}^n + Pa_{i,j-1}^n\right)\right] \\
&+R_{i,j}(-10^{-6}Cd_{i,j}\left|W_{si,j}^n\right|W_{vi,j}^n + C_{bi,j}\sqrt{\bar{U}_{i,j}^{n-1^2} + \bar{V}_{i,j}^{n-1^2}}\bar{V}_{i,j}^{n-1})\ \Big\} \\
&+\sum_{n=2}^{N}\sum_{i=2}^{IM-1}\sum_{j=1}^{JM-1}\lambda_{\bar{h}i,j}^{n}\delta\left\{\bar{h}_{i,j}^n - h_{i,j}^{n-1} - 0.5\cdot\beta\cdot\left(h_{i,j}^n + \bar{h}_{i,j}^{n-1} - 2h_{i,j}^{n-1}\right)\right\} \\
&+\sum_{n=2}^{N}\sum_{i=2}^{IM-1}\sum_{j=1}^{JM-1}\lambda_{\bar{u}i,j}^{n}\delta\left\{\bar{U}_{i,j}^n - U_{i,j}^{n-1} - 0.5\cdot\beta\cdot\left(U_{i,j}^n + \bar{U}_{i,j}^{n-1} - 2U_{i,j}^{n-1}\right)\right\} \\
&+\sum_{n=2}^{N}\sum_{i=2}^{IM-1}\sum_{j=1}^{JM-1}\lambda_{\bar{v}i,j}^{n}\delta\left\{\bar{V}_{i,j}^n - V_{i,j}^{n-1} - 0.5\cdot\beta\cdot\left(V_{i,j}^n + \bar{V}_{i,j}^{n-1} - 2V_{i,j}^{n-1}\right)\right\}
\end{aligned} \tag{3.6}$$

$$
\begin{aligned}
&+\sum_{n=2}^{N}\sum_{i=2}^{IM-1}\lambda_{h_{i,2}}^{n}\delta\left(h_{i,2}^{n}-h_{i,1}^{n}\right)+\sum_{n=2}^{N}\sum_{i=2}^{IM-1}\lambda_{v_{i,2}}^{n}\delta\left(V_{i,2}^{n}+0.1\sqrt{\frac{g}{H_{i,2}}}\left(h_{i,2}^{n-1}-h_{i,2}^{n}\right)\right)\\
&+\sum_{n=2}^{N}\sum_{i=2}^{IM-1}\lambda_{v_{i,1}}^{n}\delta\left(V_{i,1}^{n}-V_{i,2}^{n}\right)\\
&+\sum_{n=2}^{N}\sum_{i=2}^{IM-1}\lambda_{u_{i,1}}^{n}\delta\left(U_{i,1}^{n}-U_{i,1}^{n-1}+\frac{\Delta t(V_{i,2}^{n-1}-V_{i-1,2}^{n-1})}{\Delta y_{i,1}+\Delta y_{i,2}}(U_{i,2}^{n-1}-U_{i,1}^{n-1})\right)
\end{aligned}
$$

As previously mentioned, elevations along the open lateral boundary and surface wind drag coefficients are the only control variables in the ECDA model. The initial and solid lateral boundary conditions are well posed, and therefore,

$$
\begin{aligned}
&\delta h_{i,j}^{1}=\delta u_{i,j}^{1}=\delta v_{i,j}^{1}=\delta\bar{h}_{i,j}^{1}=\delta\bar{u}_{i,j}^{1}=\delta\bar{v}_{i,j}^{1}=0\\
&\delta h_{1,j}^{n}=\delta u_{1,j}^{n}=\delta v_{1,j}^{n}=\delta\bar{h}_{1,j}^{n}=\delta\bar{u}_{1,j}^{n}=\delta\bar{v}_{1,j}^{n}=0\\
&\delta h_{IM,j}^{n}=\delta u_{IM,j}^{n}=\delta v_{IM,j}^{n}=\delta\bar{h}_{IM,j}^{n}=\delta\bar{u}_{IM,j}^{n}=\delta\bar{v}_{IM,j}^{n}=0\\
&\delta h_{i,JM}^{n}=\delta u_{i,JM}^{n}=\delta v_{i,JM}^{n}=\delta\bar{h}_{i,JM}^{n}=\delta\bar{u}_{i,JM}^{n}=\delta\bar{v}_{i,JM}^{n}=0
\end{aligned}
\tag{3.7}
$$

after applying the chain rule and integrating by parts each term on the right hand side of Eq.3.6, transforming the summation indices in the terms of δJ that involve the Lagrange multipliers, Eq.3.6 can be rewritten as,

$$
\begin{aligned}
\delta J={}&\sum_{n=2}^{N}\sum_{i=2}^{IM-1}\sum_{j=3}^{JM-1}\left(h_{i,j}^{n}-h_{o_{i,j}}^{n}\right)\delta h_{i,j}^{n}+\gamma_1\sum_{k=1}^{N_c}\left(C_{d_k}-C_{d_k}^{p}\right)\delta C_{dk}\\
&+\gamma_2\sum_{k=2}^{N_c-1}\left(2C_{d_k}-C_{d_{k+1}}-C_{d_{k-1}}\right)\delta C_{dk}-\gamma_2\left(C_{d_2}-C_{d_1}\right)\delta C_{d_1}+\gamma_2\left(C_{d_{N_c}}-C_{d_{N_c-1}}\right)\delta C_{d_{N_c}}\\
&\left.\begin{aligned}
&+\sum_{n=1}^{N-1}\sum_{i=2}^{IM-1}\sum_{j=3}^{JM-1}C_{b_{i,j}}\frac{\lambda_{u_{i,j}}^{n+1}P_{i,j}(2\bar{U}_{i,j}^{n\,2}+\bar{V}_{i,j}^{n2})+\lambda_{v_{i,j}}^{n+1}R_{i,j}\bar{U}_{i,j}^{n}\bar{V}_{i,j}^{n}}{\sqrt{\bar{U}_{i,j}^{n\,2}+\bar{V}_{i,j}^{n2}}}\delta\bar{U}_{i,j}^{n}\\
&+\sum_{n=1}^{N-1}\sum_{i=2}^{IM-1}\sum_{j=3}^{JM-1}C_{b_{i,j}}\frac{\lambda_{u_{i,j}}^{n+1}P_{i,j}\bar{U}_{i,j}^{n}\bar{V}_{i,j}^{n}+\lambda_{v_{i,j}}^{n+1}R_{i,j}(\bar{U}_{i,j}^{n\,2}+2\bar{V}_{i,j}^{n2})}{\sqrt{\bar{U}_{i,j}^{n\,2}+\bar{V}_{i,j}^{n2}}}\delta\bar{V}_{i,j}^{n}\\
&+\sum_{n=1}^{N-1}\sum_{i=2}^{IM-1}C_{b_{i,2}}\frac{\lambda_{u_{i,2}}^{n+1}P_{i,2}(2\bar{U}_{i,2}^{n\,2}+\bar{V}_{i,2}^{n2})}{\sqrt{\bar{U}_{i,2}^{n\,2}+\bar{V}_{i,2}^{n2}}}\delta\bar{U}_{i,2}^{n}+\sum_{n=1}^{N-1}\sum_{i=2}^{IM-1}C_{b_{i,2}}\frac{\lambda_{u_{i,2}}^{n+1}P_{i,2}\bar{U}_{i,2}^{n}\bar{V}_{i,2}^{n}}{\sqrt{\bar{U}_{i,2}^{n\,2}+\bar{V}_{i,2}^{n\,2}}}\delta\bar{V}_{i,2}^{n}
\end{aligned}\right\}\text{related to the bottom friction}\\
&\left.\begin{aligned}
&-\sum_{n=2}^{N}\sum_{i=2}^{IM-1}\lambda_{h_{i,2}}^{n}\delta h_{i,1}^{n}+\sum_{n=2}^{N-1}\sum_{i=2}^{IM-1}\left[\lambda_{h_{i,2}}^{n}+0.1\sqrt{\frac{g}{H_{i,2}}}\left(\lambda_{v_{i,2}}^{n+1}-\lambda_{v_{i,2}}^{n}\right)\right]\delta h_{i,2}^{n}\\
&+\sum_{n=2}^{N}\sum_{i=2}^{IM-1}\lambda_{v_{i,1}}^{n}\delta V_{i,1}^{n}+\sum_{n=2}^{N-1}\sum_{i=2}^{IM-1}\lambda_{u_{i,1}}^{n+1}\frac{\Delta t(V_{i,2}^{n}-V_{i-1,2}^{n})}{\Delta y_{i,1}+\Delta y_{i,2}}\delta U_{i,2}^{n}\\
&+\sum_{n=2}^{N-1}\sum_{i=2}^{IM-1}\left\{\lambda_{u_{i,1}}^{n}-\lambda_{u_{i,1}}^{n+1}-\lambda_{u_{i,1}}^{n+1}\frac{\Delta t(V_{i,2}^{n}-V_{i-1,2}^{n})}{\Delta y_{i,1}+\Delta y_{i,2}}\right\}\delta U_{i,1}^{n}\\
&+\sum_{n=2}^{N}\sum_{i=2}^{IM-1}\left\{\lambda_{v_{i,2}}^{n}-\lambda_{v_{i,1}}^{n}+\lambda_{u_{i,1}}^{n+1}\frac{\Delta t(U_{i,2}^{n}-U_{i,1}^{n})}{\Delta y_{i,1}+\Delta y_{i,2}}\right\}\delta V_{i,2}^{n}-\sum_{n=2}^{N-1}\sum_{i=1}^{IM}\lambda_{u_{i+1,1}}^{n+1}\frac{\Delta t(U_{i+1,2}^{n}-U_{i+1,1}^{n})}{\Delta y_{i+1,1}+\Delta y_{i+1,2}}\delta V_{i,2}^{n}
\end{aligned}\right\}\text{related to the open boundary}\\
&+\boldsymbol{\Phi}_{linear\ terms}+\boldsymbol{\Psi}_{nonlinear\ terms}
\end{aligned}
\tag{3.8}
$$

where $\boldsymbol{\Phi}_{linear\ terms}$ includes all terms related to the linear terms in Eq.3.6, which are summarized in Appendix A, and $\boldsymbol{\Psi}_{nonlinear\ terms}$ includes all terms related to the nonlinear horizontal advection and diffusion terms in Eq.3.6,

$$\boldsymbol{\Psi}_{nonlinear\ terms}=\sum_{n=2}^{N}\sum_{i=2}^{IM-1}\sum_{j=2}^{JM-1}L_{i,j}\lambda_{u_{i,j}}^{n}\delta F_{x_{i,j}}+\sum_{n=2}^{N}\sum_{i=2}^{IM-1}\sum_{j=3}^{JM-1}M_{i,j}\lambda_{v_{i,j}}^{n}\delta F_{y_{i,j}} \tag{3.9}$$

which are summarized in Appendix B. Substituting all of the terms of $\boldsymbol{\Phi}_{linear\ terms}$ and $\boldsymbol{\Psi}_{nonlinear\ terms}$ into Eq.3.8. By organizing the coefficients of each non-control variable($\delta h, \delta U, \delta V, \delta\overline{h}, \delta\overline{V}, \delta\overline{h}$) together and forcing the coefficients of non-control variables to be zero, the corresponding adjoint discrete equations are derived as,

$$\lambda_{\overline{h}i,j}^{n}-\lambda_{hi,j}^{n+1}+\alpha Q_{i,j}\lambda_{ui,j}^{n+1}-\alpha Q_{i+1,j}\lambda_{ui+1,j}^{n+1}+\alpha S_{i,j}\lambda_{vi,j}^{n+1}-\alpha S_{i.j+1}\lambda_{vi,j+1}^{n+1}-0.5\cdot\beta\lambda_{\overline{h}i,j}^{n+1}=0 \tag{3.10}$$

$$\lambda_{\overline{u}i,j}^{n}-\lambda_{ui,j}^{n+1}-0.5\beta\lambda_{\overline{u}i,j}^{n+1}+C_{bi,j}\frac{\lambda_{ui,j}^{n+1}P_{i,j}(2\overline{U}_{i,j}^{n\,2}+\overline{V}_{i,j}^{n\,2})+\lambda_{vi,j}^{n+1}R_{i,j}\overline{U}_{i,j}^{n}\overline{V}_{i,j}^{n}}{\sqrt{\overline{U}_{i,j}^{n\,2}+\overline{V}_{i,j}^{n\,2}}}+F_{\overline{u}}=0 \tag{3.11}$$

$$\lambda_{\overline{v}i,j}^{n}-\lambda_{vi,j}^{n+1}-0.5\beta\lambda_{\overline{v}i,j}^{n+1}+C_{bi,j}\frac{\lambda_{ui,j}^{n+1}P_{i,j}\overline{U}_{i,j}^{n}\overline{V}_{i,j}^{n}+\lambda_{vi,j}^{n+1}R_{i,j}(\overline{U}_{i,j}^{n\,2}+2\overline{V}_{i,j}^{n\,2})}{\sqrt{\overline{U}_{i,j}^{n\,2}+\overline{V}_{i,j}^{n\,2}}}+F_{\overline{v}}=0 \tag{3.12}$$

$$\begin{aligned}&\lambda_{hi,j}^{n}+Q_{i,j}(1-2\alpha)\lambda_{ui,j}^{n+1}-Q_{i+1,j}(1-2\alpha)\lambda_{ui+1,j}^{n+1}+Q_{i,j}\alpha\lambda_{ui,j}^{n}-Q_{i+1,j}\alpha\lambda_{ui+1,j}^{n}\\&+S_{i,j}(1-2\alpha)\lambda_{vi,j}^{n+1}-S_{i,j+1}(1-2\alpha)\lambda_{vi,j+1}^{n+1}+S_{i,j}\alpha\lambda_{vi,j}^{n}-S_{i,j+1}\alpha\lambda_{vi,j+1}^{n}\\&-\lambda_{\overline{h}i,j}^{n+1}-0.5\beta\lambda_{\overline{h}i,j}^{n}+\beta\lambda_{\overline{h}i,j}^{n+1}+W_{i,j}^{n}(h_{i,j}^{n}-ho_{i,j}^{n})=0\end{aligned} \tag{3.13}$$

$$\begin{aligned}&\lambda_{ui,j}^{n}+O_{i-1,j}A_{i,j}\lambda_{hi-1,j}^{n+1}-O_{i,j}A_{i,j}\lambda_{hi,j}^{n+1}+\frac{R_{i,j}}{4}f_{i,j}H_{i,j}\lambda_{vi,j}^{n+1}+\frac{R_{i-1,j}}{4}f_{i-1,j}H_{i-1,j}\lambda_{vi-1,j}^{n+1}\\&+\frac{R_{i,j+1}}{4}f_{i,j}H_{i,j}\lambda_{vi,j+1}^{n+1}+\frac{R_{i-1,j+1}}{4}f_{i-1,j}H_{i-1,j}\lambda_{vi-1,j+1}^{n+1}-(1-\beta)\lambda_{\overline{u}i,j}^{n+1}-0.5\beta\lambda_{\overline{u}i,j}^{n}+F_{u}=0\end{aligned} \tag{3.14}$$

$$\begin{aligned}&\lambda_{vi,j}^{n}+O_{i,j-1}B_{i,j}\lambda_{hi,j-1}^{n+1}-O_{i,j}B_{i,j}\lambda_{hi,j}^{n+1}-\frac{P_{i,j}}{4}f_{i,j}H_{i,j}\lambda_{ui,j}^{n+1}-\frac{P_{i,j-1}}{4}f_{i,j-1}H_{i,j-1}\lambda_{ui,j-1}^{n+1}\\&-\frac{P_{i+1,j-1}}{4}f_{i,j-1}H_{i,j-1}\lambda_{ui+1,j-1}^{n+1}-\frac{P_{i+1,j}}{4}f_{i,j}H_{i,j}\lambda_{ui+1,j}^{n+1}-(1-\beta)\lambda_{\overline{v}i,j}^{n+1}-0.5\beta\lambda_{\overline{v}i,j}^{n}+F_{v}=0\end{aligned} \tag{3.15}$$

where the coefficients of $F_{\overline{u}}, F_{\overline{v}}, F_{u}, F_{v}$ are listed in Appendix C.

Therefore, the increment of the cost function now becomes,

$$\delta J = -\sum_{n=2}^{N}\sum_{i=2}^{IM-1} \lambda_{h_{i,2}}^{n}\delta h_{i,1}^{n} - \sum_{n=2}^{N}\sum_{i=2}^{IM-1}\sum_{j=2}^{JM-1} 10^{-6}\left|W_{s_{i,j}}^{n}\right|\left(P_{i,j}W_{u_{i,j}}^{n}\lambda_{u_{i,j}}^{n} + R_{i,j}W_{v_{i,j}}^{n}\lambda_{v_{i,j}}^{n}\right)\delta C_{d_{i,j}}$$
$$+ \gamma_1\sum_{k=1}^{N_c}\left(C_{d_k} - C_{d_k}^{P}\right)\delta C_{dk} + \gamma_2\sum_{k=2}^{N_c-1}\left(2C_{d_k} - C_{d_{k+1}} - C_{d_{k-1}}\right)\delta C_{dk} - \gamma_2\left(C_{d_2} - C_{d_1}\right)\delta C_{d_1} + \gamma_2\left(C_{d_{N_c}} - C_{d_{N_c-1}}\right)\delta C_{d_{N_c}} \qquad (3.16)$$

The adjoint variables $\lambda_{\bar{u}_{i,j}}^{n}, \lambda_{\bar{v}_{i,j}}^{n}, and\ \lambda_{\bar{h}_{i,j}}^{n}$ are calculated by solving the Eq.3.10-3.12. Then Eq.3.13-3.15 are used to solve for the adjoint variables $\lambda_{u_{i,j}}^{n}, \lambda_{v_{i,j}}^{n}, and\ \lambda_{h_{i,j}}^{n}$. The sequence of computing adjoint variables in the adjoint model is the reverse of the sequence of computing state variables in the forward model. After obtaining the adjoint variables, the gradient of the cost function with respect to the control variables can be calculated. In the tidal simulation model (determination of tidal open boundary), for each tidal constituent, substitute Eq.2.8, Eq.3.1 and 3.2 into Eq.3.16, and then the gradients of the cost function with respect to the open boundary control variables are obtained

$$\begin{aligned}
\frac{\partial J}{\partial a_1} &= -\sum_{n=1}^{N-1}\sum_{i=2}^{IM-1}\chi_i\lambda_{i,2}^{n}\cdot\cos\left(\omega t^n + E_i - \Theta_i\right)\\
\frac{\partial J}{\partial a_2} &= -\sum_{n=1}^{N-1}\sum_{i=2}^{IM-1}\chi_i\lambda_{i,2}^{n}\cdot i\cdot\cos\left(\omega t^n + E_i - \Theta_i\right)\\
\frac{\partial J}{\partial a_3} &= -\sum_{n=1}^{N-1}\sum_{i=2}^{IM-1}\chi_i\lambda_{i,2}^{n}\cdot i^2\cdot\cos\left(\omega t^n + E_i - \Theta_i\right)\\
\frac{\partial J}{\partial a_4} &= -\sum_{n=1}^{N-1}\sum_{i=2}^{IM-1}\chi_i\lambda_{i,2}^{n}\cdot A_i\cdot\sin\left(\omega t^n + E_i - \Theta_i\right)\\
\frac{\partial J}{\partial a_5} &= -\sum_{n=1}^{N-1}\sum_{i=2}^{IM-1}\chi_i\lambda_{i,2}^{n}\cdot A_i\cdot i\cdot\sin\left(\omega t^n + E_i - \Theta_i\right)\\
\frac{\partial J}{\partial a_6} &= -\sum_{n=1}^{N-1}\sum_{i=2}^{IM-1}\chi_i\lambda_{i,2}^{n}\cdot A_i\cdot i^2\cdot\sin\left(\omega t^n + E_i - \Theta_i\right)
\end{aligned} \qquad (3.17)$$

Eq.3.17 can be applied to any tidal constituent (here we consider only M_2, S_2, K_1, O_1, N_2). The total number of the control variables is determined by how many tidal constituents are used as the open boundary forcing.

In the case that surface wind drag coefficients are the only control variables, if C_d is assumed to be constant in the entire domain within a data assimilation window (only one control variable in this case), the gradient of the cost function with respect to C_d is

$$\frac{\delta J}{\delta C_d} = -10^{-6}\sum_{n=2}^{N}\sum_{i=2}^{IM-1}\sum_{j=2}^{JM-1}\left|W_{s_{i,j}}^{n}\right|\left(P_{i,j}W_{u_{i,j}}^{n}\lambda_{u_{i,j}}^{n} + R_{i,j}W_{v_{i,j}}^{n}\lambda_{v_{i,j}}^{n}\right) + \gamma_1\left(C_d - C_d^{P}\right) \qquad (3.18)$$

For C_d being piecewise constant case, C_d is assumed to be constant in each subregion (as shown in Figure 2.1) within a data assimilation window and is considered as a control variable. The gradient of the cost function with respect to wind drag coefficients is,

$$\begin{aligned}
\frac{\delta J}{\delta C_{d1}} &= -10^{-6}\sum_{n=2}^{N}\sum_{i=I_0}^{I_1}\sum_{j=2}^{JM-1}\left|W_{si,j}^{n}\right|\left(P_{i,j}W_{ui,j}^{n}\lambda_{ui,j}^{n} + R_{i,j}W_{vi,j}^{n}\lambda_{vi,j}^{n}\right) + \gamma_1\left(C_{d1} - C_{d1}^{p}\right) \quad - \gamma_2\left(C_{d2} - C_{d1}\right) \\
\frac{\delta J}{\delta C_{dk}} &= -10^{-6}\sum_{n=2}^{N}\sum_{i=I_{k-1}}^{I_k}\sum_{j=2}^{JM-1}\left|W_{si,j}^{n}\right|\left(P_{i,j}W_{ui,j}^{n}\lambda_{ui,j}^{n} + R_{i,j}W_{vi,j}^{n}\lambda_{vi,j}^{n}\right) + \gamma_1\left(C_{dk} - C_{dk}^{p}\right)\delta C_{dk} + \gamma_2\left(2C_{dk} - C_{dk+1} - C_{dk-1}\right) \qquad (3.19) \\
\frac{\delta J}{\delta C_{dN_c}} &= -10^{-6}\sum_{n=2}^{N}\sum_{i=I_{N_c-1}}^{I_{N_c}}\sum_{j=2}^{JM-1}\left|W_{si,j}^{n}\right|\left(P_{i,j}W_{ui,j}^{n}\lambda_{ui,j}^{n} + R_{i,j}W_{vi,j}^{n}\lambda_{vi,j}^{n}\right) + \gamma_1\left(C_{dN_c} - C_{dN_c}^{p}\right) + \gamma_2\left(C_{dN_c} - C_{dN_c-1}\right) \\
I_0 &= 1,\ I_k = k*\frac{IM}{8},\quad k = 1,2,\cdots,8
\end{aligned}$$

The Eq.3.17-3.19 show that no matter how many control variables there are, the gradient of the cost function can be efficiently derived after integrating the adjoint model once. Thus, the adjoint model provides an efficient method for calculating gradient of the cost function in optimization process, especially for the case of large number of control variables.

3.4. Optimization and Iteration Scheme

By forward integrating the forward model and then integrating the adjoint model backward, the cost function and its gradient are available. An unconstrained optimization algorithm is needed to minimize the cost function, and determine the optimal control variables. For most unconstrained optimization algorithms, the gradients of the cost function are required in the iterative process to find the optimal direction and to compute the step-size in that direction. The control variables are then adjusted in order to minimize the cost function. For a linear model, the number of iterations required to reach the minimum of the cost function is theoretically equal to the number of control variables. However, the umber of iterations is affected by many factors, such as the number of observations, distribution of observations, and the data assimilation window length. Therefore, it is crucial to select a robust and efficient optimization algorithm that can provide a fast convergence toward the minimum of the cost function.

Several useful algorithms have been developed based on the descent direction method. There are conjugate-gradient methods, Newton and truncated Newton methods, quasi-Newton methods, and limited memory quasi-Newton methods. Based on the studies of Gilbert and Lemarechal (1989) and Zou et al. (1992), the limited memory quasi-Newton method is a robust and efficient method requiring the fewest iterations and storage memory. Thus, in this study, we choose to use the limited memory Broyden-Fletcher-Goldfarb-Shanno (BFGS) quasi-Newton algorithm to perform the numerical optimization. The description of this method was given by Liu and Nocedal (1989) and Nash and Nocedal (1989).

The procedure of the iterative optimal data assimilation that is applied to all the following experiments is described as:

i) Forward integrate the forward numerical model for a data assimilation window (T=30 days for the tidal open boundary conditions and T=24 hours for the wind drag coefficients) with the initial values of the control variables. Save hourly simulated elevations at the corresponding tide stations.

ii) Calculate data misfits between the model results (h) and the observations (h_o) at locations where data exist and save them into a temporary file. Calculate the value of the cost function with Eq.3.5.

iii) Integrate the adjoint model backward in time from $t=T$ to $t=0$, forced by data misfits to calculate the adjoint variables $\lambda_h, \lambda_u, \lambda_v, \lambda_{\bar{h}}, \lambda_{\bar{u}}, \lambda_{\bar{v}}$. And then calculate the gradient of the cost function with respect to the control variables.

iv) Use the limited memory BGFS quasi-Newton minimization algorithm to calculate optimal control variable estimates.

v) Check whether the convergence criterion, $\|G\| < \varepsilon \; or \; J < \varepsilon$ (G is norm of the gradient, J is value of the cost function, and ε is criterion), for the minimization process is satisfied. If Yes, iteration is stopped, and go to step vi. Otherwise, step i to v are repeated with the new values of the control variables.

vi) Integrate the forward numerical model with final optimal values of the control variables.

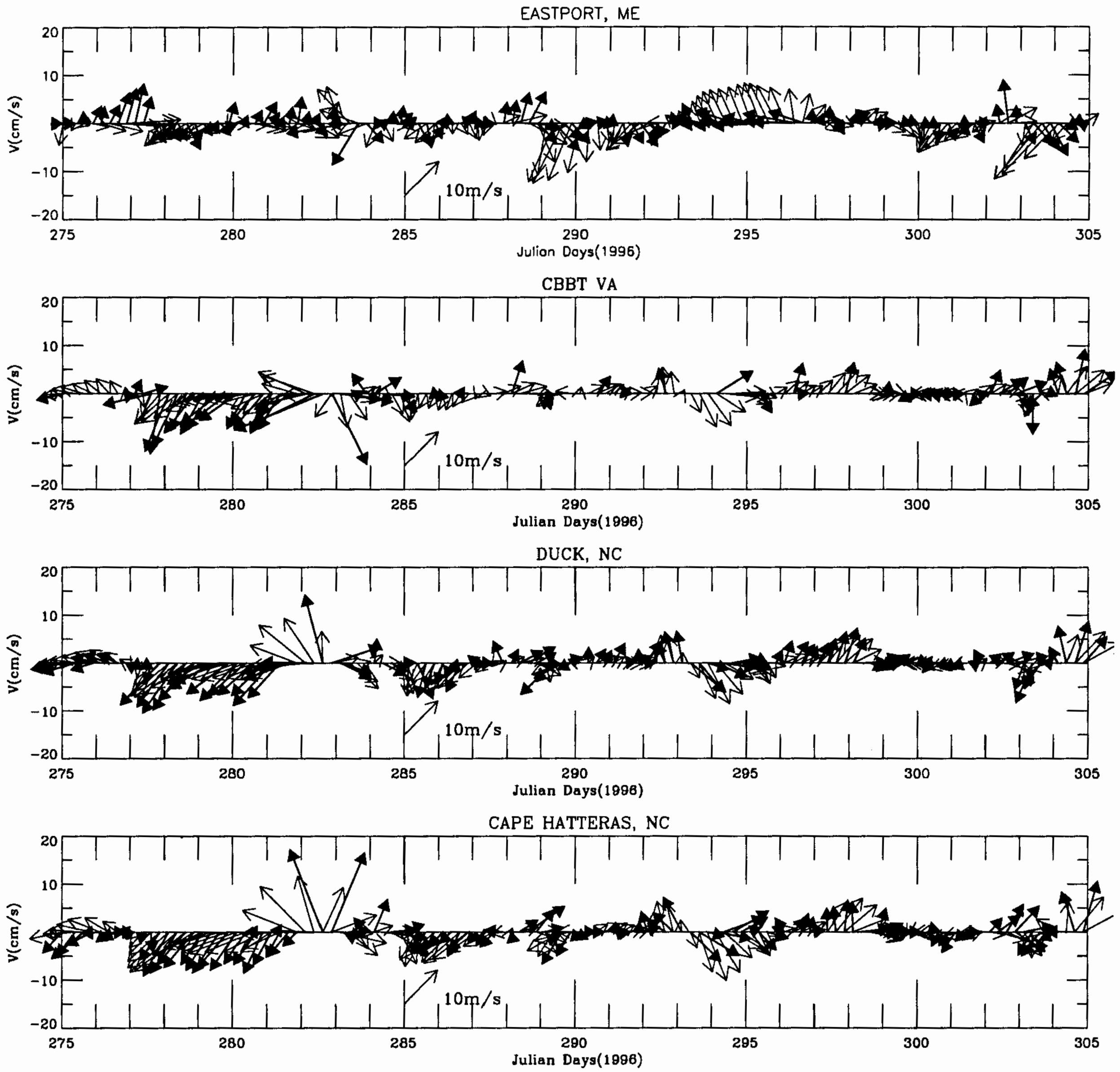

Figure 3.1. Comparison of observed and EDAS surface winds at Eastport, CBBT, Duck and Cape Hatteras in October, 1996. Solid arrows, observed winds; open arrows, EDAS analyzed winds.

4. VERIFICATION OF THE ADJOINT MODEL

It is important to ensure correctness of the adjoint code and efficiently converging rate of the optimization process. Any error in the adjoint model equations can result in wrong gradient of the cost function with respect to the control variables. Therefore, the optimization method can fail to find a reasonable optimal parameter estimation. Various tools can be used to debug and verify the adjoint model equations. The most useful method is to use gradient of the cost function to check the correctness of the adjoint model equations. This involves perturbing each of the control variables by an appropriate small amount and integrating the forward model to calculate the change in the cost function with respect to the corresponding control variable. The derivative of the cost function at any point of C_d of the parameter space can be calculated by a finite difference (FD) method as follows,

$$G = \frac{J(C_d + \Delta C_d) - J(C_d)}{\Delta C_d} \tag{4.1}$$

The gradient calculated from an adjoint model should be consistent with that calculated using Eq.4.1 within the order of ΔC_d.

To verify the performance of the adjoint data assimilation procedure, an identical twin experiment is used in which pseudo-observations are generated by the numerical model with predetermined control variables. Therefore, the "data" are not contaminated with observational errors and contain the same dynamics as the numerical model itself used in the data assimilation procedure. In this section, the correctness of the adjoint model equations is verified with Eq.4.1, and the performance of the data assimilation system is evaluated by identical twin experiments. The penalty terms in Eq.3.5 are not considered in the following identical twin experiments of this section.

4.1. Test of Gradient of the Cost Function

Several experiments have been performed to compare the gradient of the cost function calculated using Eq.4.1 with that calculated from the adjoint model. Similar results were found in these experiments. As an example, results from the experiments of estimating wind drag coefficients are presented. The hourly low-pass filtered subtidal water level observations at 18 NOS tide gauge stations are used to calculate the values of the cost function and data misfits. These data misfits, which measure the distance between the observations and model results, are used to force the adjoint model.

Two experiments were performed, the first using one control variable and the second using eight control variables. In the former, the gradients for different values of C_d are presented in Table 4.1. It shows that the gradients calculated using the finite difference method and the adjoint method are very close in magnitude and are consistent in signs. The maximum gradient difference between the two methods is less than 0.0012. This difference is insignificant and reasonable, being approximately 5% of the gradients calculated. In order to verify the correctness of adjoint model equations for the multiple control variables case, the gradients of the cost function for eight control variables are similarly calculated using both the finite difference method (with ΔC_d=0.2) and the adjoint method.

In this case, C_d is defined as a sinusoidal function of time, and there is a one day phase shift between each of the 8 control variables.

$$C_d(m) = 10.0 + 5.0\sin\left[\ \frac{2\pi}{30.0}\left(J_D + m - 1\right)\ \right], \qquad m = 1,\cdots,8 \tag{4.2}$$

where m represents the index of the control variable and J_D is the Julian day (the control variables remain constant within the 24-hour data assimilation window). The time series of the hypothetical wind drag coefficients (Eq.4.2) are plotted in Figure 4.1. Note that these hypothetical C_d values are also used in the identical twin experiments in the next section. The gradients of the cost function for consecutive 30-day period are presented in Figure 4.2. It can be seen that the gradients using both the finite difference method and the adjoint method are in very good agreement. The maximum and minimum gradient differences between the two methods during the 30-day period are presented in Table 4.2. The maximum difference is 1.33×10^{-3}, for the second gradient component, and the maximum difference of the norm of gradients is 1.44×10^{-3}.

Table 4.1 Comparison of the gradients (G) from finite difference method and adjoint method with one control variable

C_d	ΔC_d	G of FD	G of Adjoint	Difference
3.6	0.2	0.002012	0.001917	0.000095
	0.02	0.002029		0.000112
	0.002	0.002047		0.000130
5.0	0.2	0.003807	0.003649	0.000158
	0.02	0.003803		0.000154
	0.002	0.003894		0.000244
10.0	0.2	0.010225	0.009827	0.000398
	0.02	0.010207		0.000380
	0.002	0.01013		0.000303
15.0	0.2	0.01664	0.01586	0.00078
	0.02	0.01665		0.00079
	0.002	0.01668		0.00082
20.0	0.2	0.02306	0.02188	0.00118
	0.02	0.02302		0.00114
	0.002	0.02295		0.00107

The above experiments for one and eight control variables show that the gradients calculated using the adjoint model are consistent with those calculated using the finite difference method. This demonstrates that the adjoint model developed in Section 3 can give the same accurate gradients of the cost function as the finite difference method. However, the adjoint method is more efficient than the finite difference method, especially for a large number of control variables.

Table 4.2. The maximum and minimum gradient differences of the gradient components between finite difference method and the adjoint method

Component	$\|G\|$ (norm)	G(1)	G(2)	G(3)	G(4)	G(5)	G(6)	G(7)	G(8)
Max. Diff.	1.44×10^{-3}	1.19×10^{-3}	1.33×10^{-3}	6.23×10^{-4}	2.87×10^{-4}	2.12×10^{-4}	7.79×10^{-4}	1.24×10^{-3}	2.95×10^{-4}
Min. Diff.	$<10^{-8}$	3.0×10^{-6}	2.0×10^{-6}	$<10^{-8}$	1.1×10^{-6}	2.3×10^{-7}	$<10^{-8}$	$<10^{-8}$	$<10^{-8}$

4.2. Identical Twin Experiments

The verification above indicates that the gradient computed by the adjoint model is very close and consistent with that from the finite-difference method. It now remains to determine whether the correct optimal control variables can be obtained by the optimization procedure, and how fast the iterative optimization converges. Identical twin experiment is the most useful tool to verify and evaluate the performance and feasibility of the adjoint data assimilation procedure. In the identical twin experiment, the pseudo-observations are generated by the numerical model itself with a set of predetermined control variables. Thus, the pseudo-observations are not contaminated by any observational errors and contain the same dynamics as the numerical model, and we can sample any kind of the pseudo-observation (current and elevation at any grid point and any time step). Another merit of the identical twin experiment is that the true values of control variables are already known, we therefore can examine whether or not the optimal control variables converge to their true values. Thus, identical twin experiment is the best situation for data assimilation and is widely used to evaluate and verify the performance of a developed adjoint data assimilation system. In this section, twin experiments of recovering the "true" tidal boundary conditions and the "true" wind drag coefficients are performed, respectively.

4.2.1. Recovery of Tidal Boundary Conditions

In this identical twin experiment, tidal elevations of M_2 constituent are specified along the open boundary. The coefficients of amplitude and phase, a_1-a_6 (see Eq. 3.1 and 3.2), are the control variables, so the elevations along the open boundary are calculated after determining the control variables. The tidal model is integrated with the predetermined values of a_1-a_6 (called "true" values) for at least 60 days (results from the first 30 days are not used in order to eliminate initial oscillations). The hourly simulated elevations at 18 NOS tide gauge stations (see Table 2.1) are saved and used as pseudo-observations in the data assimilation process.

A twin experiment was conducted in which initial value of each control variable is obtained by subtracting 0.5 from its "true" values. Figure 4.3 shows the values of the cost function (J) and the norm of its gradient (G) versus the number of iterations in the optimization process (all values are normalized by their own initial values, J_0 and G_0). We can see that the cost function and the norm of the gradient drop rapidly in the first several iterations. The convergence criterion is satisfied after 43 iterations. The relative value of the cost function (J/J_0) decreases from 1 to 10^{-7}. The final value of the norm of the gradient is less than 10^{-6}. The optimal amplitudes and phases of M_2 constituent along the open boundary (Figure 4.4) converge closely to their true values from the initial values. *RMS* errors between the true and optimal elevations for 30 days along the open boundary are presented in Figure 4.5. Although the optimal amplitude and phase are not exactly coincident with the true values, the RMS errors are less than 1cm and the correlation coefficients (*Cr*) are greater than 0.999. Another experiment was conducted in which initial values of the control variables were set to be zero in order to test sensitivity of the performance of the optimization procedure to the initial values of the control variables. Similar results were obtained, which shows that the optimization procedure is independent of the choice for the initial values of the control variables. However, the initial guess must be meaningful and ensure the model running reasonably. On the other hand, for the efficiency of the optimization process, the initial guess of the control variables should be as close to the true solution as possible.

Table 4.3. Optimal coefficients of the quadratic polynomials (Eq. 3.1 and 3.2) of amplitude and phase of M_2 constituent for the twin identical experiments

Experiment	a_1	a_2	a_3	a_4	a_5	a_6
True_value	0.4213	-0.2759	0.2769	0.6688	-0.3929	0.9759
Initial_value	0.9213	0.2241	0.7769	1.1688	0.1071	1.4759
ITE_Sta18	0.4187	-0.2695	0.2764	0.6771	-0.4339	1.4349
ITE_Sta9	0.4189	-0.2699	0.2767	0.6768	-0.4386	1.4370
ITE_Sta6	0.4131	-0.2377	0.2446	0.6734	-0.4305	1.4421
ITE_Sta9_2	0.4096	-0.2160	0.2221	0.6703	-0.4240	1.4430
ITE_Sta6_2	0.4076	-0.2313	0.2453	0.6794	-0.4423	1.4272

A series of sensitivity experiments in which the number of water level stations was reduced step by step have been performed. We began with all 18 stations (denoted as ITE_Sta18), in which the pseudo-observations from the 18 stations are assimilated. In the next experiment, the pseudo-observations from 9 stations selected from ITE_Sta18 along the open coast (stations 4,6,7,9,12,13,15,17 and 18) are assimilated (ITE_Sta9). In the ITE_Sta6 experiment, 6 stations were selected from the stations used in experiment ITE_Sta9 (stations 4,6,7,12,13 and 17, respectively). The initial value of each control variable was obtained by adding 0.5 to its true value, and the same initial values of the control variables were set for all experiments. Values of the optimal control variables from these three experiments are listed in Table 4.3, and the optimal harmonic constants (amplitude and phase) along the open boundary calculated from these optimal control variables are presented in Figure 4.6. We can see that the optimal control variables do not exactly equal the true values for the three experiments. The optimal control variables from ITE_Sta9 are very close to those of ITE_Sta18 (the difference for each control variable is less than 0.004). The optimal amplitudes and phases along the open boundary derived by the optimal control variables from ITE_Sta18 and ITE_Sta9 are almost coincident and they are closer to the true values than those from ITE_Sta6. Simulated elevations at all of the tide gauge stations from these three experiments are close to the pseudo-observations, and RMS errors at 18 stations are all less than 0.1cm. This demonstrates that the true open boundary elevations can be recovered by assimilating tidal elevation data at coastal stations.

It is noticed that the parameter a_6 did not converge to its true value from the initial value in each of the experiments. The reason is that the "true" phase solution is primarily a linear function of I, and the model simulations are thus not sensitive to a_6. It makes no sense to try to determine a nonsensitive parameter. Therefore, the parameter a_6 can be specified as a constant or discarded in the data assimilation procedure. In order to investigate the effect of the spatial distribution of the assimilated data on the optimization procedure, two other experiments were performed: ITE_Sta9_2 and ITE_Sta6_2. In the ITE_Sta9_2 experiment, data from 9 water level stations inside bays or rivers (different from those used in ITE_Sta9) were used in data assimilation. In the ITE_Sta6_2 experiment, data from 6 stations between Montauk and Lewes (stations 4-9) were assimilated. The optimal amplitude and phase at the open boundary are also plotted in Figure 4.6. The optimal amplitude and phase along the open boundary from the ITE_Sta9_2 deviated more from the true values than even the ITE_Sta6 results. This shows that the data from inside bays or rivers may include some signals which cannot be produced by the open boundary tidal forcing but by the local geometry and bathymetry (local tidal dynamics). The true open ocean boundary conditions cannot therefore be obtained by assimilating such data. In the ITE_Sta6_2 experiment, the northernmost 6 stations from ITE_Sta18 are used. The optimal amplitudes and phases along northeast part of the open boundary are the closest to the true values among all of these twin experiments. However, ITE_Sta6_2 yields the worst results along the southern part of the open boundary. The elevation RMS errors for ITE_Sta9_2 and ITE_Sta6_2 at coastal stations are not significantly different from those of ITE_Sta18, ITE_Sta9, and ITE_Sta6. The elevation RMS errors for ITE_Sta6_2 at 18 tidal stations are less than 0.5cm. The identical twin experiments show that the true open boundary conditions can be recovered by assimilating ideal pseudo-observations from coastal stations. Better results are obtained by assimilating data from open coast stations than stations from inside shallow bays or rivers. The spatial distribution of the stations also has a significant effect on estimates of the optimal open boundary conditions.

4.2.2. Recovery of Wind Drag Coefficients

Three kinds of identical twin experiments for recovering wind drag coefficients were performed: one with one control variable, one with eight control variables, and one with 16 control variables. Since the results from all kinds of experiments are very similar, the results from only the eight control variables experiments are presented here. In this kind of experiment, the following runs were performed:

- **ITE_WDC1:** one-day data assimilation with pseudo-observations
- **ITE_WDC2:** one-day data assimilation with contaminated pseudo-observations
- **ITE_WDC3:** 30-day continuous data assimilation with pseudo-observations
- **ITE_WDC4:** 30-day continuous data assimilation with contaminated pseudo-observations

As explained in Section 3.1, the wind drag coefficient is dependent on wind speed and varies both spatially and temporally. In finding the optimal values for C_d, we are allowing the "improvement" in C_d to represent (and correct for) a systematic error in the wind field, that varies in space and time.

However, it is almost impossible to use the wind drag coefficient of each gird point as a control variable in the data assimilation procedure because of the limitation of available observations and computational cost. In order to assess the performance of the adjoint data assimilation system for the multi control variables case, experiments with eight piecewise constant control variables (the spatial distribution of C_d in the model domain is shown in Figure 2.1) were designed, in which pseudo water levels were generated by integrating the forward model with the hypothetical values of C_d of Eq.4.2, and hourly pseudo water levels from 18 tide gauge stations were used in data assimilation. The results are described as follows.

ITE_WDC1: *one-day data assimilation with pseudo-observations*

In this experiment, the initial values for all C_d are set to 20.0. The optimal C_d values determined at each iteration are presented in Figure 4.7. It shows that most of the optimal C_d values converge toward their true solutions rapidly during the first several iterations, and are very close to their true values after approximately 10 iterations. The maximum difference between the true solution and the final optimal C_d for eight control variables is 1.5×10^{-4} and appeared at the eighth C_d component. Figure 4.8 shows the variation of the cost function (J) and the norm of its gradient ($\|G\|$) versus the number of iterations for this experiment. The cost function and the norm of its gradient have been normalized by their own initial values J_0 and $\|G_0\|$ (the values of the cost function and the norm of the gradient correspond to the initial values of the control variables) for convenience of comparison. It is evident that the cost function and the norm of the gradient drop rapidly in the initial three iterations. The convergence criterion $\|G\| < \varepsilon$ (here $\varepsilon=10^{-7}$ of computer accuracy) is satisfied after 30 iterations. The corresponding values of the cost function and the norm of the gradient are 1.4×10^{-11} and 3.2×10^{-8}, respectively.

The impact of the initial values of the control variables on the results of the optimization procedure was also tested. The results show that no matter how far the initial guesses are from their true solutions, the value of the cost function and the norm of the gradient drop rapidly in the first several iterations, and the optimal C_d values are very close to their true solutions after about ten iterations. After that, the optimization procedure adjusts the optimal C_d slowly, and all of the eight optimal C_d components gradually converge to their true solutions.

ITE_WDC2: *one-day data assimilation with contaminated pseudo-observations*

In the ITE_WDC1 experiment, the pseudo-observations do not contain any observational errors. Therefore, the optimal values of C_d efficiently converge to their true solution. However, water level observations are always contaminated with errors. In order to assess the effects of observational errors on the performance of the data assimilation system, white noise with zero mean and a standard deviation of 0.057 m was superimposed on the pseudo-observations used in the ITE_WDC1. As an example, the contaminated pseudo-observations at Sandy Hook are shown in Figure 4.9. The same data assimilation procedure as ITE_WDC1 was repeated with initial C_d values of 20.0 but the contaminated pseudo-observations were assimilated. Figure 4.10 shows the variation of the optimal C_d with the number of iterations. It can be seen that the trend for each optimal C_d component is very similar to that of ITE_WDC1. However, there is a larger difference between the final optimal value and the true solution for each control variable. The maximum difference among the eight components is now 0.53 (for the second C_d component). The trends of the cost function and the norm of the gradient (shown in Figure 4.11) are also similar to those of ITE_WDC1, although the cost function is much greater than that of ITE_WDC1. After about 10 iterations the misfits between the model results and the pseudo-observations closely resemble the superimposed white noise signal (the misfits at Sandy Hook are shown in Figure 4.12). This indicates that the data misfits between the model simulated water levels and pseudo-observations are primarily contributed by the superimposed white noise. This experiment indicates that the optimal C_d converges to the true solution. However, the true C_d values cannot be exactly recovered since the effects of white noise. Thus, the observational noise has an impact on the determination of the optimal wind drag coefficients.

ITE_WDC3: *30-day continuous data assimilation with pseudo-observations*

This experiment is an extension of ITE_WDC1 to a 30-day continuous data assimilation for evaluating the performance of the data assimilation system with multiple control variables which vary in time and space. The initial guesses of the eight C_d components for the first day were again given as values of 20.0. The forward model was integrated from rest, and the restart file at the end of each data assimilation window (i.e., 24 hours) was created by model integration with the optimal C_d values of that day. The optimal C_d values were then used as the first guesses for the following 24-hour data assimilation procedure. Differences between the true and the optimal values of C_d are shown in Figure 4.13. It can be seen that, in general, the optimal values of C_d are close to their true solutions. Most of the differences between the true solution and the optimal values of C_d are less than 10^{-4}, and the maximum difference is 0.03. The norm of the gradient and the cost function during the 30-day assimilation period are presented in Figure 4.14 and Figure 4.15. The norm of the gradient and the cost function are small in magnitude, with the maximum values being 4.5×10^{-7} and 2.6×10^{-8}, respectively. This experiment demonstrates that the data assimilation system is successful in recovering multiple control variables from pseudo water level observations along the coast.

ITE_WDC4: *30-day continuous data assimilation with contaminated pseudo-observations*

The same data assimilation procedure as that used in the ITE_WDC3 experiment were performed, but the same contaminated pseudo-observations as that in ITE_WDC2 experiment were assimilated. The comparison between the true solutions and the optimal values of C_d are presented in Figure 4.16. In general, each optimal C_d component follows the trend of its true solution. However, on some days, the differences between the true solution and the optimal values of C_d are greater than 5.0, which are much greater than those of ITE_WDC3. As shown in Figure 4.17, the norm of the gradient is generally less than 10^{-4}, but is still much greater than that of ITE_WDC3 (with the exception of the maximum of 2.1×10^{-4} occurred on Julian Day 256). Cost function values (shown in Figure 4.18) vary in the range from about 0.7 to 0.9 during the 30-day assimilation period.

This experiment shows that the noise added to the pseudo-observations inhibits the optimal C_d from converging to their true solution. The noise ratio (defined as the ratio of the standard deviation of noise to that of observation) at the 18 water level stations varies from a maximum of 0.63 at Eastport to a minimum of 0.21 at Springmaid Pier. The results of this experiment show that the amplitude of the noise added to the pseudo-observations is too large compared with amplitude of the pseudo-observations to recover the true C_d solution exactly. In order to demonstrate this, another experiment was performed in which noise with zero mean and standard deviation of 0.014m was added to the pseudo-observations at all of the 18 stations (the mean noise ratio is about 0.1). The optimal C_d values for this case are much closer to the true solution than that of ITE_WDC4, but the differences between the true solution and the optimal values of C_d still exist. The maximum values of the norm of the gradient and the cost function are 1.7×10^{-5} and 0.05, respectively. The results show that any observational error can cause the optimal C_d not to converge exactly to the true solution. The smaller the noise ratio, the closer the optimal C_d is to the true solution.

4.3. Effects of Spatial Distribution of Observational Stations

A sensitivity test of the identical twin experiment can be used to demonstrate how the spatial distribution of water level stations influences the result of optimization process. In general, any perturbation of a control variable should be correctly represented by the change in the cost function. In other words, any change of a control variable should result in a change of the water levels which are used to compute the cost function. Otherwise, the gradient of the cost function will be zero, and the optimization procedure fails to find the meaningful optimal control variables since the convergence criterion is already satisfied. Since the selected water level stations (in the ECDA model) are all close to the coast, a perturbation of the wind drag coefficients at the area far away from the coast may not be reflected in the changes of the water levels at these water level stations within the data assimilation window, in other words, the changes of the wind drag coefficients at an area far away from water level stations may not result in any water level change at the coastal stations. This results in the zero gradient of the cost function, and therefore optimization process stops successfully but fails to find meaningful optimal control variables. In this section, three experiments were performed to demonstrate the influence of choosing the number and distribution of water level stations in the optimization process. According to the control variable definition, the model domain was divided into eight regions, and each region is associated with a control variable (see Figure 2.1). The number of water level stations in each region for these three experiments is listed in Table 4.4.

A 30-day continuous data assimilation identical twin experiment was conducted with eight control variables and pseudo-observations from 15 water level stations (denoted as ITE_DOS1). Note that there are no stations in Regions 2 and eight. The optimal values of C_d (shown in Figure 4.19) are different from the true solutions on day 250 since the optimization procedure could not find better values of C_d than those of day 249. After day 250, the optimal values of C_d in regions 3-7 converge to their true solutions again. In Regions 1 and 2, the error of the optimal C_d on day 250 leads to an overshoot on day 251, before gradually converging to their true solutions. In Region 8, the optimal C_d converges to its true value after 6 days.

Table 4.4. Distribution of the water level stations in model domain

	Region1	Region2	Region3	Region 4	Region5	Region6	Region7	Region8
ITE_DOS1	5	0	3	1	1	4	1	0
ITE_DOS2	5	0	5	2	2	4	2	0
ITE_WDC3	5	0	4	1	1	3	2	2
ITE_DOS3	pseudo-observation is available at every model grid point.							

For ITE_DOS2 experiment, pseudo-observations from 20 water level stations were used, but there are still no stations in Regions 2 and 8. Similar results as ITE_DOS1 are obtained. The optimal values of C_d from the optimization on day 250 are still different from the true solutions. Keep in mind that for ITE_WDC3 of Section 4.2.2 (18 total stations, 2 in Region 8 and none in Region 2), the optimal values of C_d converged to their true solutions exactly. This indicates that spatial distribution of the water level stations has a significant effect on the results of the optimization. This is part of the reason why the wind drag coefficients were defined in this way in the ECDA domain.

Another experiment (ITE_DOS3) was performed in which the hourly pseudo-observations (water level only) from all of the water cell grid points (total 9794) were used in the data assimilation. The results from this experiment show that the maximum difference between the true and the optimal values of C_d is less than 10^{-4} during the 30 day data assimilation period. A comparison of errors of the optimal C_d for this experiment with those for ITE_WDC3 in Section 4.2.2 is shown in Figure 4.20. Errors are now observed to be close to zero for this experiment, but there appear some larger errors for the ITE_WDC3. A comparison of the cost function for this experiment with that for ITE_WDC3 (shown in Figure 4.21) shows that the cost function has been significantly reduced on days 250 and 257 for this experiment. Aside from these two days, values of the cost function from the two experiments are the same order of magnitude. Therefore, within a preset accuracy criterion, the number of representative observations does not have a significant effect on the cost function. So we can use a minimum number of representative observations to obtain similar results with using more observations. This is encouraging for designing a reasonable and efficient observation system.

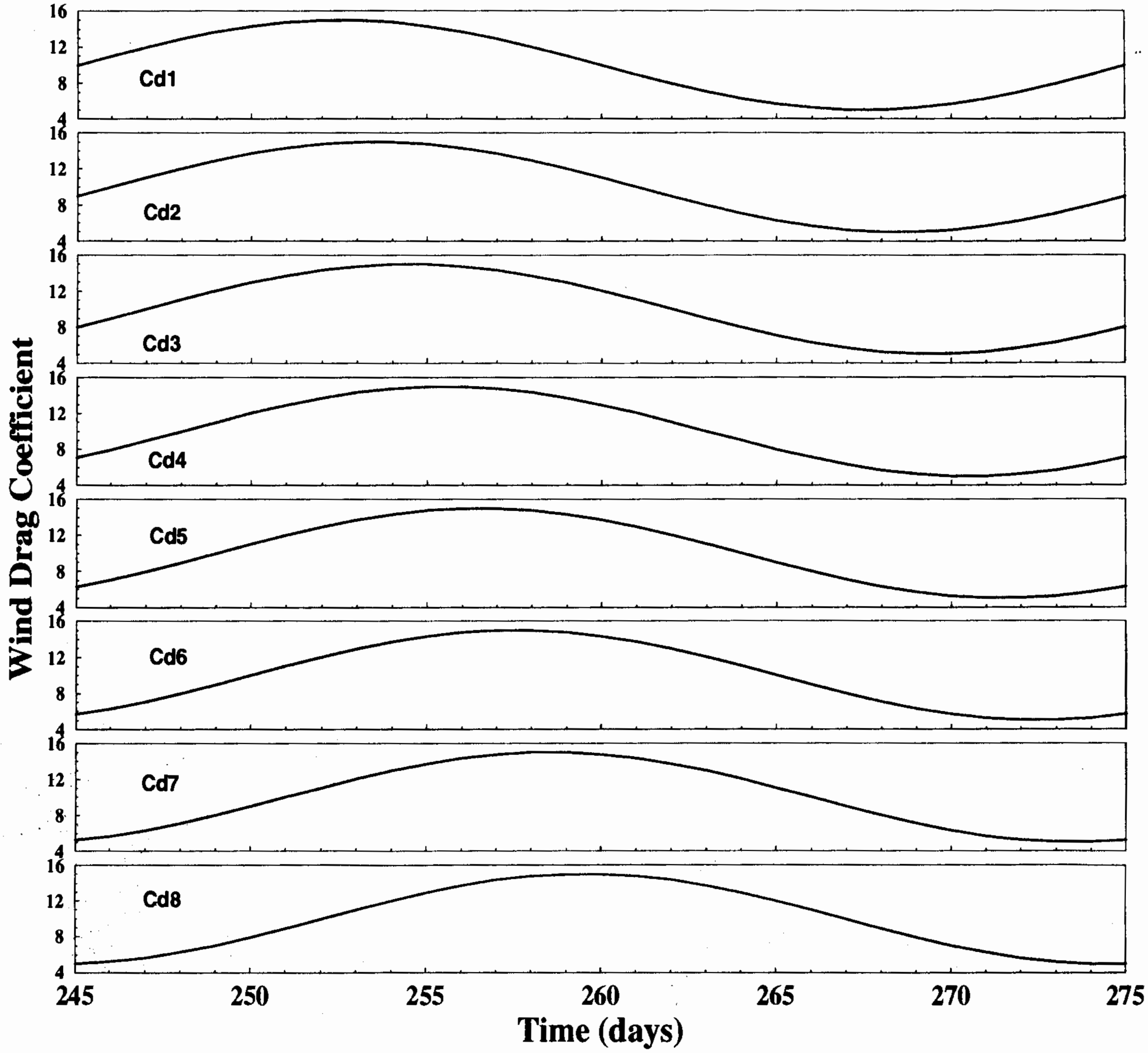

Figure 4.1. Time series of hypothetical wind drag coefficients for the identical twin experiment with eight control variables.

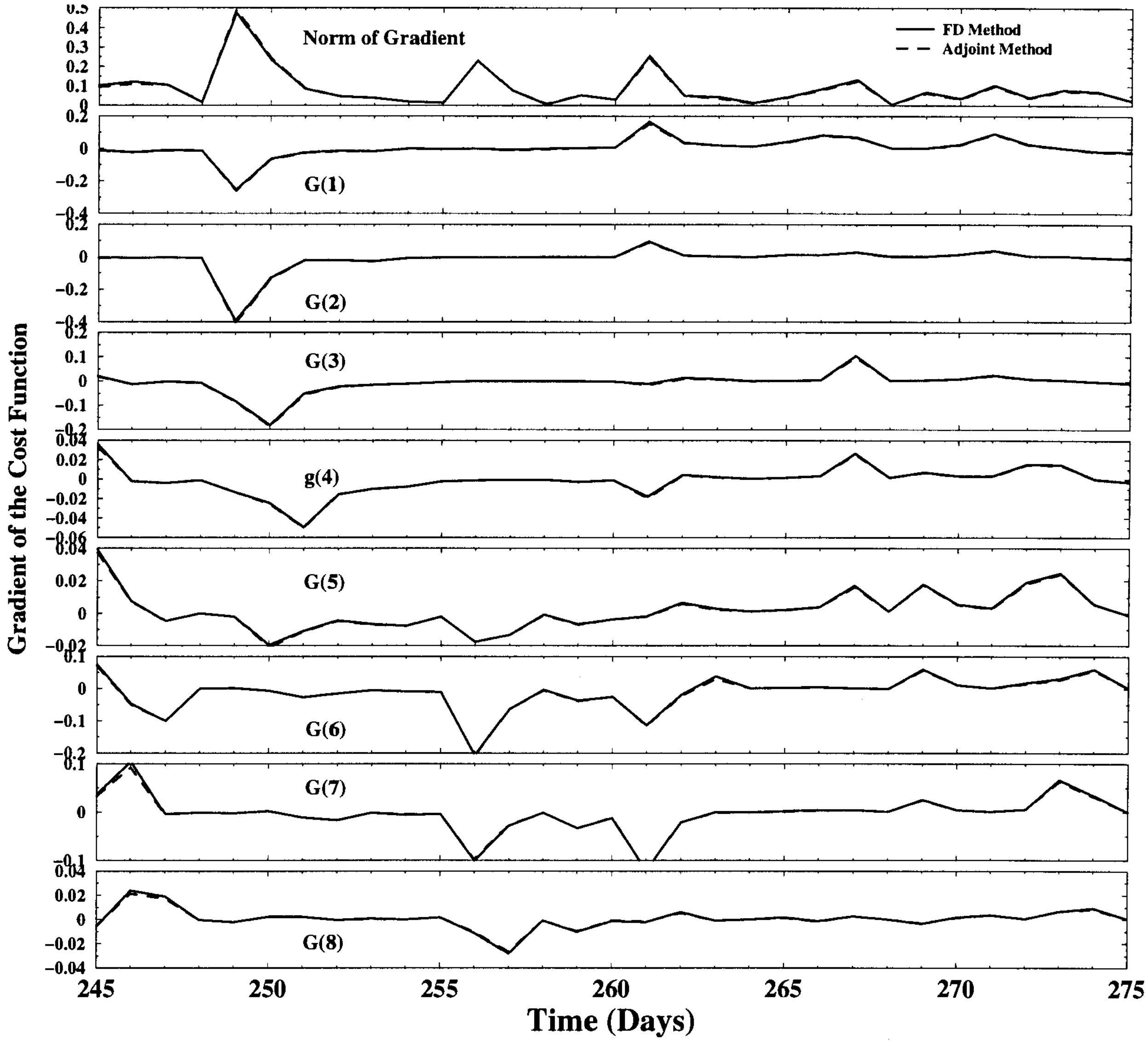

Figure 4.2. Time series of the norm of the gradient and the gradient components calculated by both the finite difference and adjoint methods.

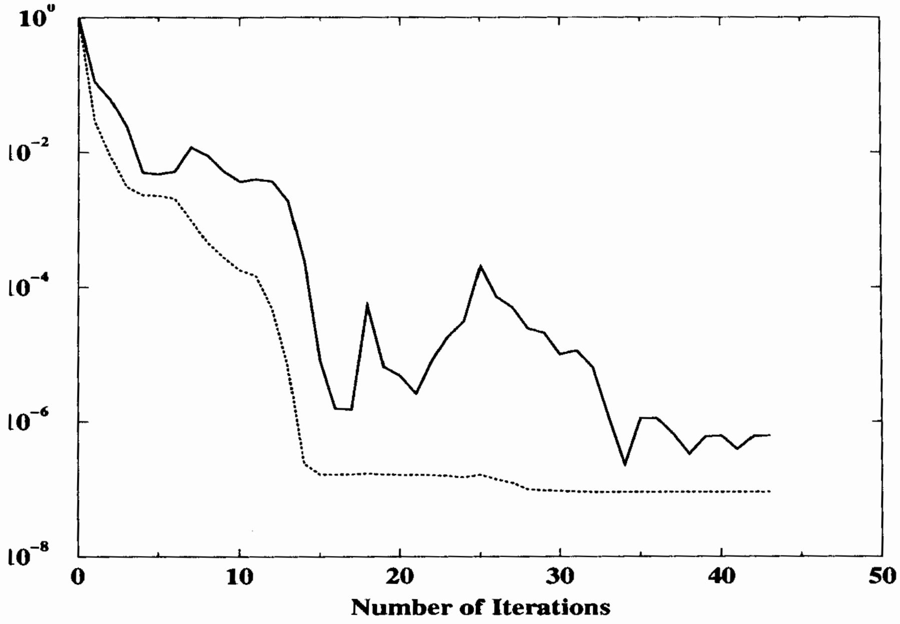

Figure 4.3. Norms of the gradient (solid line) and cost function (dotted line) versus the number of iterations.

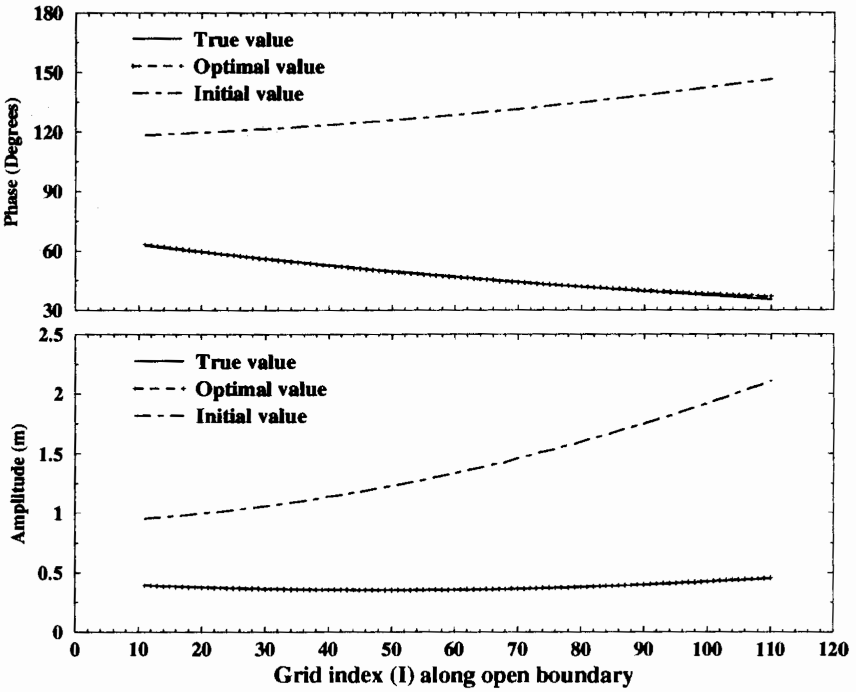

Figure 4.4. Amplitudes and phases along the open boundary in the twin experiment. Solid line, true values; dashed line with plus, optimal values; dashed line, initial values.

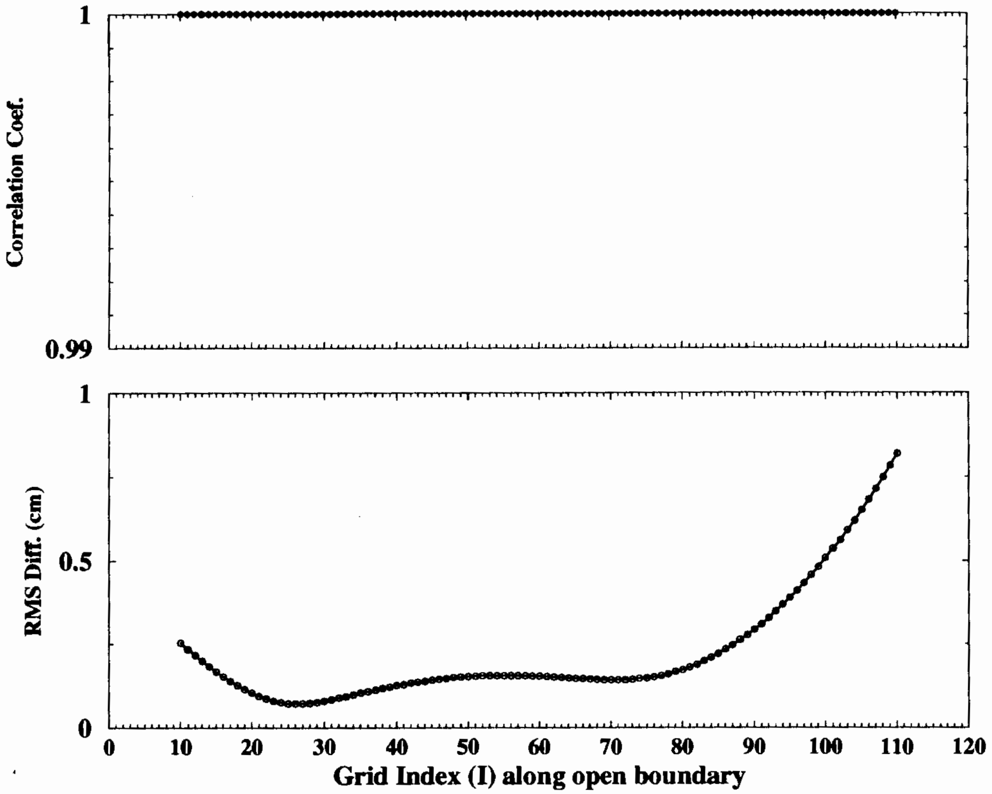

Figure 4.5. RMS errors and correlation coefficients between true open boundary elevations and optimal open boundary elevations.

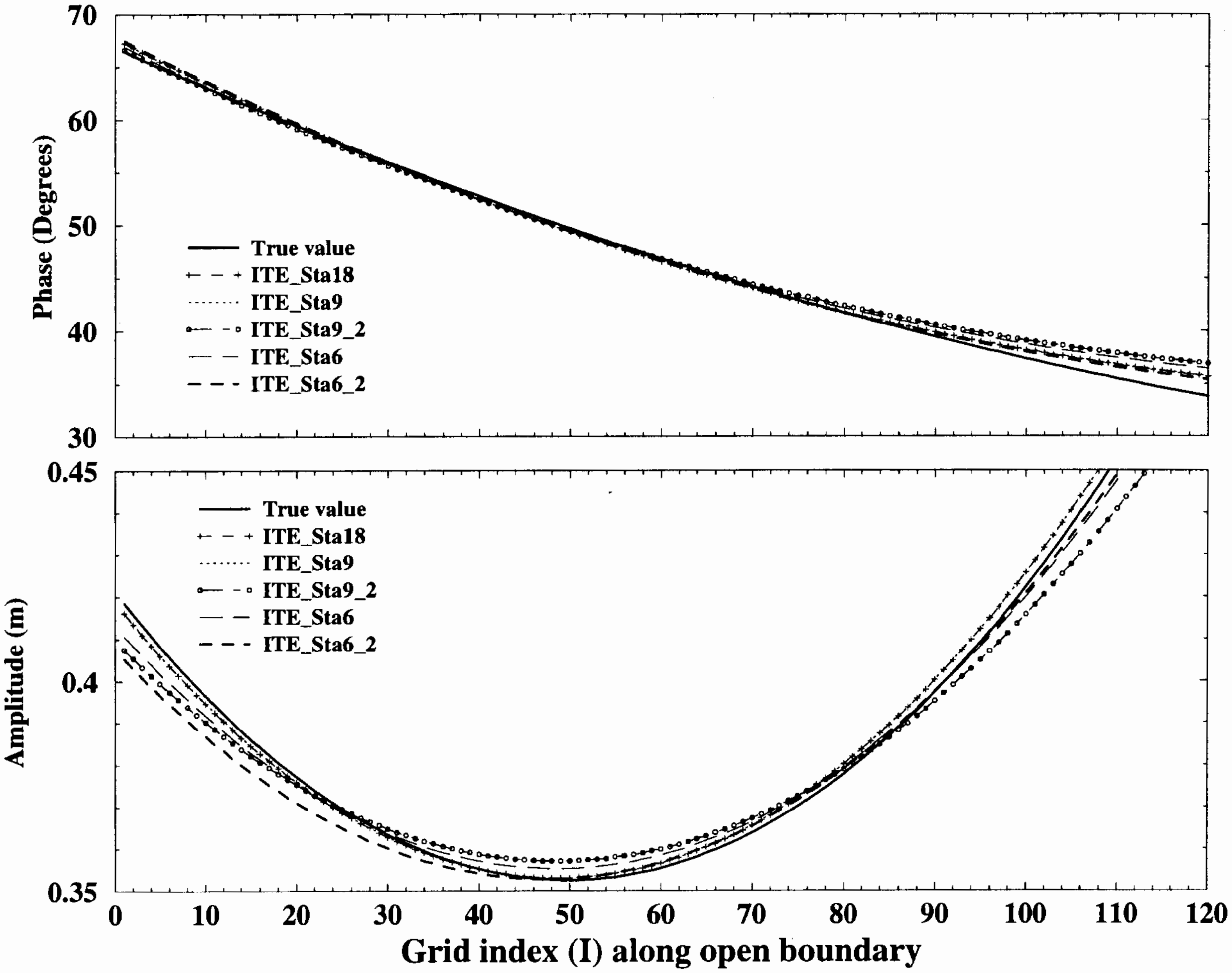

Figure 4.6. True and optimal amplitudes and phases at the open boundary from various twin experiments.

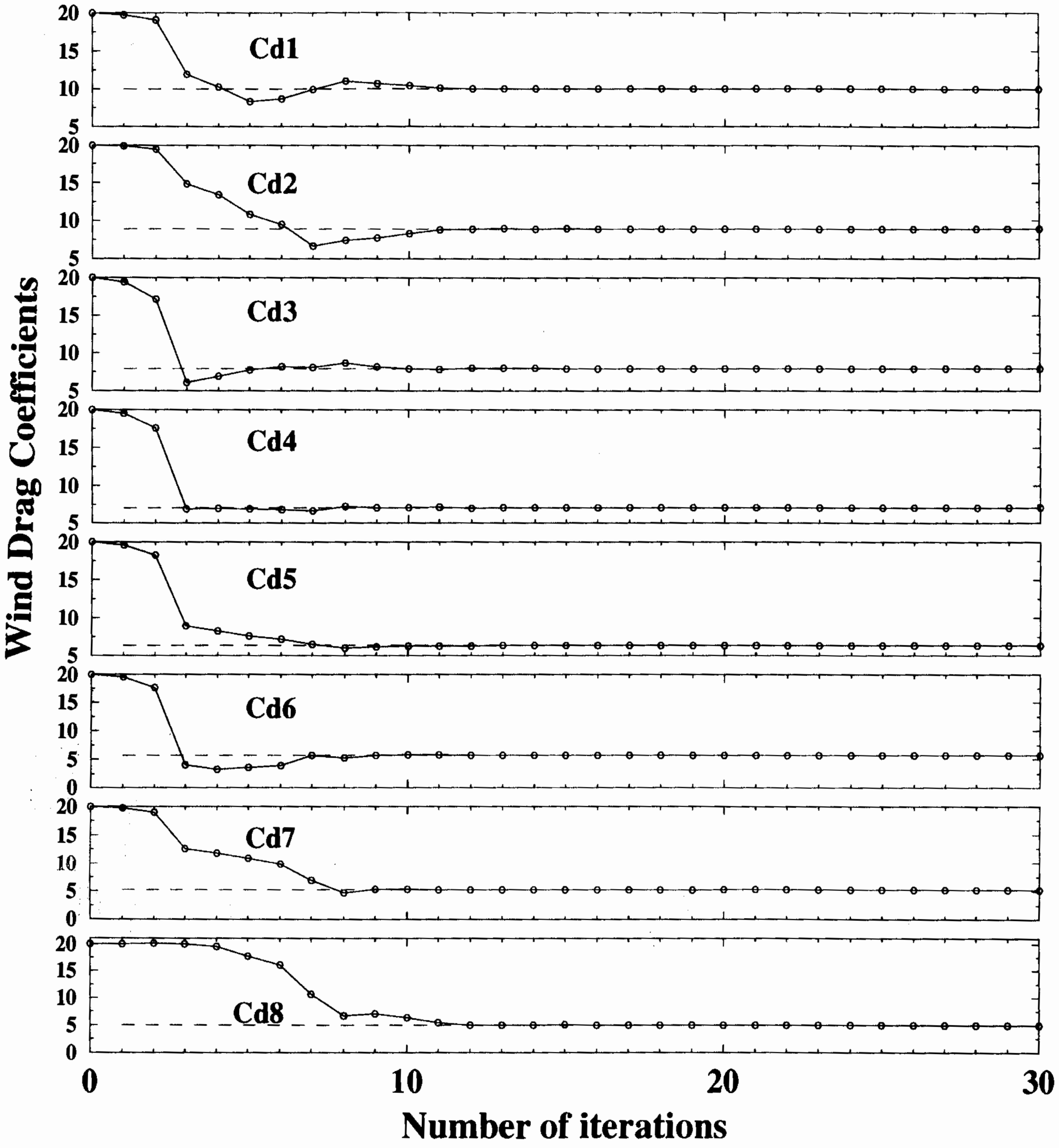

Figure 4.7. Variation of the optimal C_d during a one-day identical twin experiment with eight control variables and pseudo-observations. Solid line, optimal values; dashed line, true values.

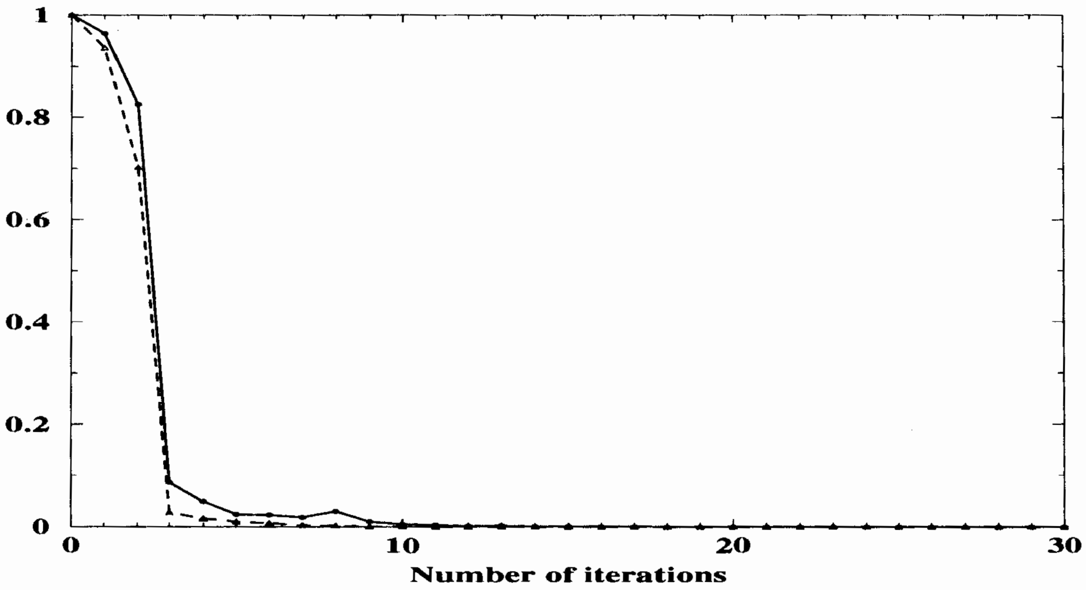

Figure 4.8. Variation of the norm of the gradient $|G|/|G_0|$ and the cost function J/J_0 (scaled by their initial values $\|G_0\|$ and J_0) with the number of iterations for a one-day identical twin experiment with eight control variables and pseudo-observations. Solid line, gradient; dashed line, cost function.

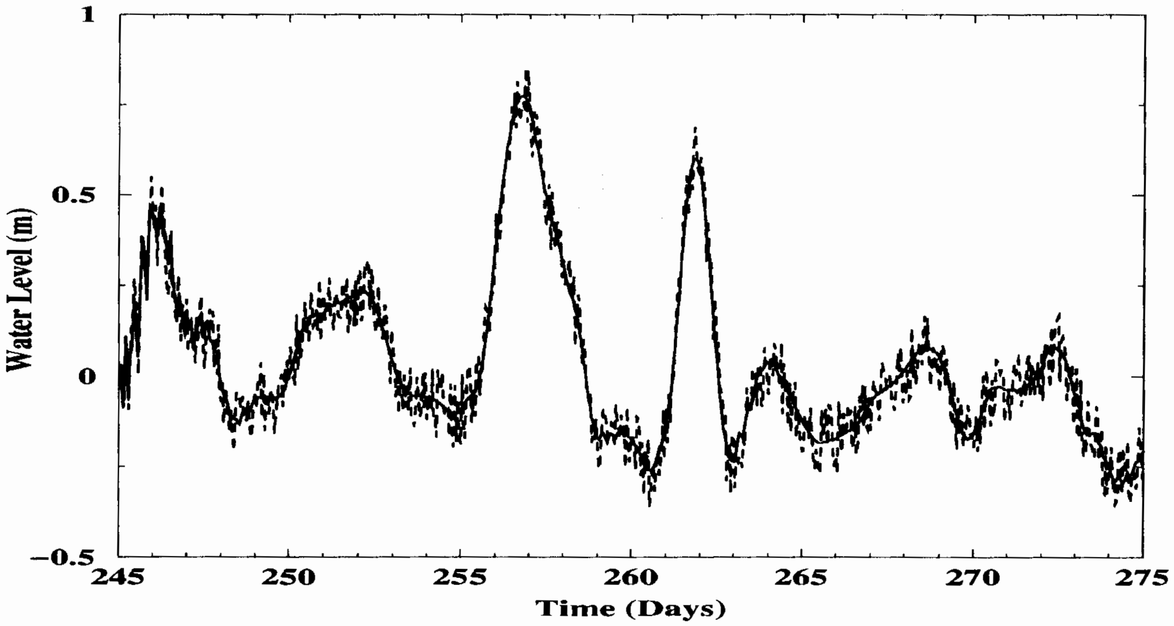

Figure 4.9. An example of the original (solid line) and contaminated (dashed line) pseudo-observations at Sandy Hook.

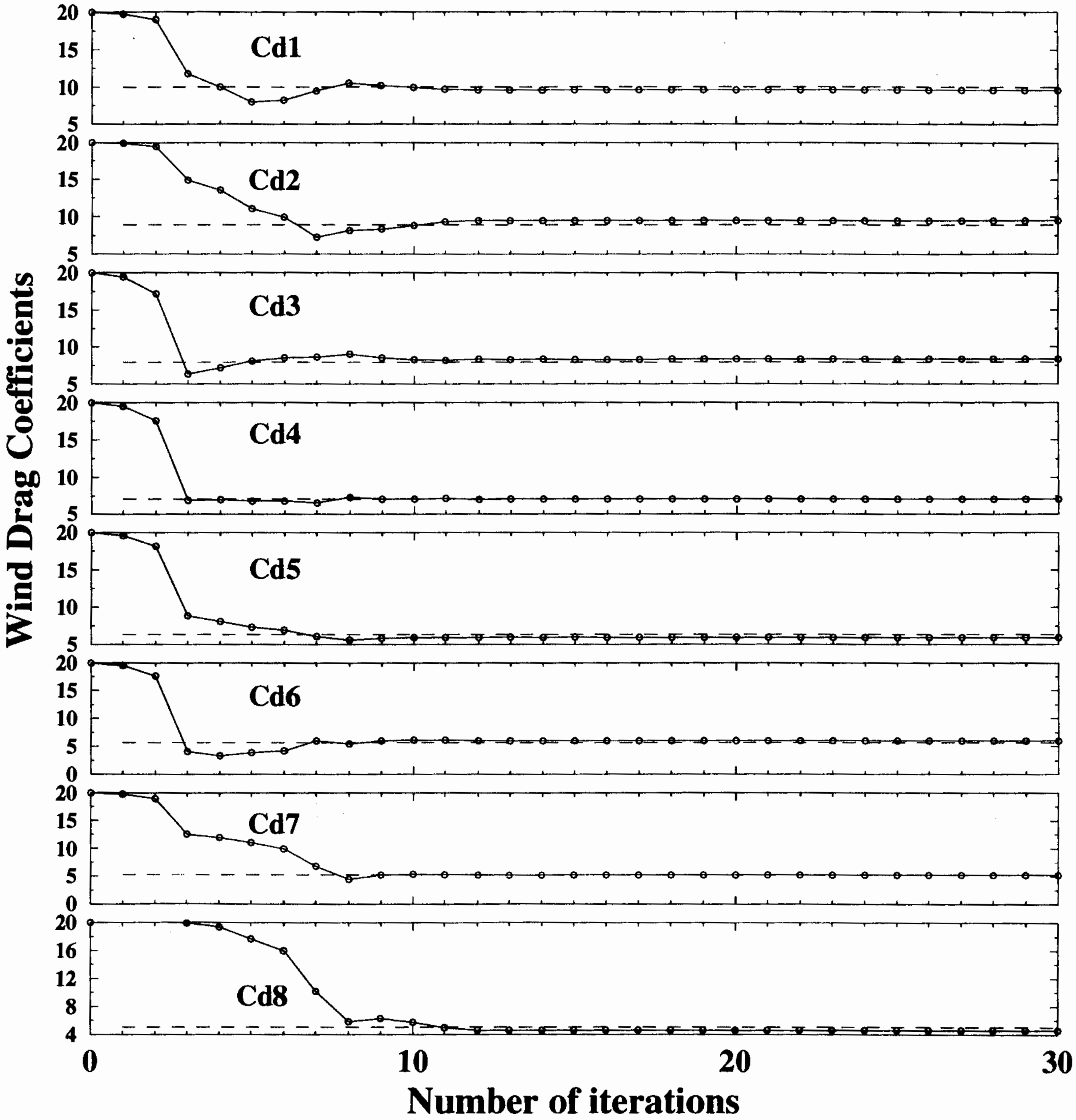

Figure 4.10. Variation of C_d during the iterative process for the one-day identical twin experiment with eight control variables and contaminated pseudo-observations. Solid line, optimal values; dashed line, true values.

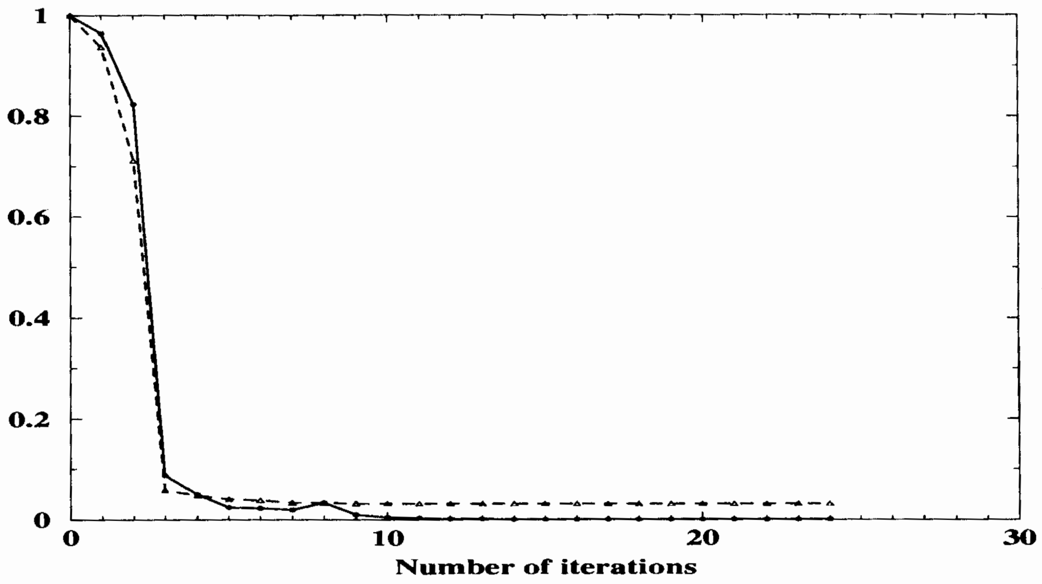

Figure 4.11. Variation of the norm of the gradient $|G|/|G_0|$ and the cost function J/J_0 (scaled by their initial values $\|G_0\|$ and J_0) with the number of iterations for a one-day identical twin experiment with eight control variables and contaminated pseudo-observations. Solid line, gradient; dashed line, cost function.

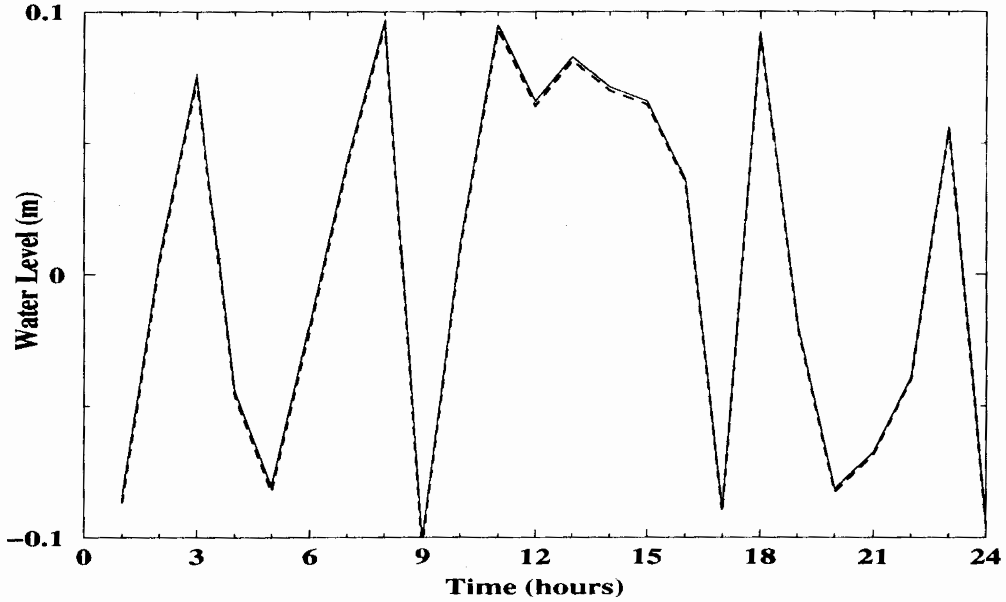

Figure 4.12. Comparison between the white noise (solid line) and data misfits (dashed line) after four iterations at Sandy Hook.

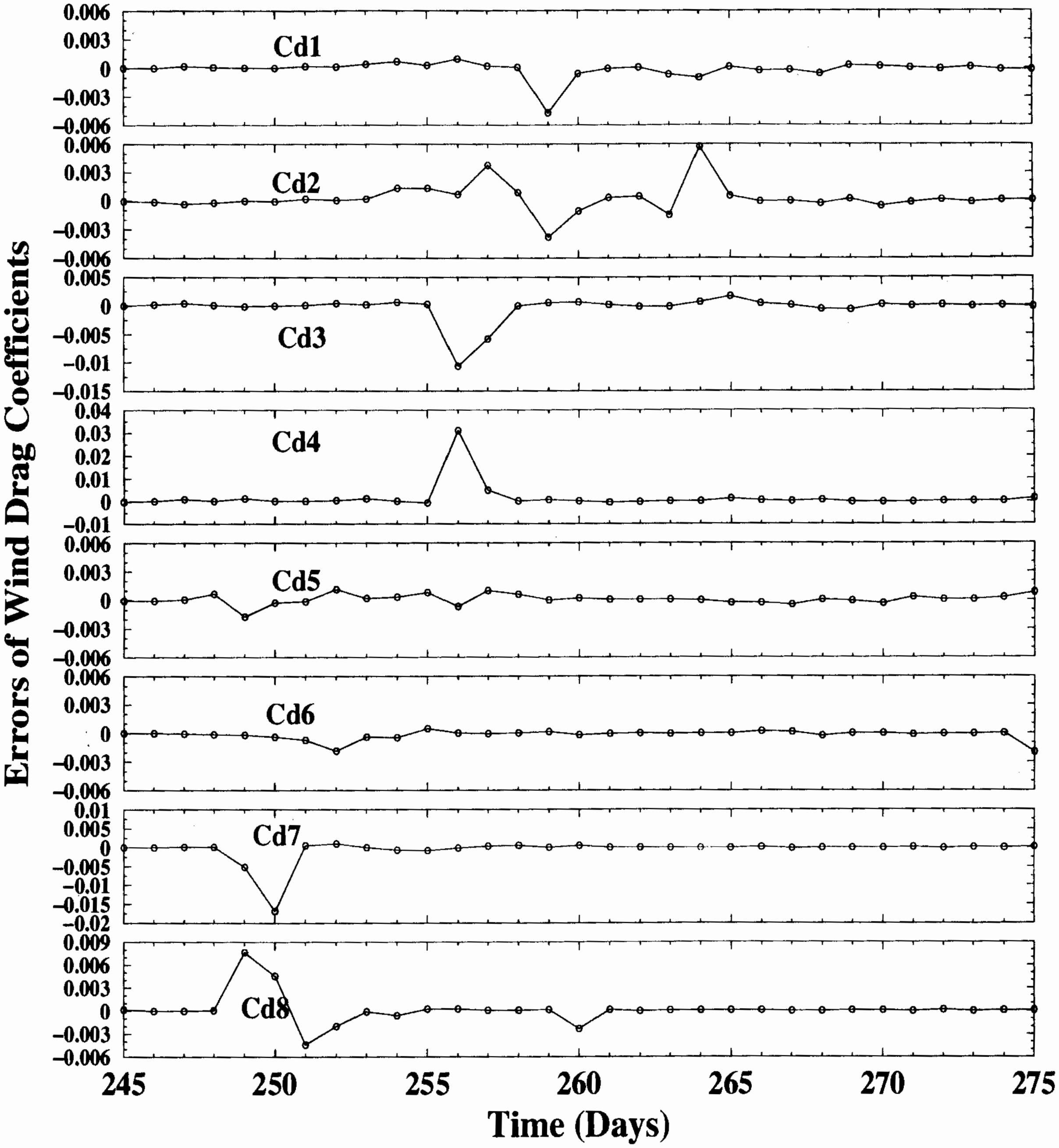

Figure 4.13. Time series of the differences between the true solution and the optimal C_d from the 30-day identical twin experiment of ITE_WDC3.

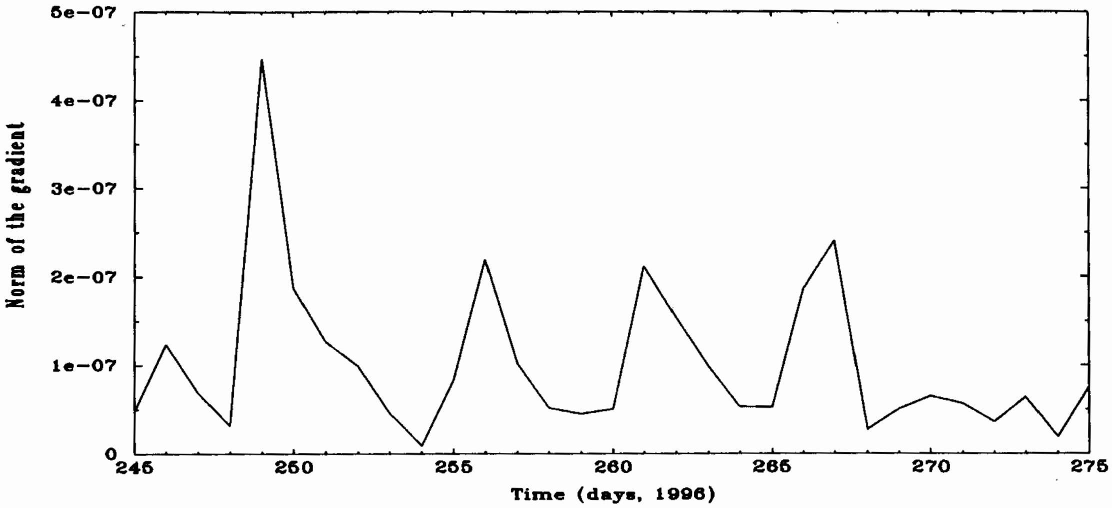

Figure 4.14. Time series of the norm of the gradient from a 30-day identical twin experiment with eight control variables and pseudo-observations (ITE_WDC3).

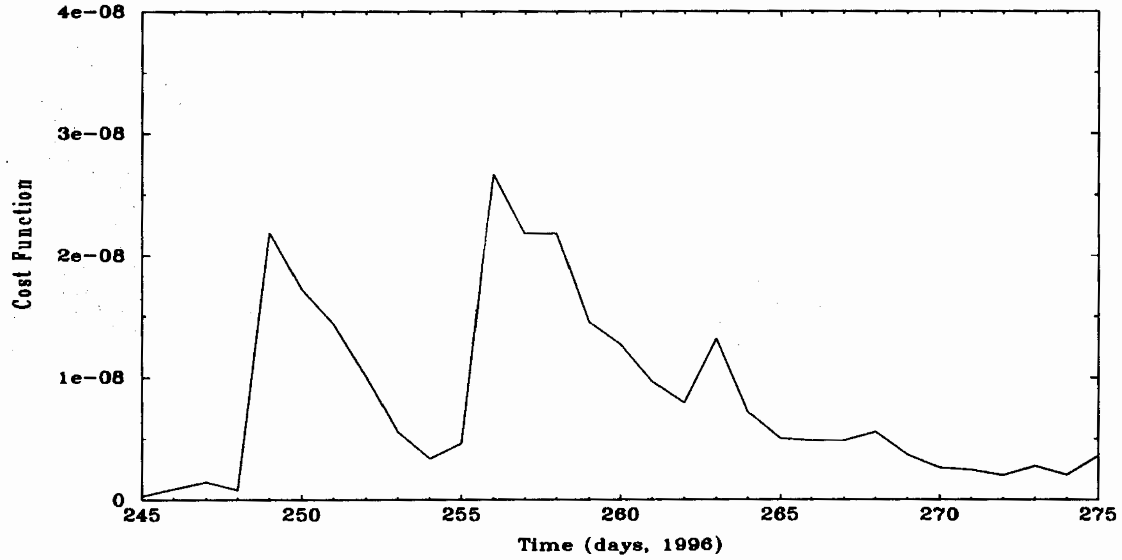

Figure 4.15. Time series of the cost function from a 30-day identical twin experiment with eight control variables and pseudo-observations (ITE_WDC3).

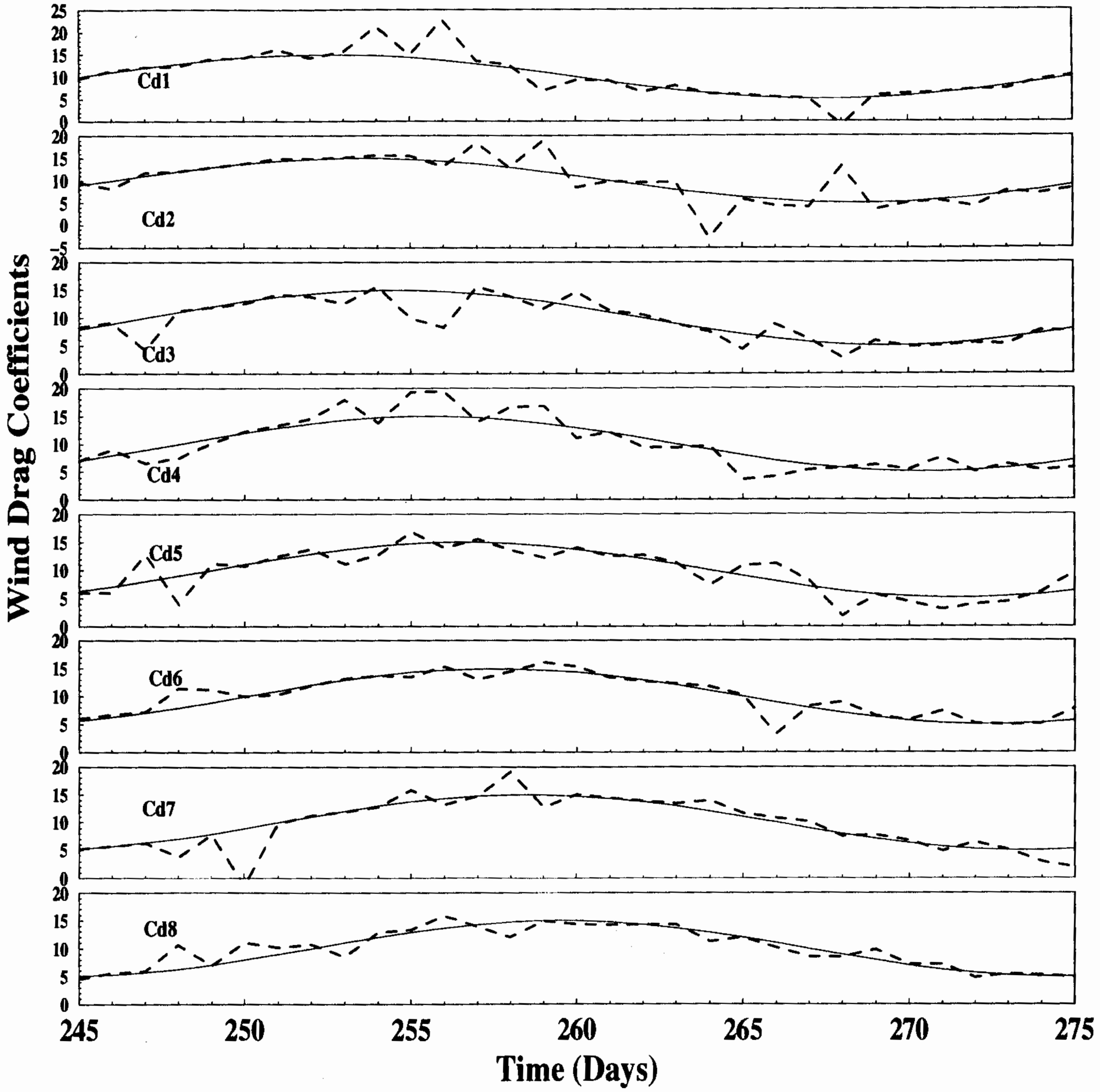

Figure 4.16. Time series of the true solution (solid line) and the optimal values (dashed line) of C_d from a 30-day identical twin experiment with eight control variables and contaminated pseudo-observations (ITE_WDC4).

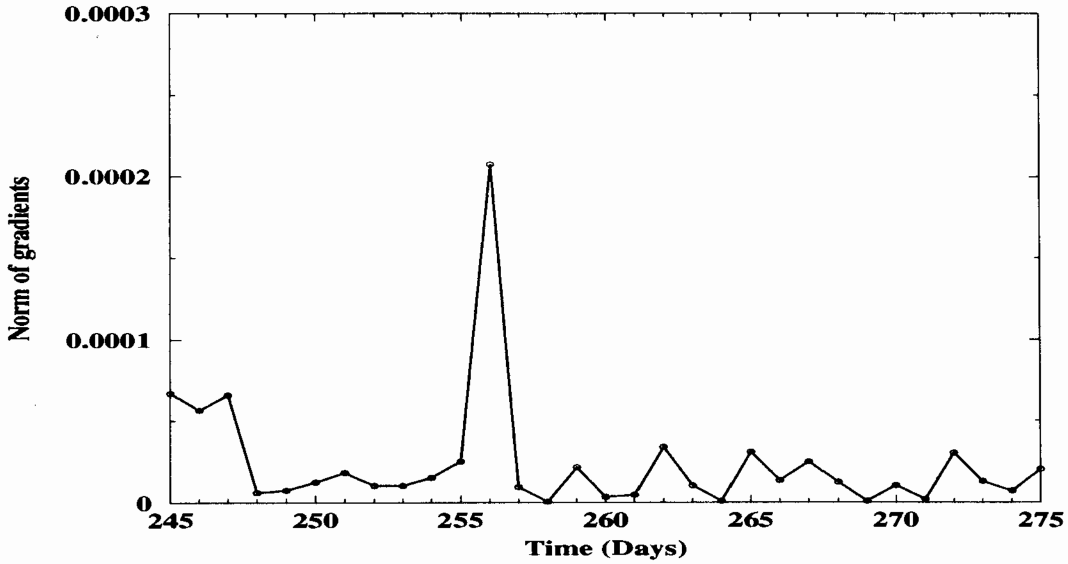

Figure 4.17. Time series of the norm of the gradient from a 30-day identical twin experiment with eight control variables and contaminated pseudo-observations (ITE_WDC4).

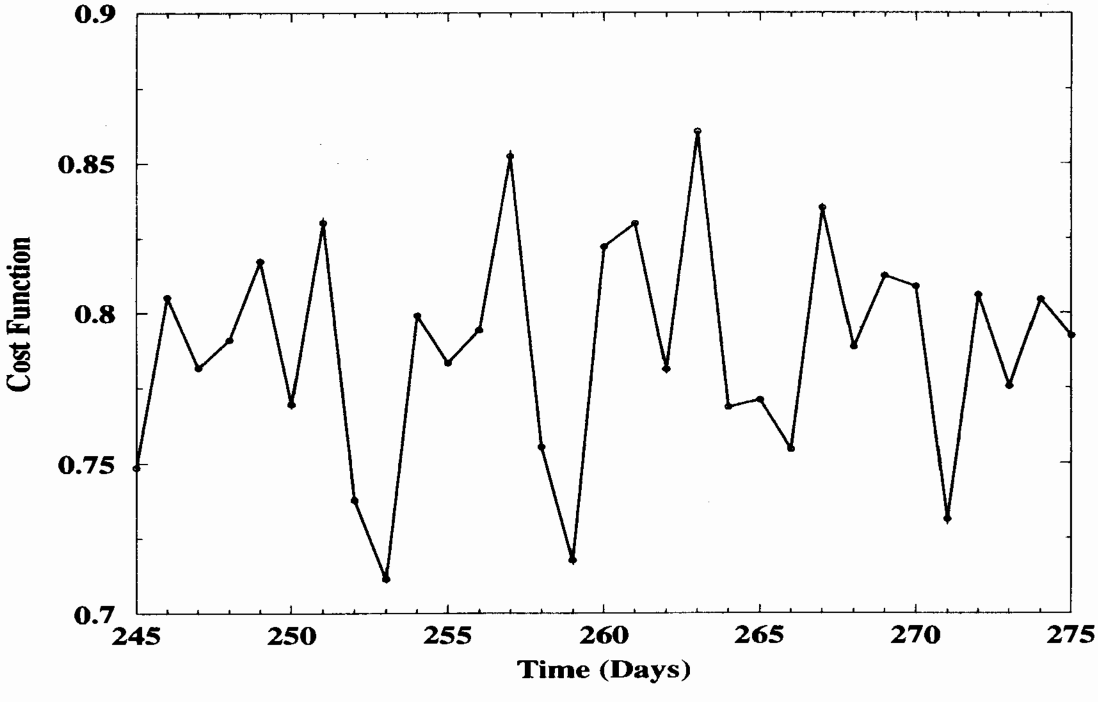

Figure 4.18. Time series of the cost function from a 30-day identical twin experiment with eight control variables and contaminated pseudo-observations (ITE_WDC4).

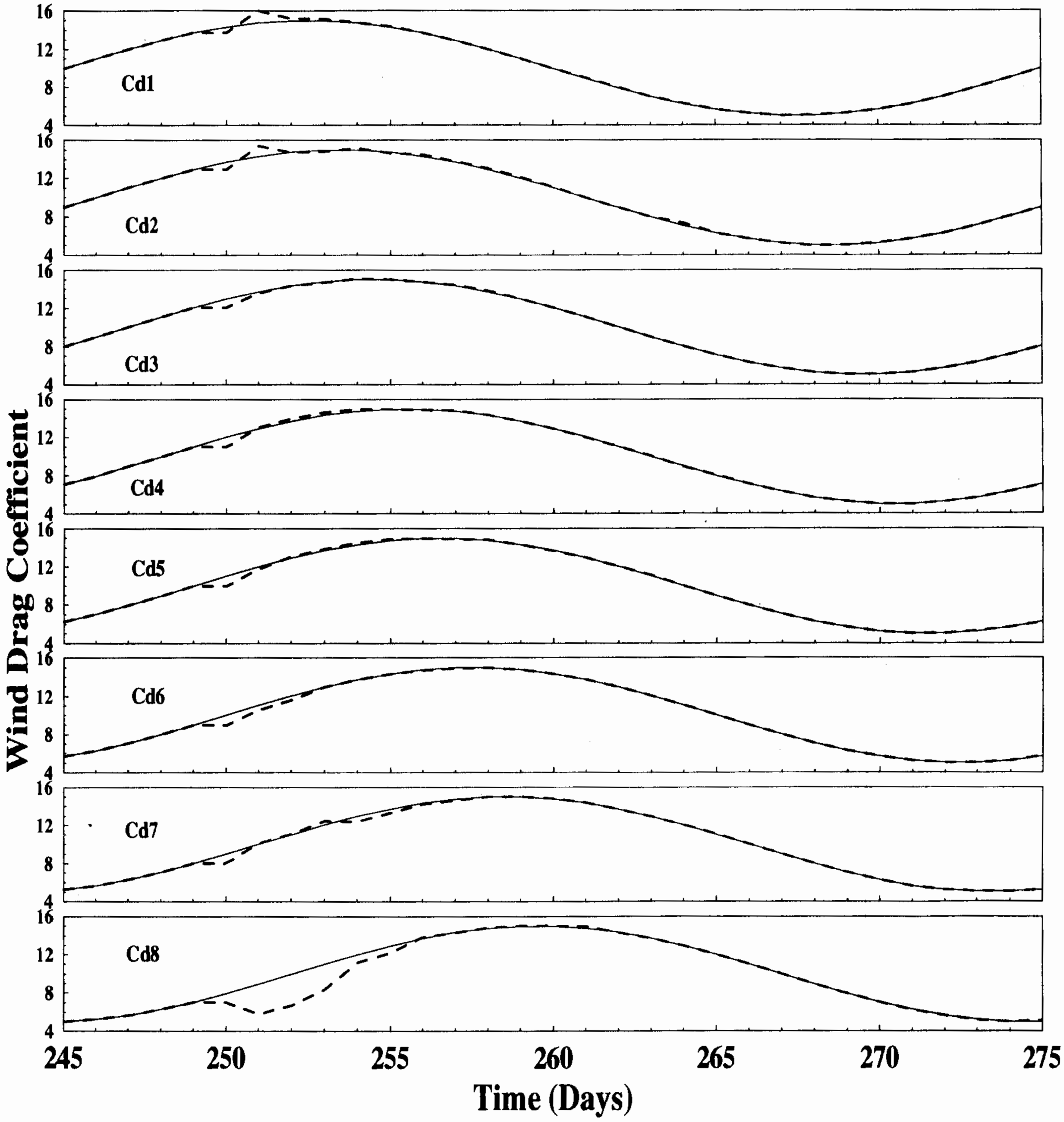

Figure 4.19. Time series of the true values (solid line) and optimal values (dashed line) of C_d from a 30-day identical twin experiment with 15 stations (ITE_DOS1).

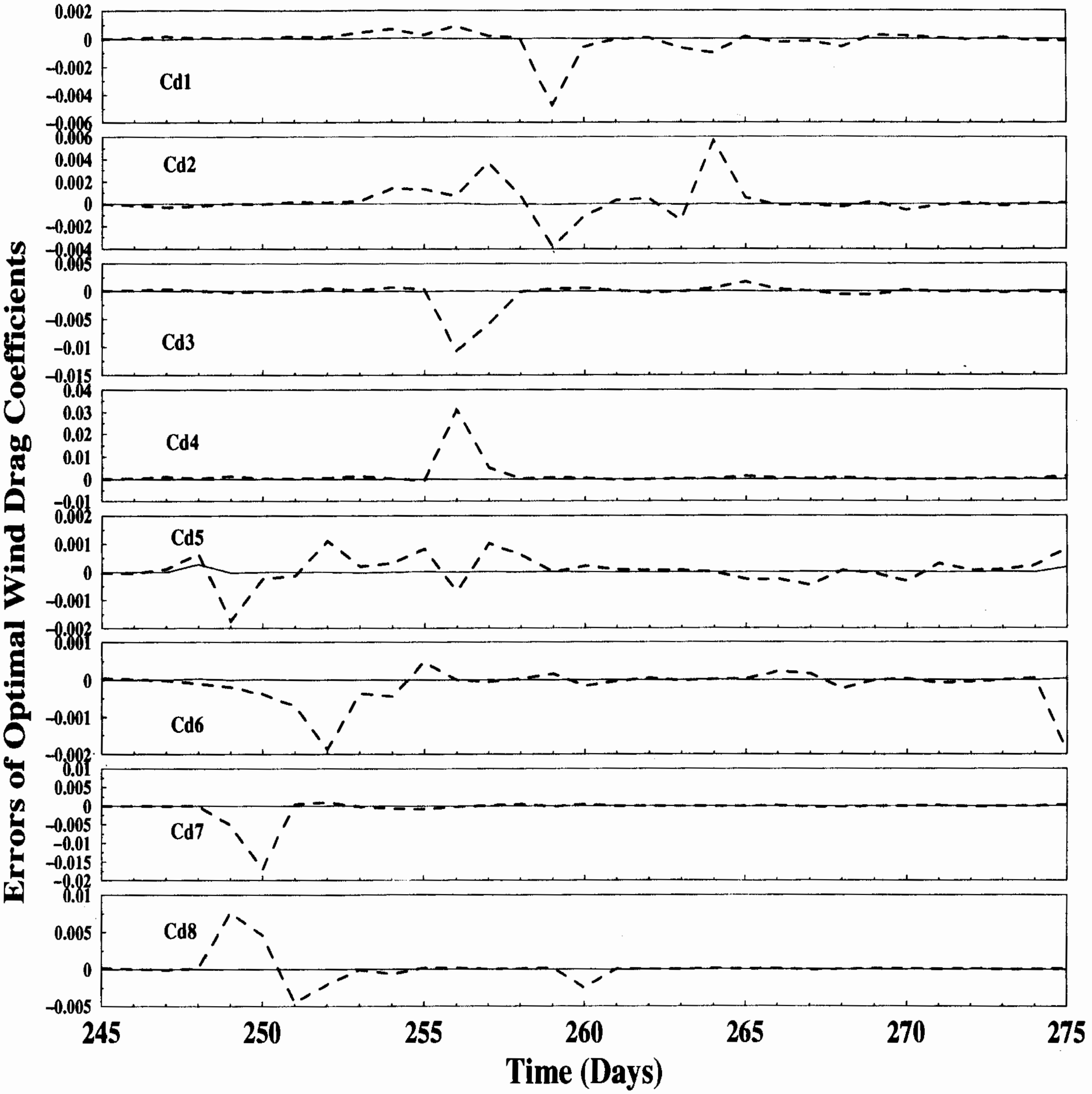

Figure 4.20. Comparison of the errors in the optimal values of C_d. The solid line represents the differences between the true and the optimal values of C_d from the identical twin experiment in which pseudo-observations are available at every grid point inside the model domain (ITE_DOC3). The dashed line represents the difference between the true and the optimal values of C_d from the identical twin experiment of ITE_WDC3.

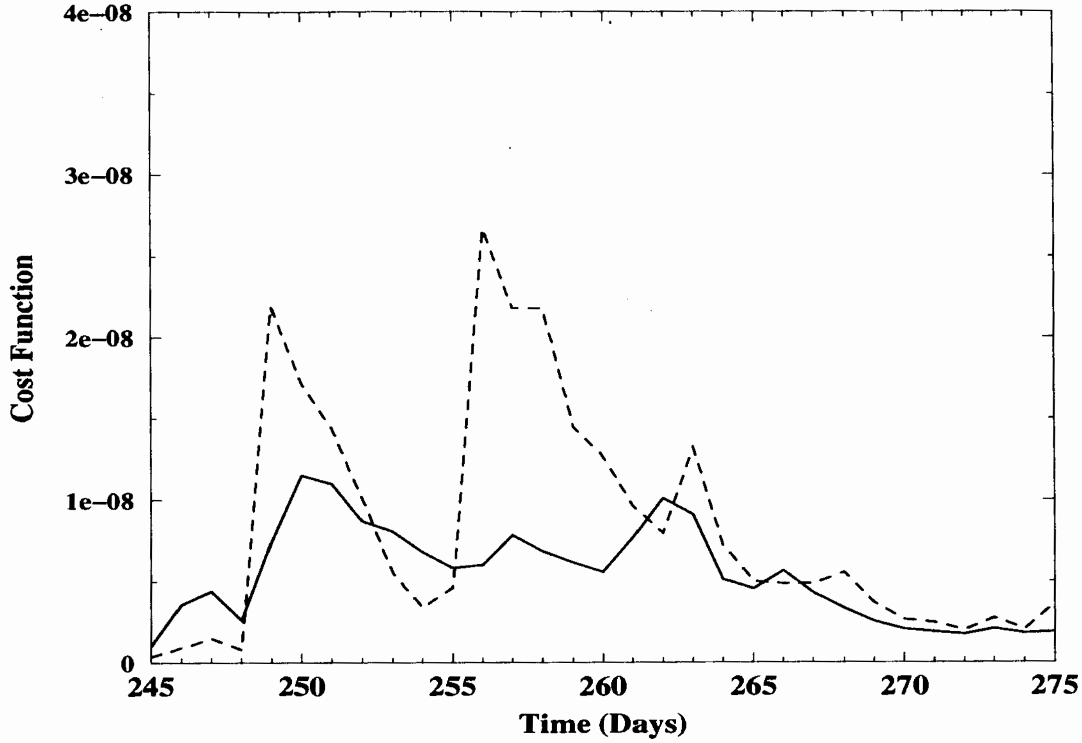

Figure 4.21. Time series of the cost function from the identical twin experiments ITE_WDC3 (solid line) and ITE_DOS3 (dashed line).

5. PRACTICAL APPLICATION

5.1. Optimal Estimation of Tidal Open Boundary Conditions

To understand the importance of each tidal constituent along the U. S. East Coast, the harmonic constants for 37 tidal constituents at tide gauge stations along the coast are analyzed. These constants were calculated by the Center for Operational Oceanographic Products and Services (CO-OPS) of NOAA from long-term water level observations using the least square harmonic analysis method. The ratio of the potential energy of each tidal constituent to the total potential energy of all 37 tidal constituents is defined as:

$$\gamma_{PE} = \frac{A_i^2}{\sum_{i=1}^{37} A_i^2} \tag{5.1}$$

where A_i is amplitude of each tidal constituent. The potential energy ratios of the five major tidal constituents (M_2, S_2, N_2, K_1, O_1) at 18 tidal gauge stations are listed in Table 5.1. We can see that more than 80% of the potential tidal energy is generally contributed by the M_2 constituent, and more than 94% potential tidal energy is contributed by the five major tidal constituents. In this section, we therefore focus on the open boundary optimization of these five major tidal constituents.

Table 5.1. Potential energy ratios (expressed as percent) of the major 5 tidal constituents at 18 tidal gauge stations

Sta.#	M_2	S_2	N_2	K_1	O_1	$\sum of 5$
1	85.521	4.624	4.929	1.252	0.795	97.121
2	82.693	3.200	4.890	3.472	1.669	95.925
3	90.081	2.558	4.292	0.769	0.404	98.104
4	78.474	3.784	5.590	4.773	2.330	94.950
5	89.663	2.691	4.339	0.666	0.318	97.677
6	87.445	3.417	4.488	2.007	0.531	97.889
7	85.499	3.352	4.639	2.969	1.403	97.863
8	88.213	2.729	4.224	2.011	1.166	98.343
9	86.655	2.722	3.992	2.478	1.734	97.582
10	85.786	2.696	4.213	1.712	0.951	95.358
11	85.708	3.023	4.373	1.922	1.220	96.247
12	85.263	3.059	4.677	2.993	1.316	97.308
13	83.436	2.734	4.568	3.593	2.287	96.618
14	86.239	2.828	4.629	1.622	0.907	96.226
15	87.841	2.624	4.264	1.654	0.930	97.312
16	85.801	2.412	4.347	1.316	0.705	94.581
17	85.090	2.436	5.159	1.981	1.035	95.700
18	83.445	2.048	4.421	3.185	1.851	94.949

Two experiments denoted as individual tidal constituent estimation (PA_ITC) and combined tidal constituents estimation (PA_CTC) are performed. For the first, the same data assimilation procedure as that of the identical twin experiment ITE_Sta9 is individually applied for each of the five tidal constituents to the obtain optimal open boundary conditions of each tidal constituent. Here 5 control variables in total are used for each constituent within each data assimilation process based on the results of the identical twin experiments (model simulation is not sensitive to a_6). The optimal harmonic constants of these five tidal constituents from the separate data assimilation processes are then combined and used as the lateral open boundary conditions for a new simulation run. For the latter, the harmonic constants of the five tidal constituents are estimated in one data assimilation process at the same time(25 control variables in total). Thus the interaction among the tidal constituents is included while the tides propagate into shallow coastal region. Based on the results of the identical twin experiments, the experiment ITE_Sta9 in which data from the nine coastal stations were assimilated got almost the same results as the experiment ITE_Sta18. And topography and geometry inside bays or inside rivers cannot be well resolved by the present model grid resolution, so this may cause the model results at grid points inside shallow bays not to match the corresponding observations well. Therefore, tidal predicted elevations (calculated by using the harmonic constants of the corresponding constituent from CO-OPS) from the 9 stations of ITE_Sta9 are used in the data assimilation process, and elevations from the additional 9 stations from ITE_Sta18 are used as references. Harmonic constants of each tidal constituent from Schwiderski's global tide model are interpolated along the open boundary and then used as initial values of the control variables.

5.1.1. Optimal Control Variables

The optimal quadratic polynomial coefficients of the amplitude and phase from experiment PA_ITC are listed in Table 5.2. The optimal harmonic constants (amplitude and phase) of these 5 major tidal constituents along the open boundary are compared with the initial values from Schwiderski's global tide model in Figure 5.1. It can be seen that the optimal amplitudes of the M_2, S_2, K_1 and O_1 constituents along the open boundary from the two data assimilation experiments PA_CTC and PA_ITC are close, but about 2 cm greater of the PA_CTC than PA_ITC for N_2. The optimal amplitudes of M_2, S_2 are close to those of Schwiderski's global tide model results. The optimal phases of M_2 from the two experiments are very close and smaller than those of Schwiderski's global tide model from 5° at southwest to 20° at northeast. There are almost 10° differences of the optimal phases of S_2 and N_2 between the two experiments PA_ITC and PA_CTC, and they are smaller than those of Schwiderski's global tide model results. The optimal phases of O_1 from the two experiments are very close, and they are greater than those of Schwiderski's model results.

Table 5.2. Optimal quadratic polynomial coefficients (Eq. 3.1 and 3.2) for the amplitude and phase of the five major tidal constituents from experiment PA_ITC

Constituent	a_1	a_2	a_3	a_4	a_5
M_2	0.409	-0.301	0.332	0.123	-0.385
S_2	0.601	-0.384	0.889	0.321	-0.279
N_2	0.819	-0.585	0.546	0.341	-0.230
K_1	0.870	-0.202	0.060	0.206	-0.274
O_1	0.568	0.726	-0.217	0.230	-0.442

Table 5.3. Comparison of observed and computed harmonic constants (amplitude, A, in centimeters and local phase, θ, in degrees) of M_2, S_2, N_2, K_1, O_1 at 18 tide gauge locations

Station	M_2				S_2				N_2				K_1				O_1			
	Obs.		MODEL		Obs.		MODEL		Obs.		MODEL		Obs.		MODEL		Obs.		MODEL	
	A	θ	A	θ	A	θ	A	θ	A	θ	A	θ	A	θ	A	θ	A	θ	A	θ
Boston	139.5	109	141.5	108	22.0	146	20.6	151	30.7	77	30.3	79	15.0	205	10.0	197	11.9	186	7.9	193
New London	36.6	58	44.7	53	7.2	69	6.7	73	8.9	34	10.2	25	7.5	179	8.4	187	5.2	203	6.2	190
Newport	52.9	1	58.5	1	12.3	23	10.1	34	12.7	344	14.4	348	6.4	168	8.5	169	5.1	198	6.3	175
Bridgeport	98.5	108	90.2	105	16.6	134	13.2	135	21.5	86	18.1	78	9.1	191	10.1	204	6.6	218	7.3	206
Montauk	29.6	47	33.5	44	6.5	58	5.4	60	7.9	23	8.6	15	7.3	179	8.0	186	5.1	207	5.9	188
Willets Point	113.5	116	115.6	116	18.6	141	17.3	148	23.0	91	23.2	91	9.8	192	11.0	209	6.4	229	7.8	210
Sandy Hook	69.3	7	68.5	17	13.7	35	11.5	44	15.7	350	16.5	357	10.5	175	9.8	181	5.4	171	7.5	180
Atlantic City	60.1	356	58.9	1	11.9	20	9.8	33	14.0	336	14.4	347	11.2	181	9.3	177	7.7	167	7.3	179
Cape May	72.2	28	68.0	27	12.7	56	10.8	55	15.8	9	15.6	7	10.9	199	9.6	185	8.3	185	7.3	186
Lewes	61.5	31	63.9	31	10.9	56	10.1	58	13.2	8	14.8	10	10.4	202	9.4	187	8.7	189	7.2	189
CBBT	39.4	21	39.1	27	7.4	47	6.6	49	8.9	2	10.0	9	5.9	186	10.4	188	4.7	206	7.7	189
Duck	49.1	359	47.4	6	9.3	23	7.6	28	11.5	338	11.6	345	9.2	175	9.2	177	6.1	190	7.1	180
Cape Hatteras	45.3	353	45.8	1	8.2	16	7.1	21	10.6	331	11.1	343	9.4	185	9.8	180	7.5	186	6.6	196
Springmaid	75.1	357	78.1	359	13.6	21	11.4	17	17.4	340	17.4	345	10.3	189	10.5	188	7.7	193	8.0	196
Charleston	75.8	17	79.8	14	13.1	39	10.9	36	16.7	359	16.5	6	10.4	202	10.5	199	7.8	205	7.6	208
Mayport	66.2	28	69.9	7	11.1	52	10.9	24	14.9	10	14.0	352	8.2	204	9.8	196	6.0	212	6.8	205
St. Augustine	66.2	14	66.1	7	11.2	36	10.2	23	16.3	355	13.1	352	10.1	197	9.6	196	7.3	202	6.6	205
Trident	51.7	7	53.7	6	8.1	28	8.5	19	11.9	348	11.1	351	10.1	202	8.9	197	7.7	205	5.9	206

5.1.2. Correlation Coefficients and RMS Errors

RMS errors and correlation coefficients between the tidal predictions and the simulated elevations are plotted in Figure 5.2. The RMS errors (correlation coefficients) with the open boundary conditions from Schwiderski's tidal model are generally smaller than 15 cm (greater than 0.9) at the coastal tide gauge locations. It shows that the Schwiderski's tidal model results are accurate in deep waters (which may be reasonable to be used as open boundary conditions for a regional ocean model). For the data assimilation experiments PA_ITC and PA_CTC, both the RMS errors and correlation coefficients of them are close. The maximum RMS error is 15.4 cm (at Mayport), and the minimum correlation coefficient of 0.96. And the RMS errors are less than 5 cm and the correlation coefficients are greater than 0.99 for the 9 coastal stations used in the data assimilation procedure. For most of the locations, the RMS errors (correlation coefficients) with the optimal boundary conditions are smaller (greater) than those with the open boundary conditions from Schwiderski's model results. However at Mayport and Gloucester, RMS errors (correlation coefficients) with the open boundary conditions from Schwiderski's model results are smaller (greater).

5.1.3. Time Series and Cotidal Charts

Comparison between the time series of the simulated elevations from PA_ITC and PA_CTC shows that the simulated elevations from PA_ITC and PA_CTC have similar patterns. Although there are some differences among the optimal amplitudes and phases for each tidal constituent along the open boundary of the two experiments, the combined optimal open boundary elevations for these two experiments are almost the same. The simulated elevations forced by the optimal open boundary conditions from these two experiments are therefore almost coincident. However, PA_CTC simulations are less computationally expensive than PA_ITC (computational time reduces 70%). Time series of tidal predictions and model results from the experiments with the open boundary conditions from PA_CTC and Schwiderski global tidal model are plotted in Figure 5.3. It shows that the model simulated elevations with open boundary conditions from Schwiderski tidal model are generally close to the tidal predictions (the RMS errors are less than 15 cm except Newport, Willets Point and Springmaid), but the phases of the model results are generally delayed. The model simulated elevations with the optimal open boundary conditions match the tidal predictions better than those with the open boundary conditions from Schwiderski tidal model, especially for phase match.

Coamplitudes and cophases of the five constituents are calculated by analyzing one-year simulated elevations from experiment PA_CTC using least squares method and presented in Figure 5.4a-e. For the semi-diurnal M_2, S_2, N_2, the amplitudes in deep waters increase from southwest to northeast. The amplitudes of M_2 are less than 1 m except inside of the Gulf of Maine where amplitudes exceed 2 m, and the amplitudes of S_2, N_2 are generally in the range of 8-20 cm except inside of the Gulf of Maine where exceed 20 cm. The phases of M_2, N_2 in deep waters are generally consistent from south to north, while phases of S_2 in deep waters increase from south to north. For the diurnal K_1, O_1, they have similar amplitude and phase patterns. Amplitudes are generally not more than 10 cm and phases decrease from south to north. The computed and the corresponding observed tidal harmonic constants (published by CO-OPS) at 18 tide gauge stations (listed in Table 5.3) show that, For M_2 constituent, the maximum amplitude error is 8 cm (at New London station), and the amplitude errors are less than 5 cm at open coast stations. The maximum phase error is 20 minutes happening (at Sandy Hook). For S_2, N_2, K_1, O_1 constituents, the observed and computed constants are close at most locations.

5.2. Optimal Estimation of Wind Drag Coefficients

The identical twin experiments in section 4.2.2 demonstrate that the wind drag coefficients can be exactly recovered by assimilating the pseudo-observations generated by model. In this section, the observed subtidal water levels at tide gauge stations along the U.S. East Coast are assimilated into the model. Experiments with one, eight and sixteen control variables were performed. And the results with data assimilation are compared with those without data assimilation (C_d calculated from Eq. 3.4, and the experiment is denoted as PA_NoDA). The subtidal water level forecasts with data assimilation are also evaluated using the results of an experimental nowcast/forecast system.

5.2.1. Data and Numerical Scheme

Hourly water level observations from 18 NOS tide gauge stations (shown in Figure 2.2) were filtered using a 30-hour low-pass Fourier filter to remove the astronomical tidal signals to obtain subtidal water levels. The EDAS surface wind fields from the National Centers for Environmental Prediction (NCEP) in the National Weather Service (NWS) were used as the surface forcing in the numerical model.

The forward model was first spun up from rest for 10 days, with the wind drag coefficients calculated from Eq.3.4 to create initial fields for the adjoint data assimilation system. The variational adjoint data assimilation was then continuously performed for 50 days (9/10 - 10/30/1996) with a 24-hour data assimilation window. The optimal values of C_d from each previous day was used as the initial guess for the following day's data assimilation. After obtaining the optimal C_d the forward model was reintegrated for 24 hours with the optimal C_d. A new initial field was created and saved at the end of each day as the initial condition for the following day's simulation.

5.2.2. Data Assimilation Results without the Penalty Terms

In this section, penalty terms in Eq.3.5 are not considered in order to optimize only the simulated subtidal water levels. The time series of the optimal wind drag coefficients from the three experiments are presented in Figures 5.5(a-c). For the experiment with one control variable (denoted as PA_NoPT1), the optimal values of C_d varies from -5.0 to 6.0. Negative values of C_d indicate that the wind stress direction is opposite that of the surface wind in order to minimize the cost function. For the experiment with eight control variables (PA_NoPT2), the temporal variations of the optimal C_d seems to be uncorrelated with each other. This may be caused by the definition of the eight control variables, but it is not unexpected since the changes in C_d are made to compensate for assumed errors in the wind fields. The absolute values of the optimal C_d are generally less than 20.0. However, the variance of each optimal C_d is greater than that of the one control variable experiment, and some values seem to be unreasonably large compared with the wind drag coefficients calculated using Eq.3.4. However, the magnitude of the cost function is reduced significantly with the optimal C_d from this experiment. This may indicate that the magnitude and/or direction of the surface wind stresses are not accurate enough so that the numerical model can not simulate the subtidal water level well compared with the observations. In order to minimize the cost function, the wind drag coefficients need to be adjusted in the wind stress computation. For the case with 16 control variables (PA_NoPT3), the optimal wind drag coefficient components C_{dx} and C_{dy} are not only different in magnitude but are also occasionally opposite in sign. From Eq. 3.3 we know that the wind stress direction will remain in the same direction as the surface wind only when C_{dx} is equal to C_{dy}. So the optimal C_{dx} and C_{dy} allow the wind stress direction calculated with the optimal C_{dx} and C_{dy} to deviate from that of the surface wind. If both C_{dx} and C_{dy} are positive, the wind stress direction is off from the wind direction less than 90°. And if C_{dx} and C_{dy} are both negative, the wind stress direction is totally opposite to the wind direction.

Time series of the cost function for these three experiments are presented in Figure 5.6. In general, the values of the cost function with data assimilation are less than those without data assimilation, and the values of the cost function from PA_NoPT3 are smallest. This demonstrates that, in the sense of minimizing the cost function, the best results are obtained from the experiment with 16 control variables. It also indicates that allowing the wind stress to change direction in the data assimilation procedure improves the accuracy of the model simulated subtidal water levels.

Time series of the subtidal water levels (shown in Figure 5.7) show that even if only one control variable for the entire model domain is used in the adjoint data assimilation process, the simulated subtidal water levels at 18 stations are closer to the observations than those without data assimilation (in which the wind drag coefficient is calculated using the Large-Pond formulation). The results from the 8 control variable experiment show that the simulated subtidal water levels are much closer to the observed subtidal water levels than the one control variable experiment. The simulated subtidal water levels from the 16 control variable experiment match the observations well for most stations both in amplitude and phase, even during strong wind periods.

The correlation coefficients and RMS errors for the experiment without data assimilation and for these three data assimilation experiments are plotted in Figure.5.8. The correlation coefficients of the experiment without data assimilation are the lowest and vary from 0.5 to 0.88. The correlation coefficients for the experiment with 16 control variables are the highest among these four experiments and vary from 0.93 to 0.98. The RMS errors without data assimilation are the largest except at the St. Augustine station (which is already small) and vary from 6 cm to 14 cm. The RMS errors with 16 control variables are the smallest and vary from 3.3 cm to 5.3 cm. From wind drag coefficient laboratory experiments, we know that the wind drag coefficient is related to the wind speed, and therefore wind drag coefficients vary in space and time. Since we have allowed the optimal values of C_d to represent changes in the original wind data to improve the simulated subtidal water levels along the coast, we can expect a variation in the calculated optimal values of C_d over space and time, and which will then be correcting for a variety of wind data problems (and possibly other problems as well). Since eight wind drag coefficients might represent the spatial variations of wind stress better than one control variable, the simulated subtidal water levels from PA_NoPT2 are closer to the observations than PA_NoPT1. In addition to optimizing the wind stress magnitude, the 16 control variables also allow to adjust the wind stress direction by any angle. Therefore the simulated subtidal water levels are further improved with respect to PA_NoPT2. The more control variables that are used in the data assimilation procedure, the better the results should be. However, it must also be noticed that more control variables require more observations to be assimilated into the model in order to obtain better optimal control variables, which, in turn, make the simulated results match observations better. Only if there are adequate representative observations can more control variables be used in the data assimilation process. The relationship between the minimum number of observations and the number of control variables depends on the spatial and temporal distribution of the observations (Zhang, 2000) and could be examined with identical twin experiments.

The results from the above experiments show that the values of the cost function with data assimilation decreased as expected. However, some optimal values of C_d appeared to be too large and/or negative, perhaps indicating a physically unrealistic solution. Such abnormal values of C_d may be due to the following reasons: (1) Errors in the EDAS wind fields (wind speed and wind direction, whatever the causes) may have to be corrected by changing the optimal wind drag coefficients (a negative value of C_d would be obtained if the wind direction was wrong). (2) Our basic assumption is that all errors in the simulated subtidal water levels are produced by errors in the surface wind field, and the errors in surface wind field are corrected and represented by changes in wind drag coefficients. This assumption infers that the other conditions and parameters (initial conditions, open boundary conditions, surface air-pressure field, nonlinear effects, friction, etc.) are perfect and that all errors produced by these factors can be projected onto the surface wind drag coefficients (control variables). This could result in an abnormal value of C_d value if the assumption was invalid. (3) C_d is assumed to be constant either throughout the domain (one control variable) or in each subregion (8 and 16 control variables) because of limitations of the available observations. However, the true spatial variations of C_d may not be properly represented in the model. (4) The penalty terms are not considered. The minimization of the cost function alone does not ensure that the adjoint data assimilation technique obtains reasonable values of optimal control variables in the physical sense. The constraint conditions and penalty terms may be necessary to obtain more reasonable values of these control variables.

5.2.3. Effects of Penalty Term and Smoothness of Control Variable

The purpose of adding the penalty terms to the cost function is to smooth and stabilize the estimates of the control variables. The estimates of the control variables from the cost function without the penalty terms are indeed solutions satisfying the desired objective of minimizing the misfits between the model results and observations, but they are rapidly varying in space and time. Thus, they are probably not desired solutions in physical and realistic respects. Our goal is to seek a balance between misfit minimization and solution smoothness. The first objective should dominate the latter, and the role of smoothing terms must be kept to a minimum so that the realistic structural features of the estimated control variables can be preserved to the greatest extent. The influences of these two objectives are regulated through the weighting coefficients. Therefore, two penalty terms in the cost function Eq. 3.5 with weighting coefficients γ_1 and γ_2 were considered. Three additional experiments using 16 control variables were performed with different weighting coefficients (see Table 5.4).

Time series of the optimal values of C_d in the x-direction (similar results for the y-direction) from these experiments are shown in Figure 5.9. The time series of the optimal C_d from the experiments with penalty terms are very similar. And they are much smoother than that of without penalty terms. With the penalty terms, the spatial and temporal variations of the optimal C_d are smoothed, and extremely large values in the optimal C_d are eliminated. Thus, adding the penalty terms to Eq. 3.5 appears to lead to a more physically realistic depiction of the optimal wind stress fields. Figure 5.10 shows that with the penalty terms, correlation coefficients decrease and *RMS* errors increase at the tide stations. Differences of correlation coefficients and *RMS* errors between with and without penalty terms are less than 0.1 and 2 cm, respectively. This indicates that the realistic structural features of the subtidal water levels are preserved, while the estimated optimal values of C_d are smoothed. According to the experiment results, the most acceptable results would be obtained by setting the weighting coefficients $\gamma_1 = \gamma_2 = 0.001$ in Eq. 3.5. The number of iterations for each 24-hour data assimilation is reduced 50% with the addition of the penalty terms, thus reducing the computational time. The effects of the penalty terms on water level forecasts are discussed in the following section.

Table 5.4. Weighting Coefficients of γ_1 and γ_2 (see Eq. 3.5)

Case name	γ_1	γ_2
PA_NoPT3	0.0	0.0
PA_PT1	0.001	0.001
PA_PT2	0.0025	0.0025
PA_PT3	0.005	0.005

5.2.4. Subtidal Water Level Forecasts

One important purpose of the water level data assimilation is to improve subtidal water level forecasts along the coast by providing better initial conditions for the forecasting model. Therefore, a 24-hour nowcast/forecast system was configured, as shown in Figure 5.11. In this system, the forward model is run for 10 days to create restart files for the first nowcast/forecast run. The nowcast model is run for 24 hours (forced by the EDAS analyzed wind fields) to create an initial field for the forecast model. The forecast model is then run for the next 24 hours forced by ETA forecasted wind fields from NCEP/NWS from the initial fields created by the nowcast model. The forecast model utilizes the same grid, bathymetry, and open boundary conditions as the nowcast model. The following nowcast/forecast experiments were continuously performed for the period of 9/11/96 to 12/31/96 (110 days), and the forecast water levels are used in statistical analysis:

SWL_F1:
No data assimilation is included in the nowcast mode, and the wind drag coefficients for both the nowcast and forecast modes are calculated by using Eq.3.4 (denoted as the baseline run or without data assimilation case);

SWL_F2:
24-hour water level data assimilation with 16 control variables and without penalty terms is performed in the nowcast mode to obtain optimal values of C_d. The wind drag coefficients are calculated using Eq.3.4 in the forecast mode;

SWL_F3:
The same data assimilation procedure as SWL_F2 is performed in the nowcast mode, but the optimal values of C_d from the previous day's nowcast are applied to the forecast of the next day.

SWL_F4:
A 24-hour water level data assimilation with 16 control variables and penalty terms (γ_1=γ_2=0.001) is performed in the nowcast mode, and the wind drag coefficients are calculated using Eq.3.4 in the forecast mode;

SWL_F5:
The same data assimilation procedure as SWL_F4 is performed in the nowcast mode, but the optimal values of C_d from the previous day's nowcast are applied to the next day's forecast.

We are concerned with how much improvement of the water level forecasts is made by using the data assimilation technique in the nowcast/forecast system and how long the improvement could last. Water level forecasts for each hour of a 24-hour forecast circle over the 110-day period are subsampled (110 data points in total for each hour) and compared with the corresponding observations. The variations of the average correlation coefficients and RMS errors over the 18 stations with forecasting time for these experiments are presented in Figure 5.12. For the experiment without data assimilation (SWL_F1), the average RMS errors of the subtidal water level forecasts over 18 stations vary with forecasting time in the range from 9.8 cm to 13 cm. The average correlation coefficients vary from 0.75 to 0.8. Both average RMS errors and correlation coefficients do not change much as forecasting time increases. For SWL_F2, the RMS errors in the first two hours is about 3 cm smaller than that of SWL_F1 (without data assimilation). The RMS errors decrease about 0.5 cm from hour 3 to hour11. When the forecasting time is greater than 11 hours, differences of the RMS errors between SWL_F1 and SWL_F2 are insignificant. Applying the optimal values of the previous day's C_d to the next 24-hour forecasts (SWL_F3), the RMS errors are a little smaller than that of SWL_F2 in the first 4 hours. However, the RMS errors increase very fast and they are even much bigger than that of SWL_F1 as the forecasting time is greater than 6 hours. These results indicate that, on the average RMS errors over these 18 tide stations, the improvement of subtidal water level forecasts by applying the subtidal water level data assimilation without penalty terms is mostly limited in the first 3 hours. After 3 hours, the improvement on water level forecasts is not significant, and the subtidal water level forecasts by extending the optimal values of C_d of the previous day's nowcasts to the next 24-hour forecasts become even worse than that without data assimilation. By introducing penalty terms into the cost function formulation (SWL_F4 and SWL_F5), the RMS errors become smaller than that of SWL_F2, and they are about 3 cm smaller than that of SWL_F1 in the first 5 hours. For SWl_F5, the RMS errors become larger than that of SWL_F1 after about 8 hours. The results of SWL_F3 and SWL_F5 indicate that the optimal values of C_d from the previous day's nowcasts cannot be simply applied to the next day's forecasts since the surface wind fields change with time, especially in the transition period of a storm event.

The average improvement by the data assimilation technique over the18 stations for each forecasting time is calculated as

$$P = \frac{\overline{RMS}_{noDA} - \overline{RMS}_{DA}}{\overline{RMS}_{noDA}} \times 100\% \tag{5.2}$$

where P is average improvement, $\overline{RMS}_{noDA}$ *and* $\overline{RMS}_{DA}$ are average RMS errors from the experiments without and with data assimilation, respectively. Figure 5.13 shows that the improvement of SWL_F2 decreases faster than SWL_F4. More than 10 % improvement takes place in the first 3 hours for SWL_F2 and in the first 9 hours for SWL_F4. The improvement of SWL_F4 is greater than SWL_F2. Therefore, including the penalty terms in the cost function to smooth the optimal wind drag coefficients leads to the most improved forecast results.

RMS errors of the subtidal water level forecasts from SWL_F4 as a function of both forecasting time and water level station are presented in Figure 5.14. North of CBBT (stations 1-13), the RMS errors in 24-hour forecasts are less than 12 cm and are generally less than 10 cm during the first 6 hours. The maximum RMS errors of 20 cm occurred at Charleston, South Carolina. However, the nowcast RMS errors at Charleston (Figure 5.10) are not significantly larger than those of the other stations. In examining the ETA forecasted and EDAS analyzed surface wind fields (Figure 5.15), we found that the two wind fields are very different near Charleston during Julian days 320-322, 328-329, and 360-362. In those days, the forecasted winds produced large subtidal water level forecasts at Charleston, Springmaid and Fort Pulaski, which could explain the large RMS errors in that region.

The nowcast/forecast experiments demonstrate that the average RMS errors of forecasted water levels over 18 water level stations within a 24-hour forecast cycle without data assimilation vary from 9.8 cm to 13 cm, and the average correlation coefficients range from 0.75 to 0.8. The improvement in the water level forecasts with data assimilation primarily takes place within the first 6 hours. There is no significant improvement after 6 hours (the differences are less than 1 cm). This implies that the impact of the initial conditions generated by the model nowcast on the next day's forecasts is limited within about 6 hours. Therefore, further experiments should be performed on how to extend the optimal values of C_d from the previous day's data assimilation to the next day's water level forecasts.

5.3. Total Water Level Nowcasts/Forecasts

As was described earlier, total water level variation includes both astronomical tides and nontidal water level variation. In fact, the most concerned by mariners is always the total water levels which have direct impacts on the life of human being and can be directly measured at water level stations. Since it is difficult to exactly separate nontidal water levels from astronomical tides, our ultimate purpose is to produce total water level forecasts. If harmonic constants are available at a station, the astronomical tides at any time can be accurately predicted with either harmonical or response techniques. If harmonic constants are not available, the astronomical tides can be obtained with a numerical model forced with tides along the open boundaries. However, tidal simulations are generally not as accurate as tidal prediction since there are many undetermined factors for a numerical model system and errors of the boundary forcing and bathymetry. Subtidal water level forecasts can be obtained with numerical simulations forced by forecasted surface winds and atmospheric pressures. Here, several experiments were performed to compute total water level forecasts:

TWL_F1:
The nowcast and forecast runs are forced with the optimal harmonic constants of M_2, S_2 N_2, K_1, and O_1 obtained from experiment PA_CTC1 in section 5.1 along the open boundary. The nowcast run is forced with EDAS surface winds and the forecast run is forced with ETA forecasted winds. The wind drag coefficients for both nowcast and forecast runs are calculated with Eq.3.4.

TWL_F2:
The same tidal open boundary conditions as TWL_F1 are used to force both the nowcast and forecast runs. The nowcast run is forced by EDAS surface winds with the optimal wind drag coefficients obtained through the observed water level data assimilation. The forecast run is forced by ETA forecasted winds with wind drag coefficients calculated using Eq.3.4.

TWL_F3:
At coastal stations, astronomical tides are calculated using harmonic tidal prediction of 37 tidal constituents. The same nowcast/forecast scheme as SWL_F4 in Section 5.2.4 is implemented to obtain subtidal water level forecasts. Total water level forecasts are then derived by simply superimposing the simulated subtidal water level forecasts on the tidal predictions.

The average RMS errors and correlation coefficients over 18 tide stations are presented in Figure 5.16 as a function of the forecast hour. The RMS errors of the 24-hour forecasts of TWL_F1 vary from 24-27cm. The RMS errors of TWL_F2 vary from 12-22cm, which are 10 cm less in the first 6 hours and 5 cm less after 6 hours than those of TWL_F1. The RMS errors of TWL_FF3 vary from 10-16cm, which are about 2 cm less in the first 5 hours and about 5 cm less than after the first 5 hours than TWL_F2. Figure 5.15 also shows that the RMS errors for the subtidal water level forecasts of TWL_F3 are greater than those of the total water level forecasts. Therefore, adding the tide prediction and subtidal water level forecasts together reduces the RMS errors of the total water level forecasts. However, the mean values of the water level observations are greater than model forecasts. After removing the mean, the RMS errors of TWL_F1 are reduced to about 15 cm, and those of TWL_F2 are smaller than TWL_F1 during the first 9 hours. There is no significant difference between the water level forecasts of TWL_F1 and TWL_F2 after that. Therefore, the differences in the mean values between the observations and the model forecasts have very important contributions to the RMS errors of the water level forecasts (datum errors). The wind drag coefficient adjustment brings the mean values of the forecasts closer to those of the observation. The correlation coefficients of these three experiments are all greater than 0.94, and the phase of the forecasted water levels closely matches the observations. The contours of the RMS errors from these three experiments are shown in Figure 5.17 as a function of the forecasting time and the location. Similar contour patterns appear in the RMS errors before and after the mean were removed. Larger RMS errors occurred near Willets Point, Lewes and Charleston. South of Sandy Hook, the RMS errors of TWL_F1 are about 10 cm, which are greater than those of TWL_F2 and TWL_F3. Before the means were removed, the best results were obtained from TWL_F3 with RMS errors being less than 20 cm for 24-hour forecasts. After the means were removed, the RMS errors of TWL_F3 near the Long Island Sound (between Montauk and Sandy Hook) were larger than the other stations. The RMS errors increase rapidly during the first 6 hours. Interestingly, RMS errors south of Sandy Hook for TWL_F3 vary slowly in time and space.

For total water level forecasts, the best results were obtained by adding tide predictions to the simulated subtidal water levels obtained by data assimilation with penalty terms (TWL_F3). The average RMS errors over 18 stations of the 24-hour water level forecasts are less than 16cm, and the average correlation coefficients are greater than 0.96. The accuracy of the forecasted total water levels (TWL_F2) is worse than simply adding the tide predictions to the simulated subtidal water levels. This result might not be expected, since the interaction between the astronomical tides and the surface winds is included in the model dynamics for TWL_F2. The reason might be explained as follows: (1)Tidal numerical model will not be able to reproduce exactly the tide predictions, which are inherently more accurate, because of errors in the tunable model parameters, open boundary forcing, bathymetry, and geometry. (2) Since we assume that the differences between the observed and the simulated water levels are caused by the errors in wind stress fields (corrected by adjusting wind drag coefficients), the errors in the simulated astronomical tides will be attributed to the errors of the wind stress fields. Such errors cannot be properly corrected by adjusting the wind drag coefficients and may result in physically unrealistic wind drag coefficients. (3) since the astronomical tide signal is much stronger than the subtidal water level signal, the latter plays a less significant role in the assimilation of total water levels. This may result in unreasonable corrected wind stress fields. Although Case3 is the best choice for total water level forecasts at coastal stations, its shortcoming is that tidal predictions are only available at observation locations. For other locations, TWL_F2 is the next best option for computing total water level forecasts. Finer grid resolution, more accurate bathymetry, coastline data and improved tidal open boundary conditions can all help to improve the performance of the tidal simulations.

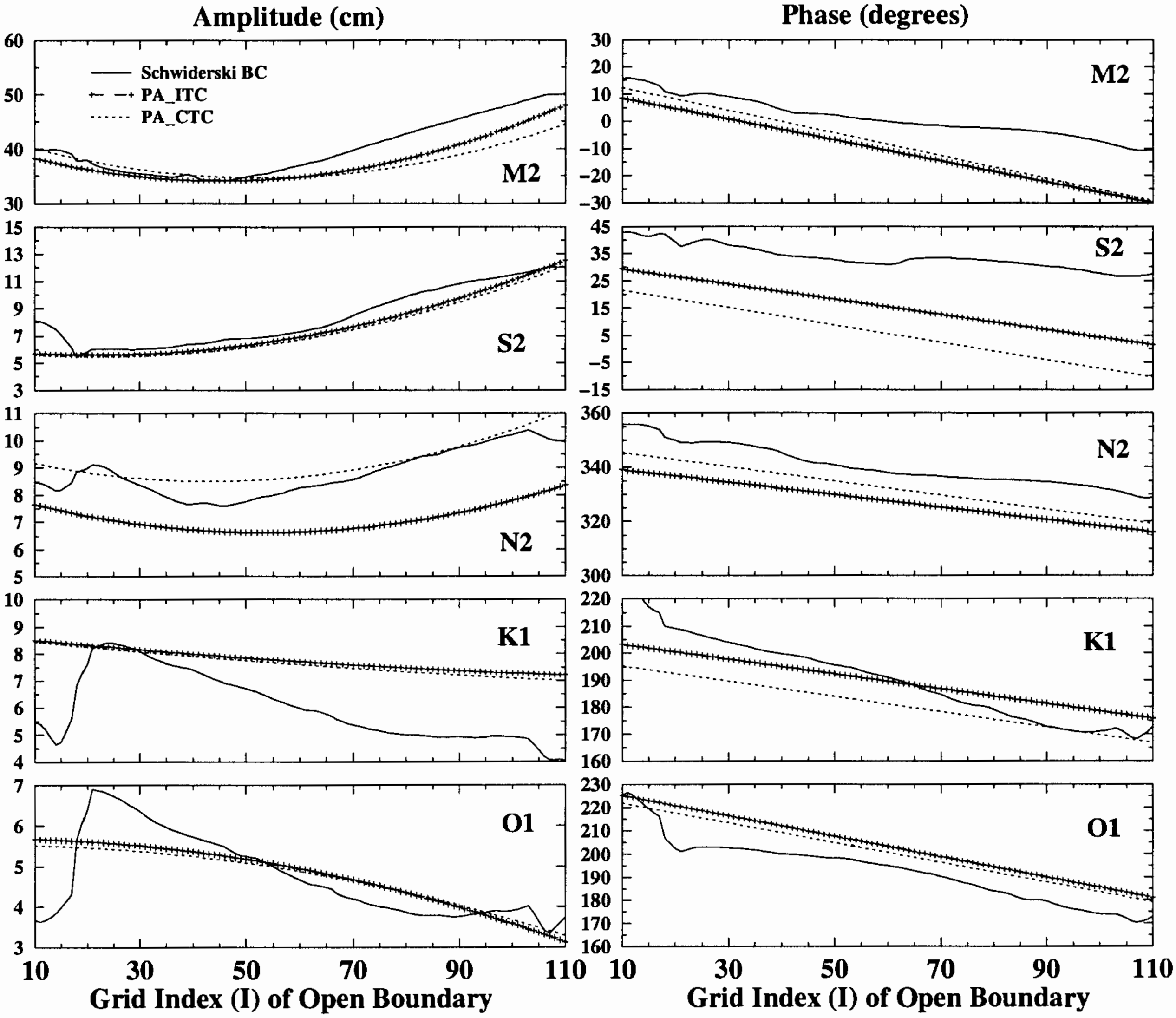

Figure 5.1. Amplitudes and phases from Schwiderski global tide model and the optimal data assimilation experiments. Solid line, from Schwiderski global model; dashed line with plus, from PA_ITC; dotted line, from PA_CTC.

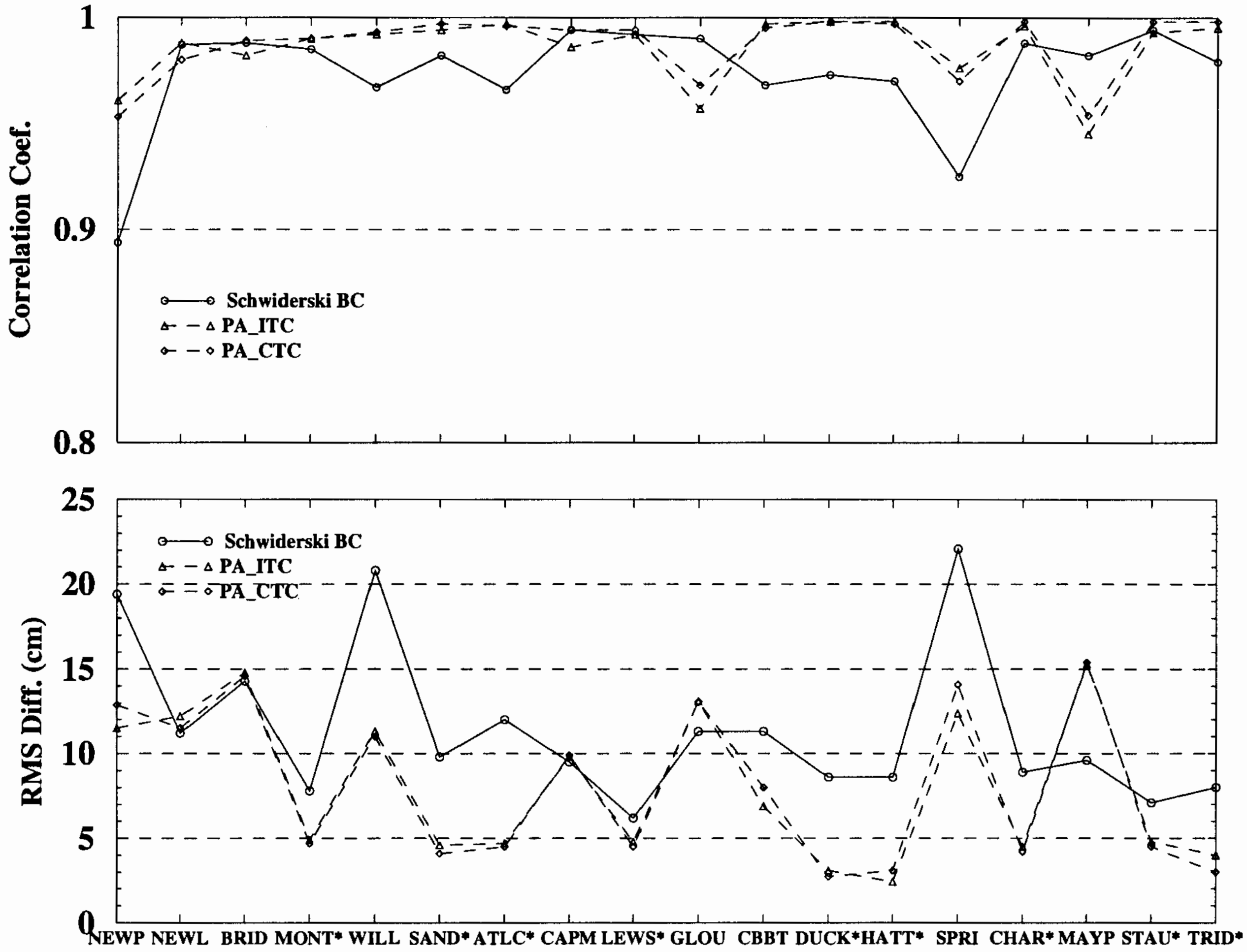

Figure 5.2. RMS errors and correlation coefficients between the tidal predictions and model results with open boundary conditions from Schwiderski global tide model and the optimal data assimilation experiments. Solid line with circle, Schwiderski global model; dashed line with triangle up, from PA_ITC; dashed line with diamond, from PA_CTC. The asterisk beside the station name indicates that the data from that station were used in assimilation.

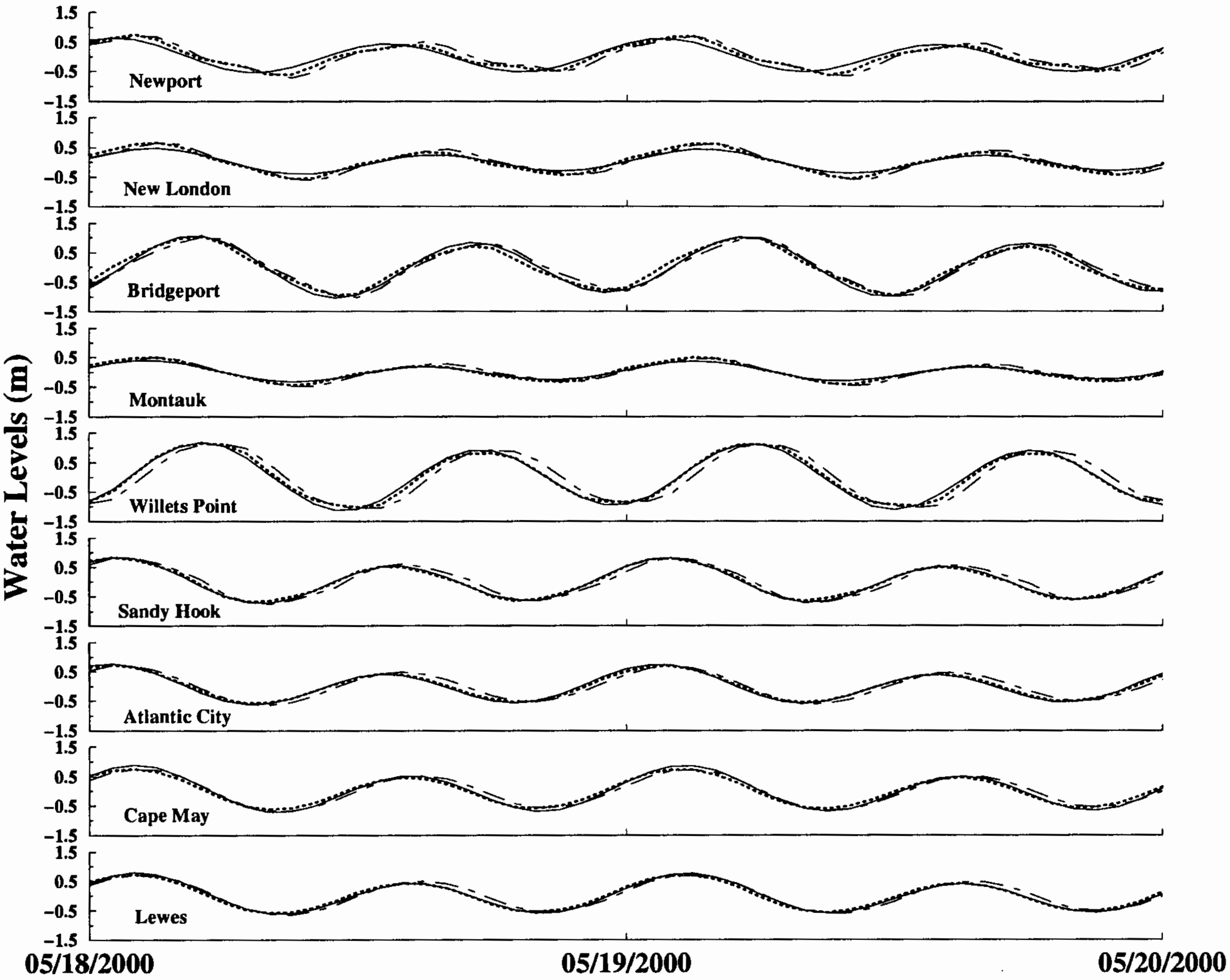

Figure 5.3. Tidal predictions (solid line) compared to model results with open boundary conditions from Schwiderski tide model (dot-dashed line) and the data assimilation experiment PA_CTC (dotted thick line).

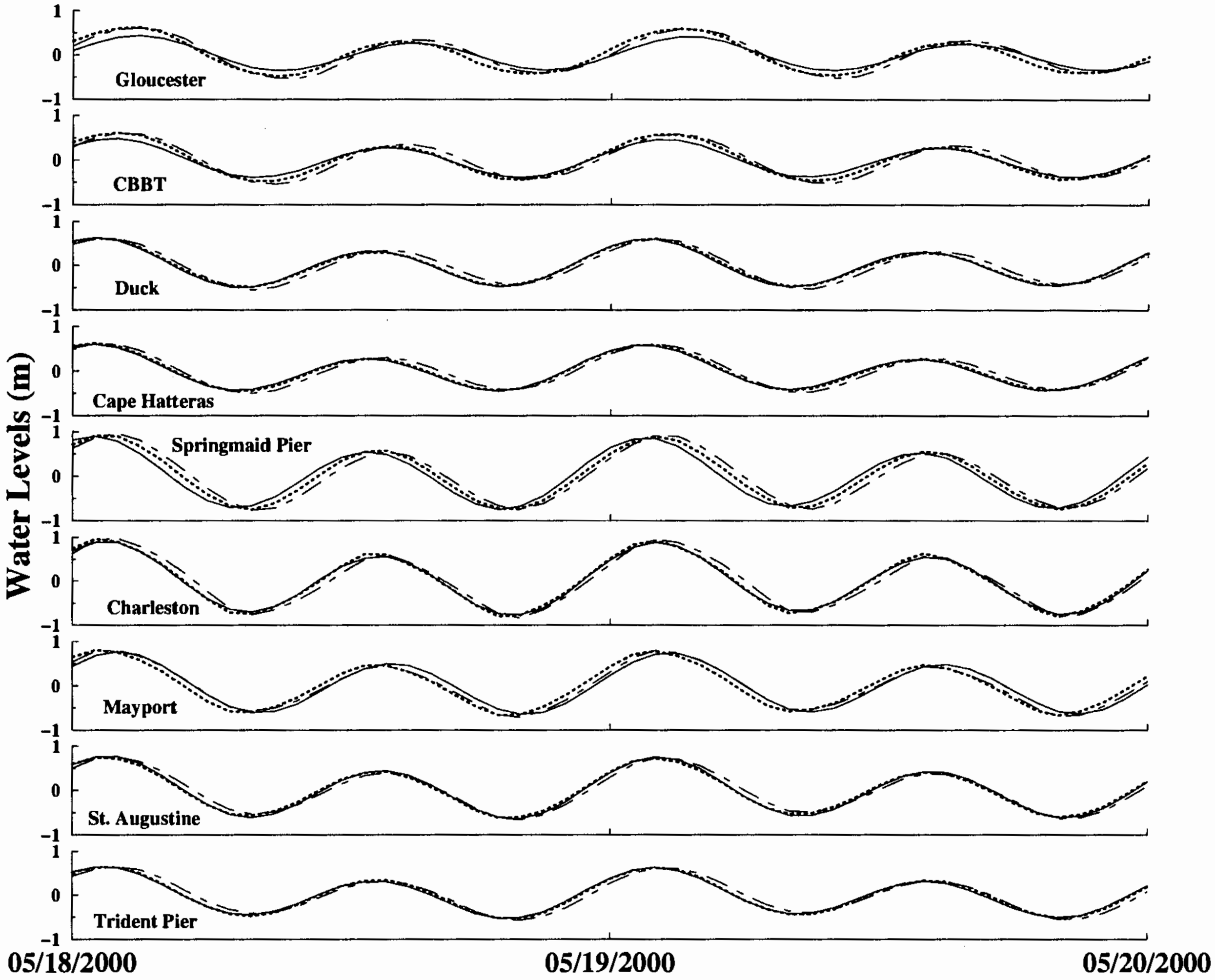

Figure 5.3. (Continued).

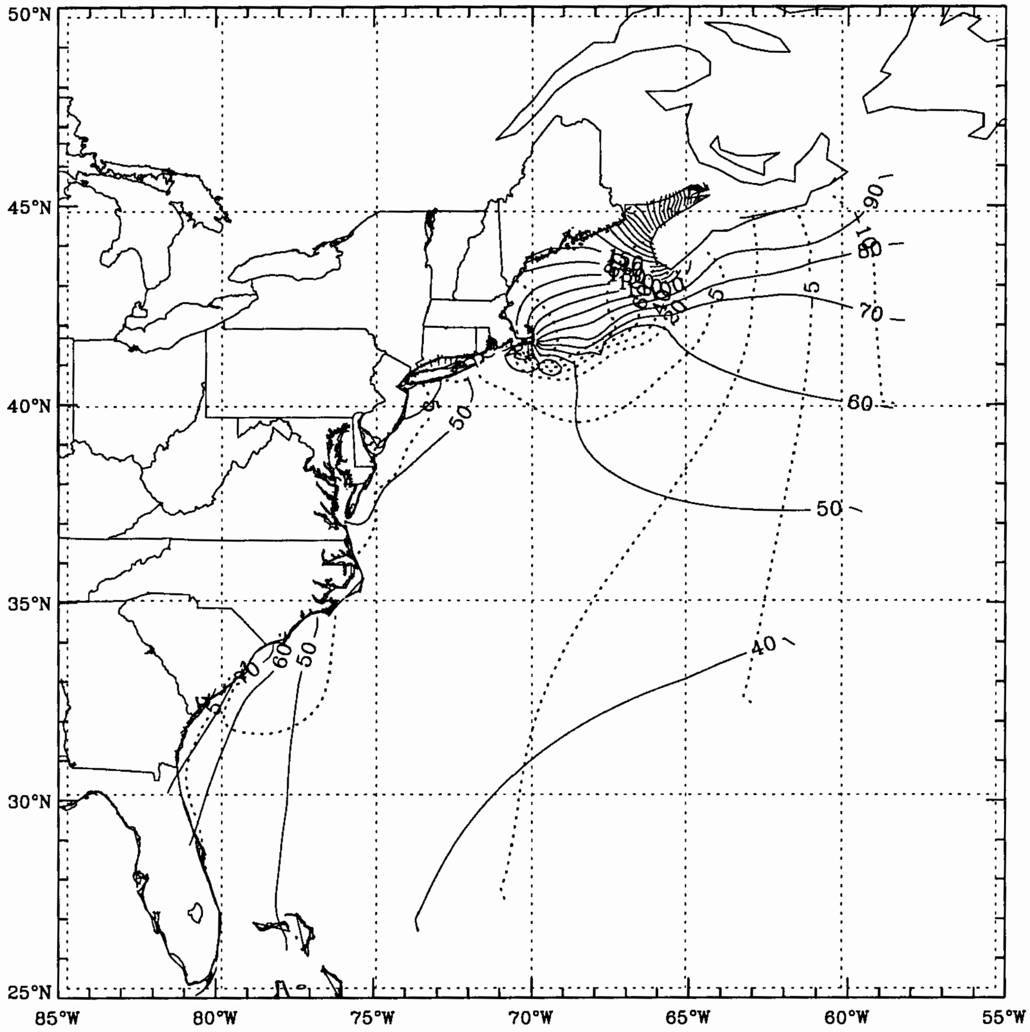

Figure 5.4a. Cotidal charts of M_2 constituent from model results of PA_CTC. Solid line, coamplitudes (in centimeters); dotted line, cophases (in degrees).

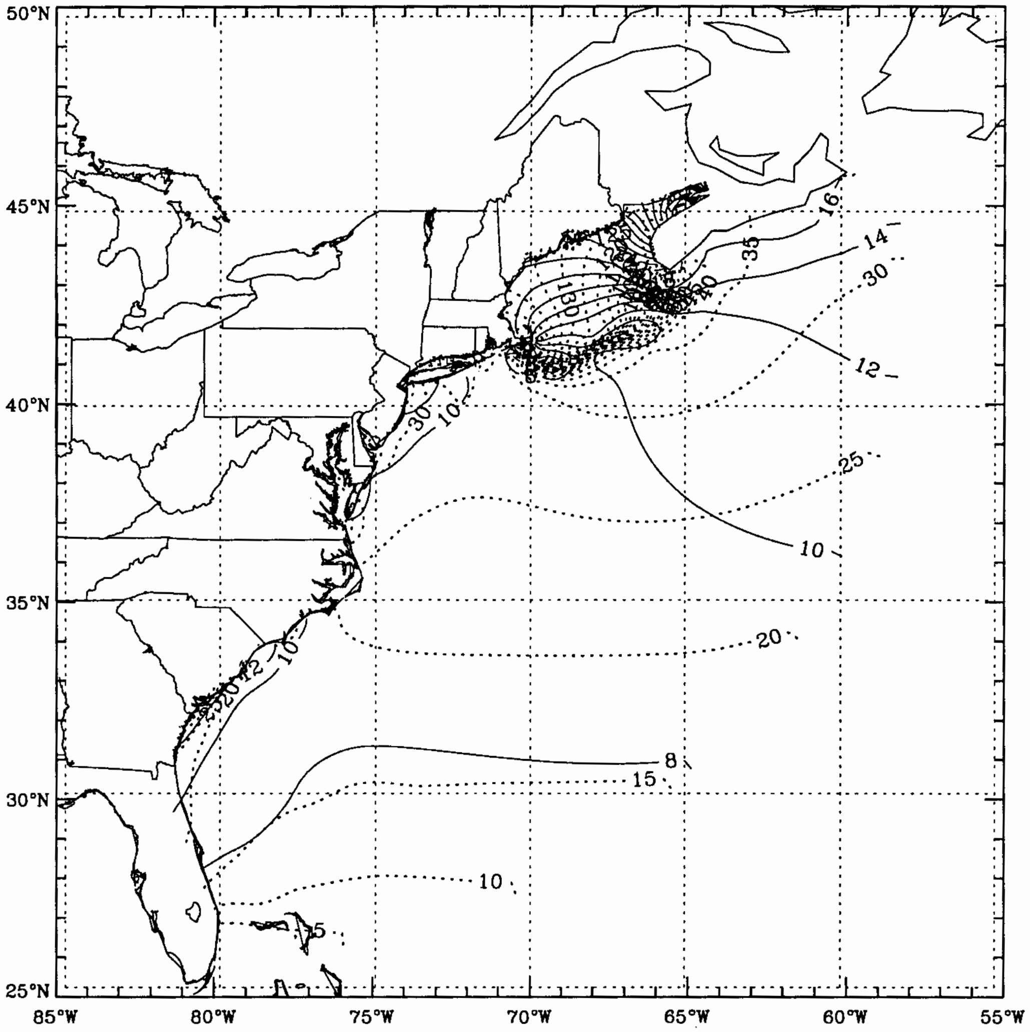

Figure 5.4b. Cotidal charts of S_2 constituent from model results of PA_CTC. Solid line, coamplitudes (in centimeters); dotted line, cophases (in degrees).

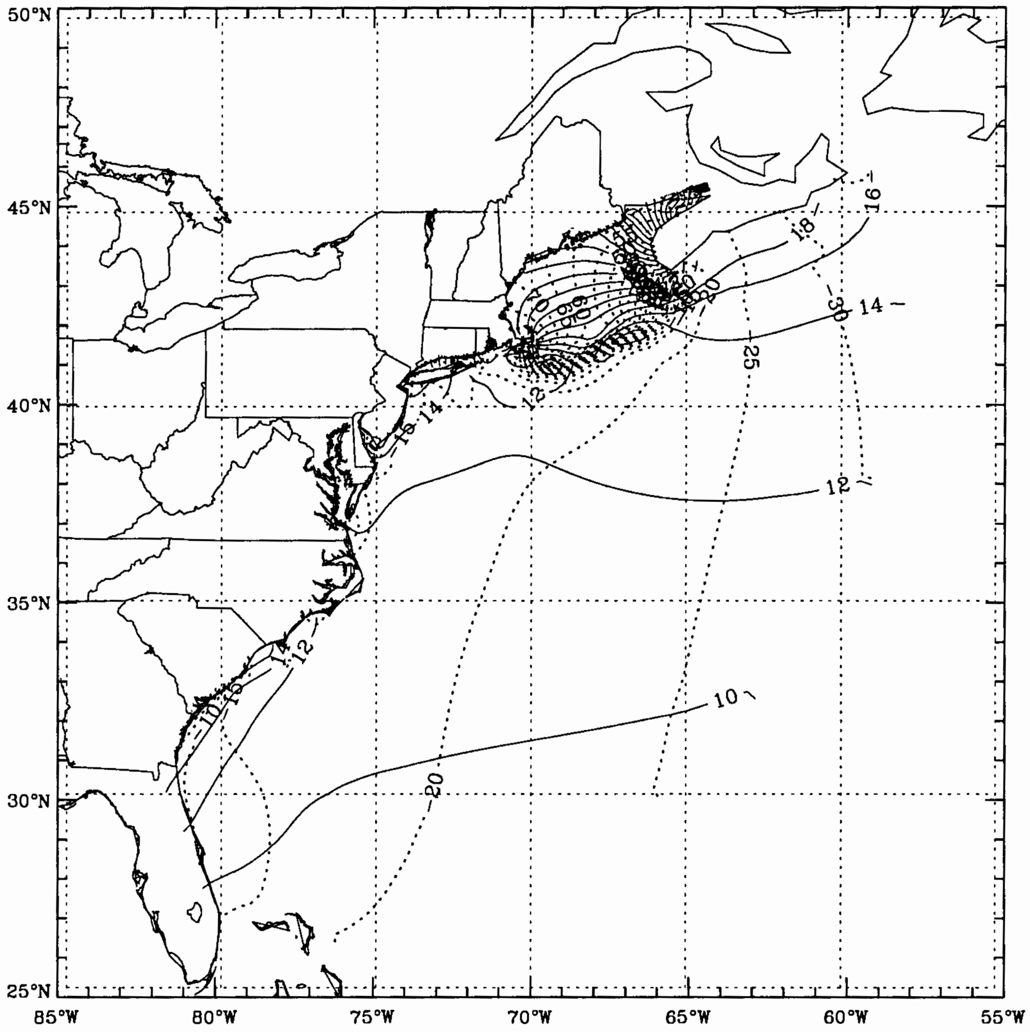

Figure 5.4c. Cotidal charts of N_2 constituent from model results of PA_CTC. Solid line, coamplitudes (in centimeters); dotted line, cophases (in degrees).

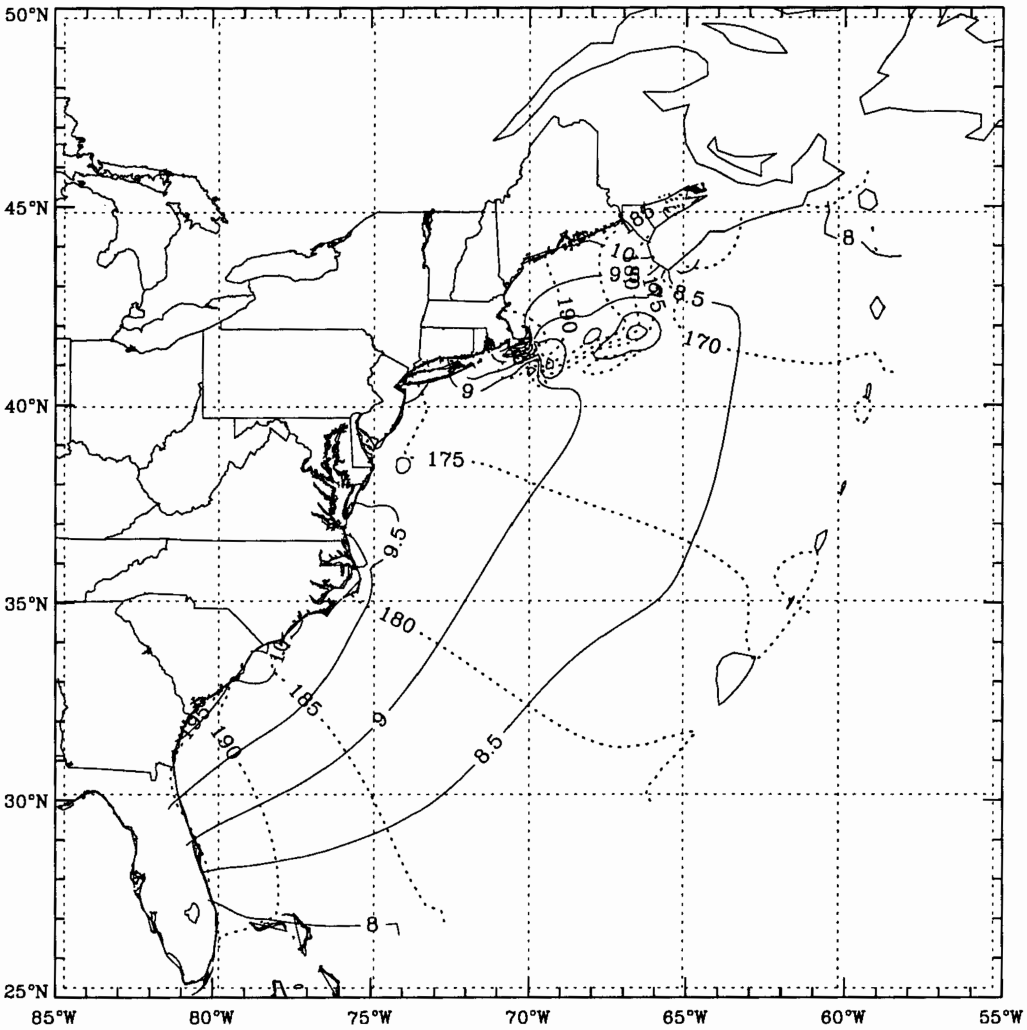

Figure 5.4d. Cotidal charts of K_1 constituent from model results of PA_CTC. Solid line, coamplitudes (in centimeters); dotted line, cophases (in degrees).

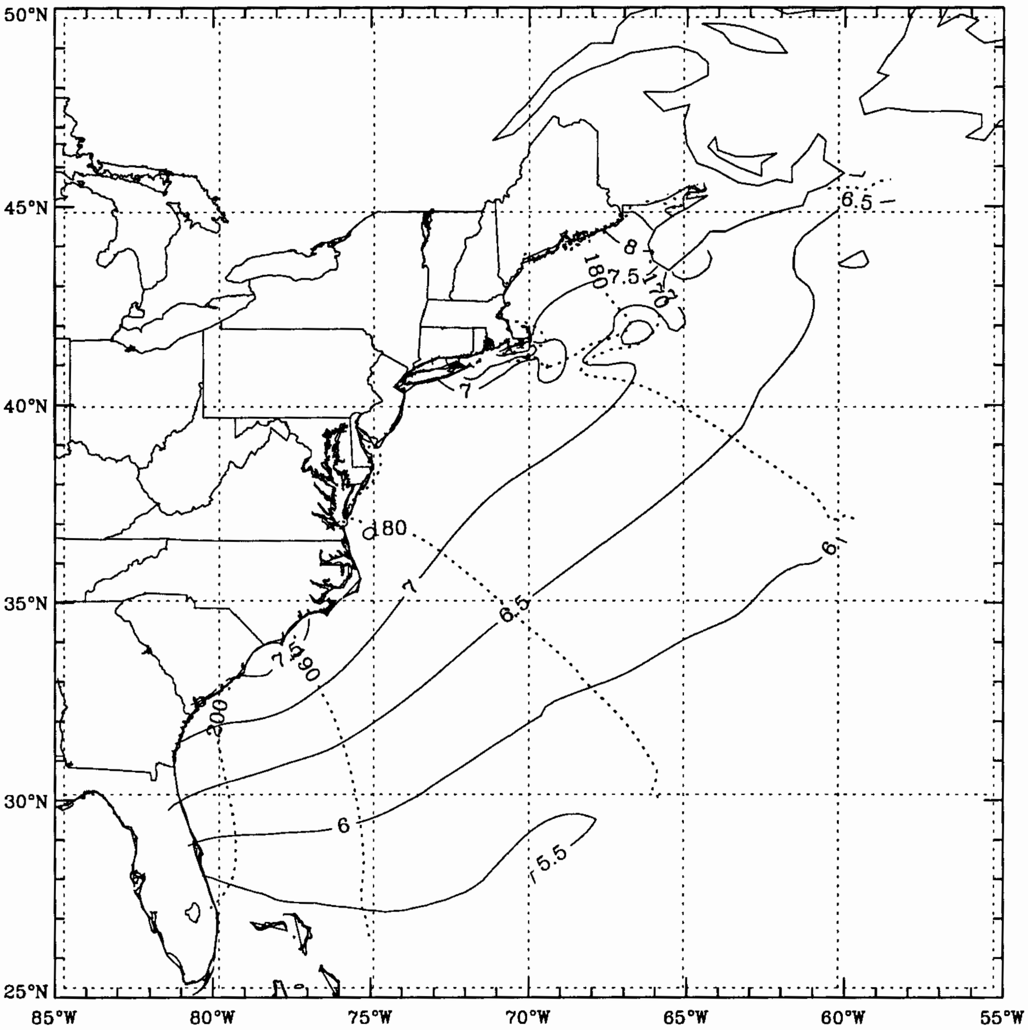

Figure 5.4e. Cotidal charts of O_1 constituent from model results of PA_CTC. Solid line, coamplitudes (in centimeters); dotted line, cophases (in degrees).

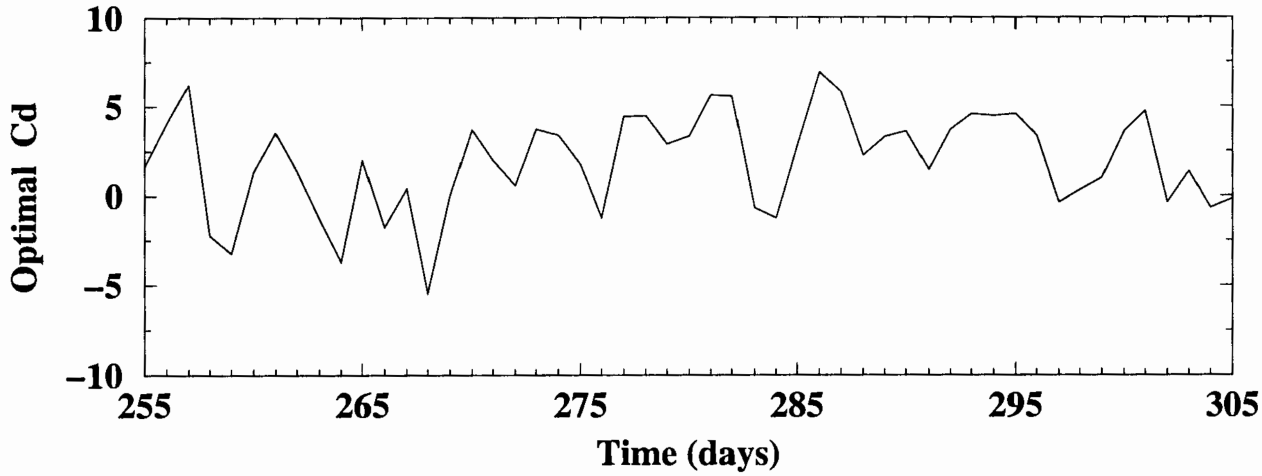

Figure 5.5a. Time series of optimal values of C_d for the one control variable experiment (PA_NoPT1).

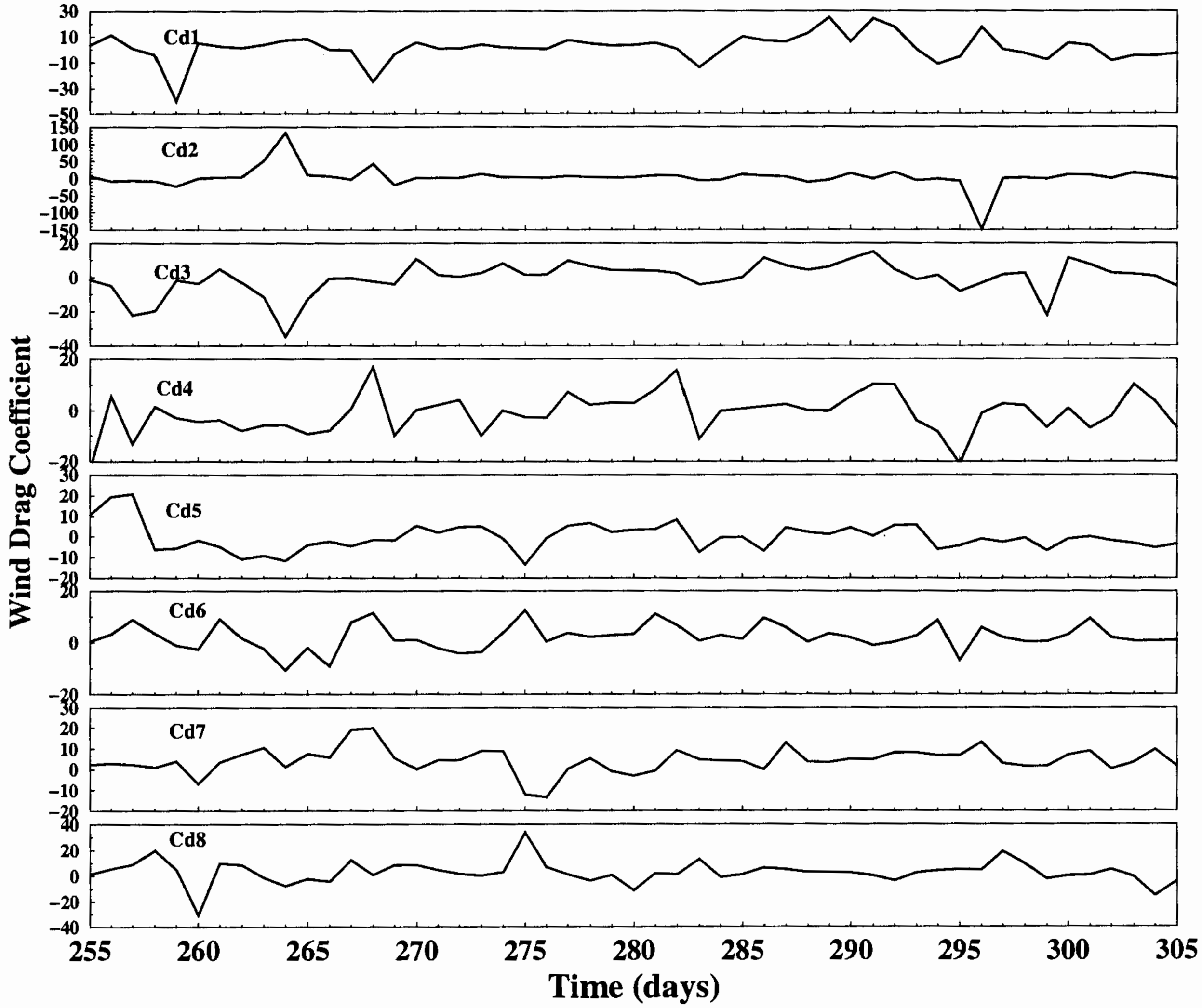

Figure 5.5b. As Figure 5.5a, but for the eight control variables experiment (PA_NoPT2).

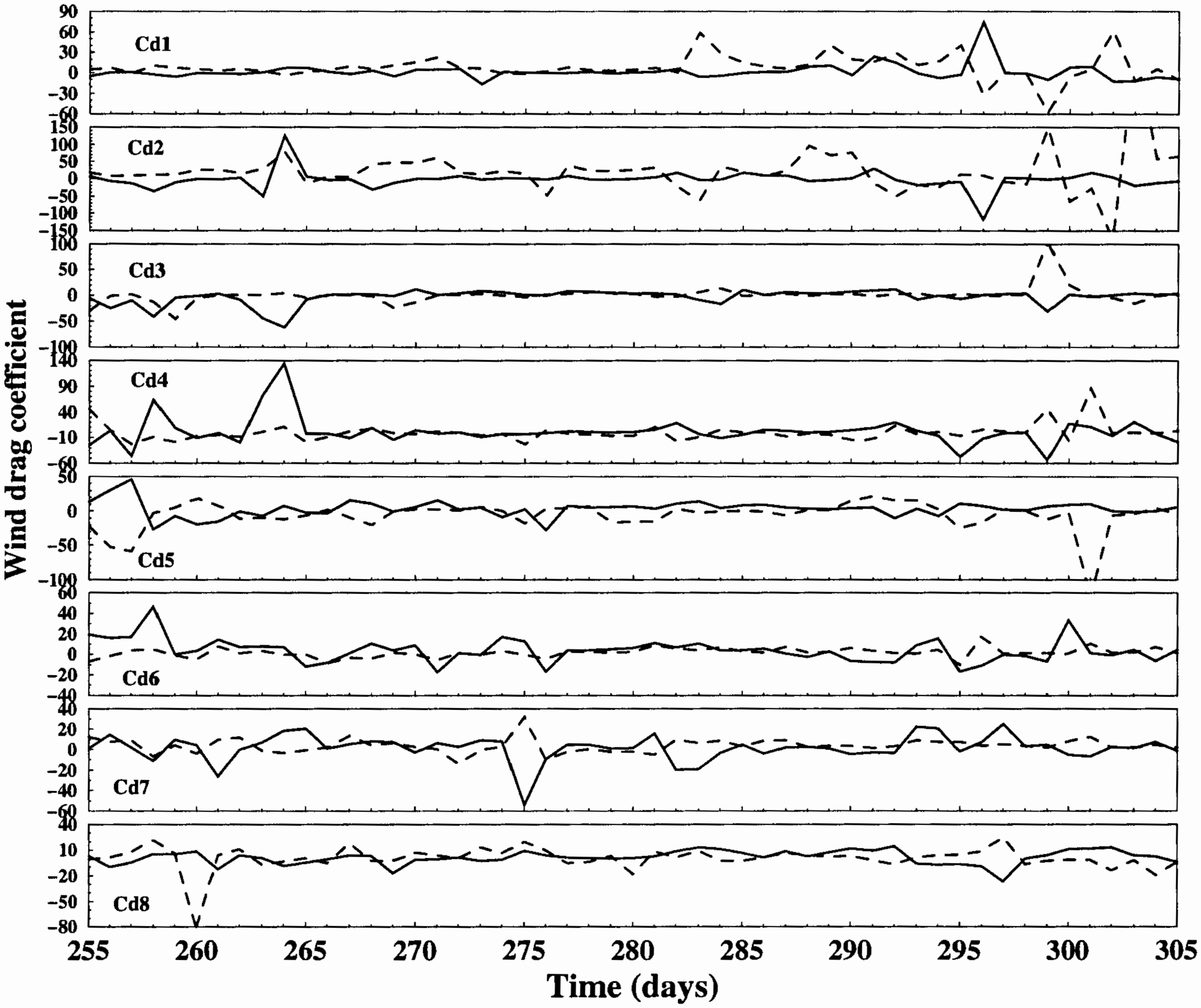

Figure 5.5c. As Figure 5.5a, but for the 16 control variables experiment (PA_NoPT3). The solid line, C_{dx}; dashed line, C_{dy}.

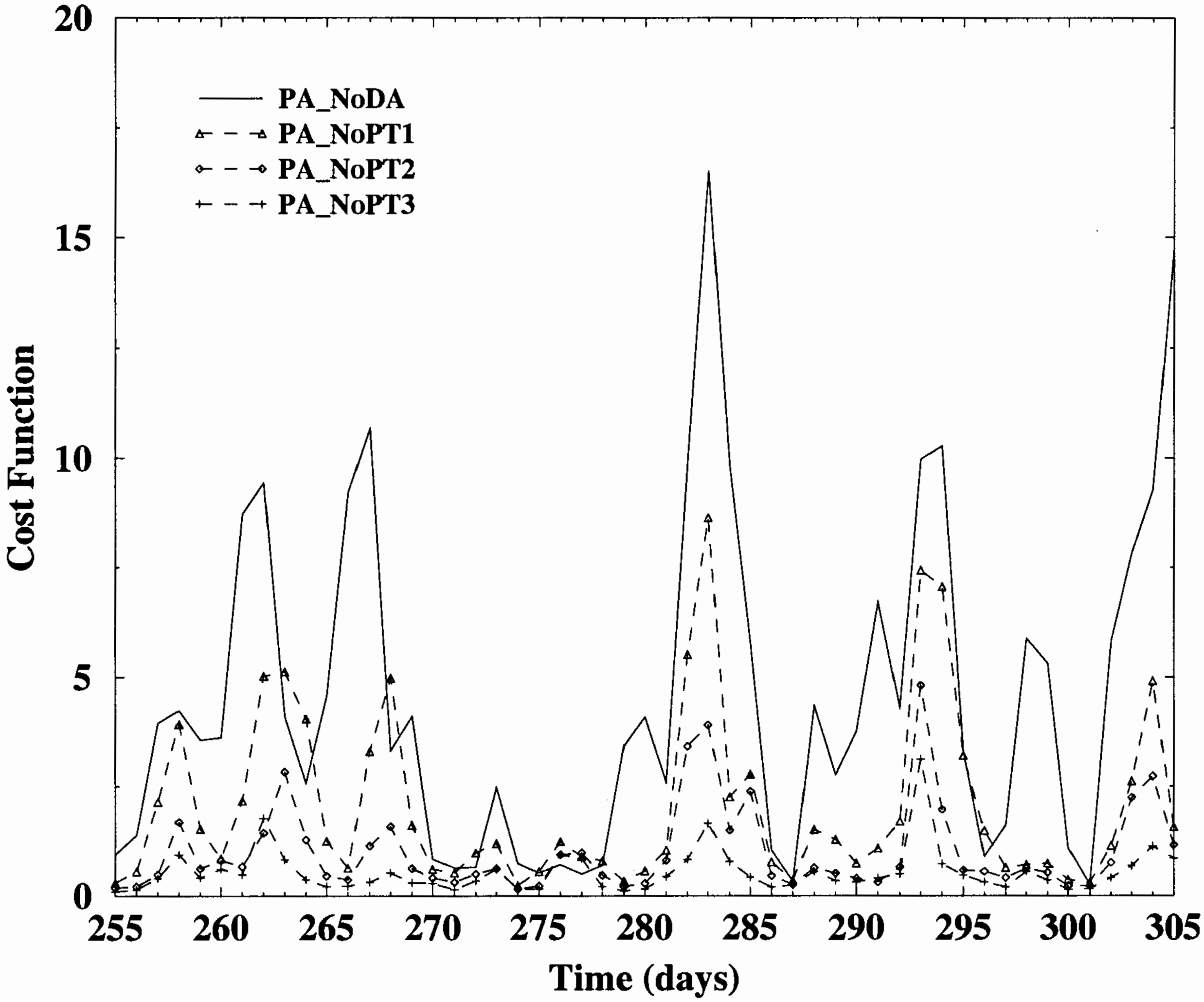

Figure 5.6. Time series of the cost function for the experiments with and without data assimilation.

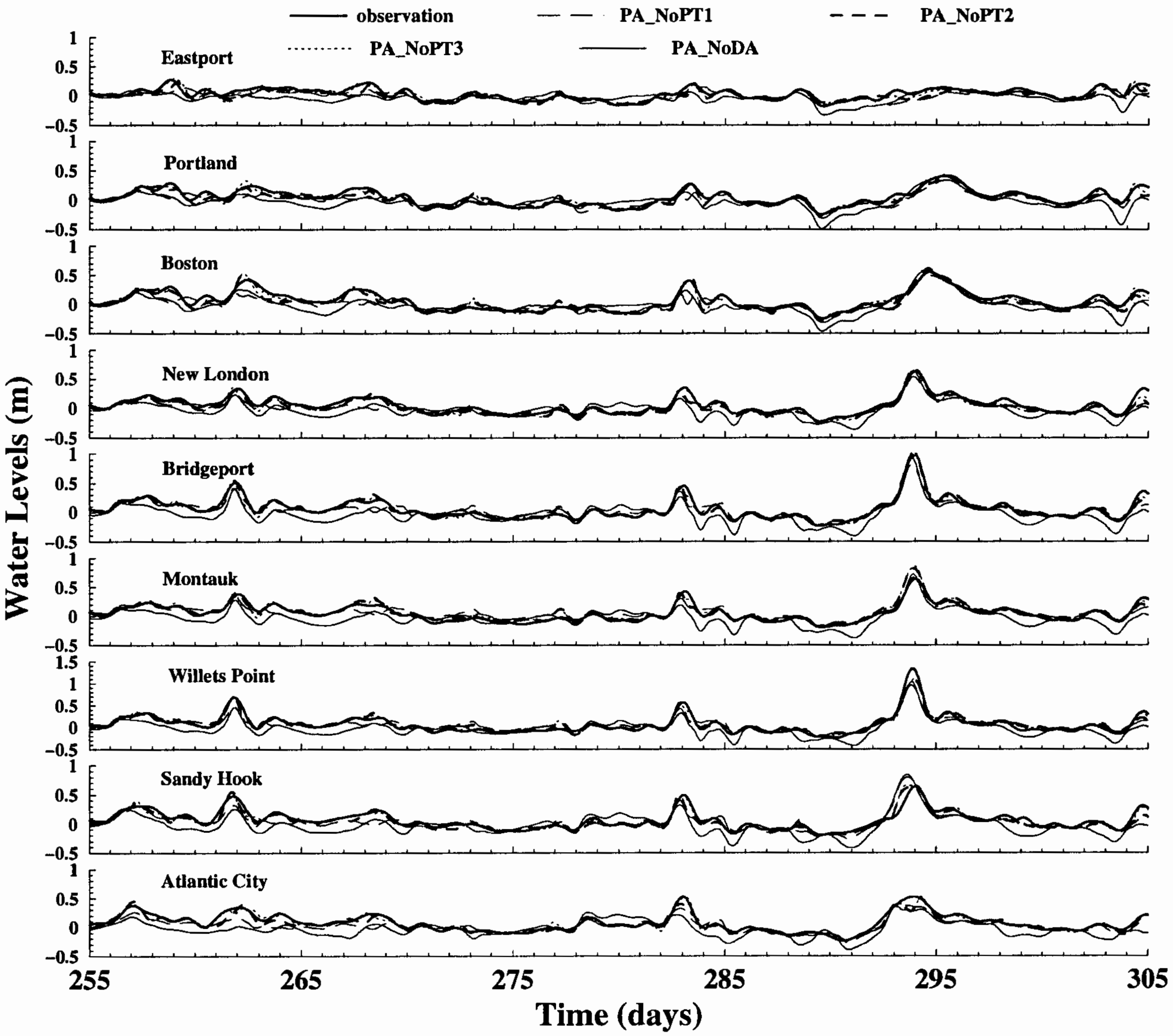

Figure 5.7. Time series of the observed and simulated subtidal water levels with and without data assimilation.

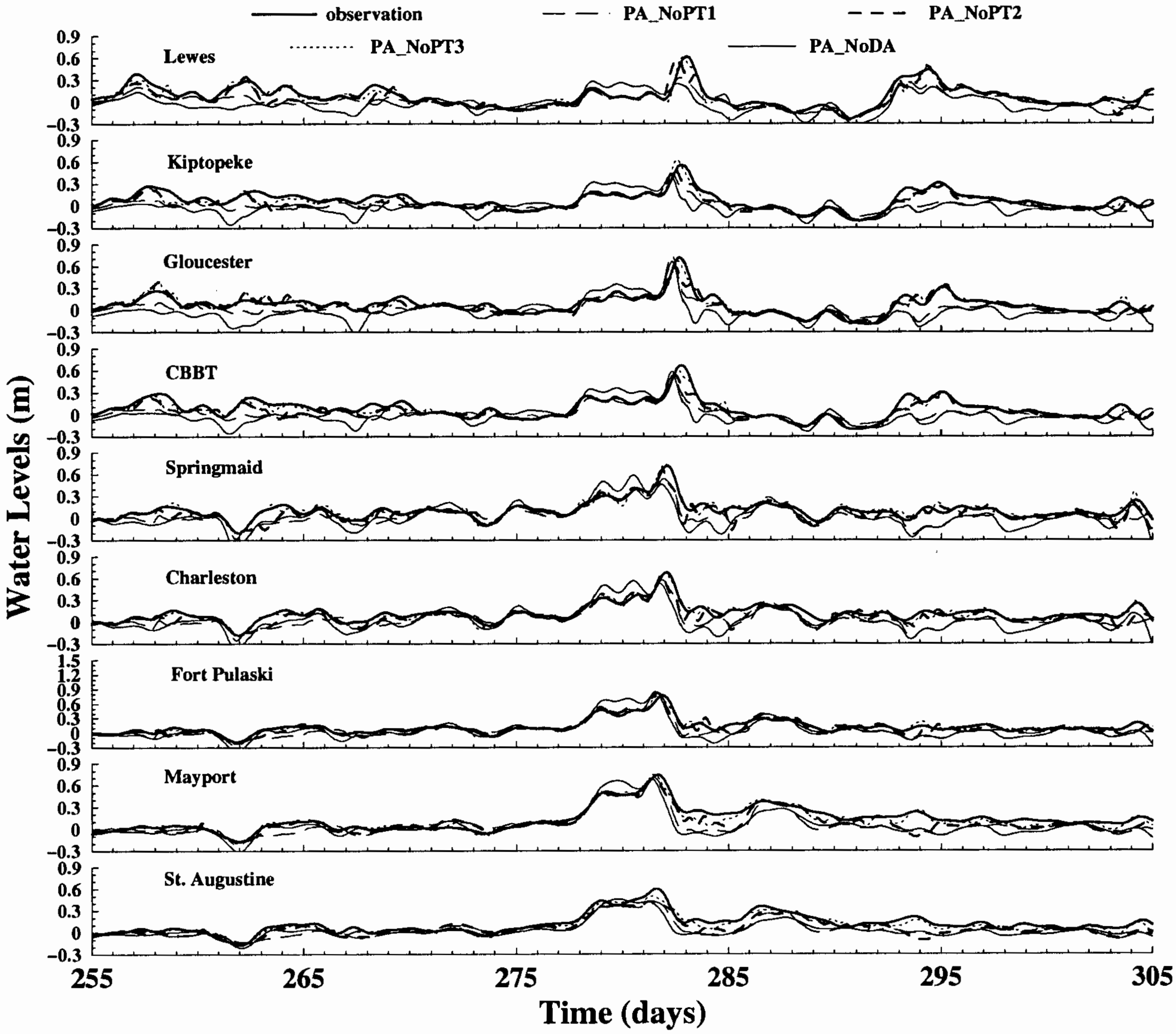

Figure 5.7. (Continued)

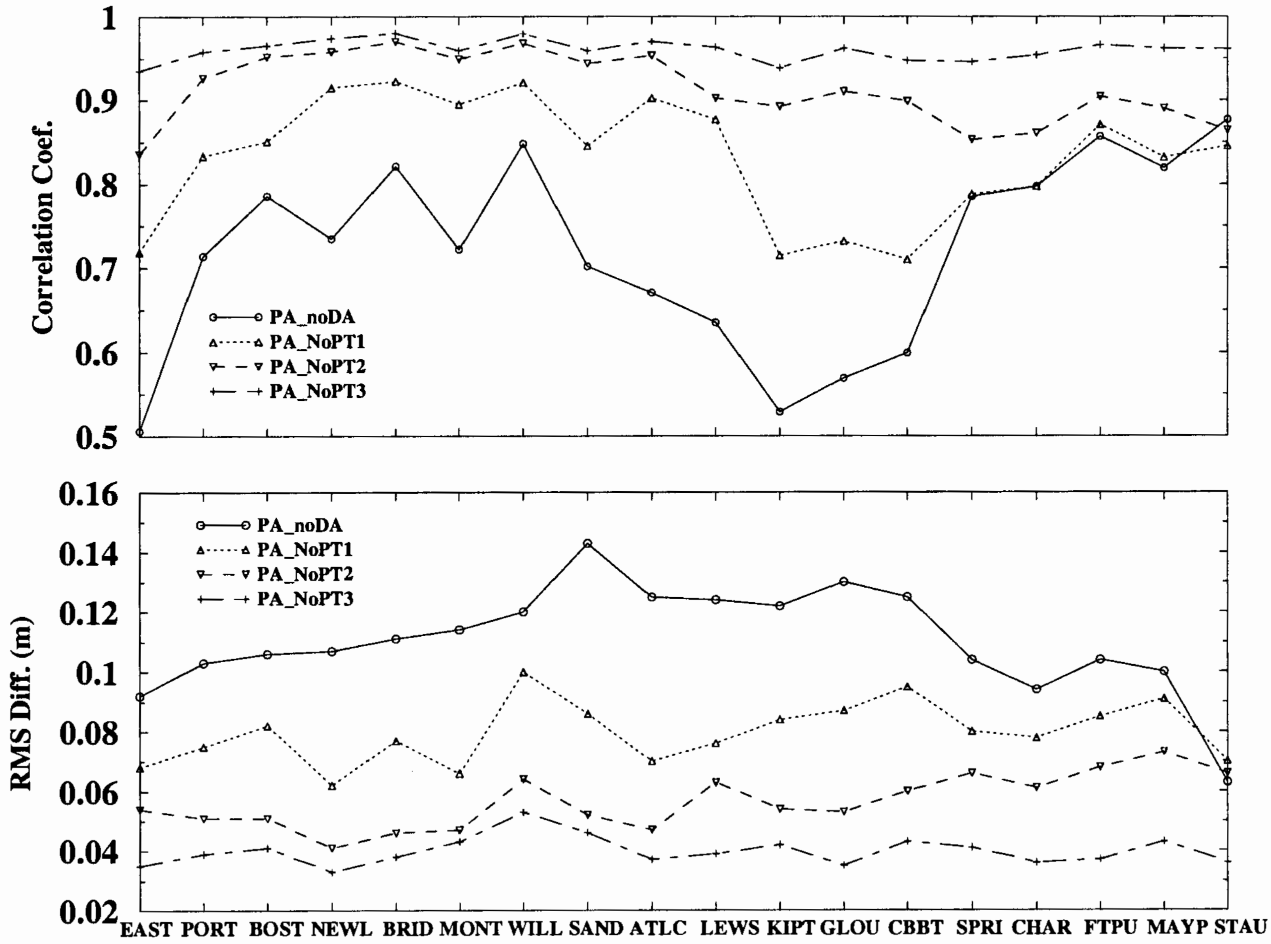

Figure 5.8. Comparison of correlation coefficients and RMS errors between the observed and simulated subtidal water levels from the experiments with and without data assimilation.

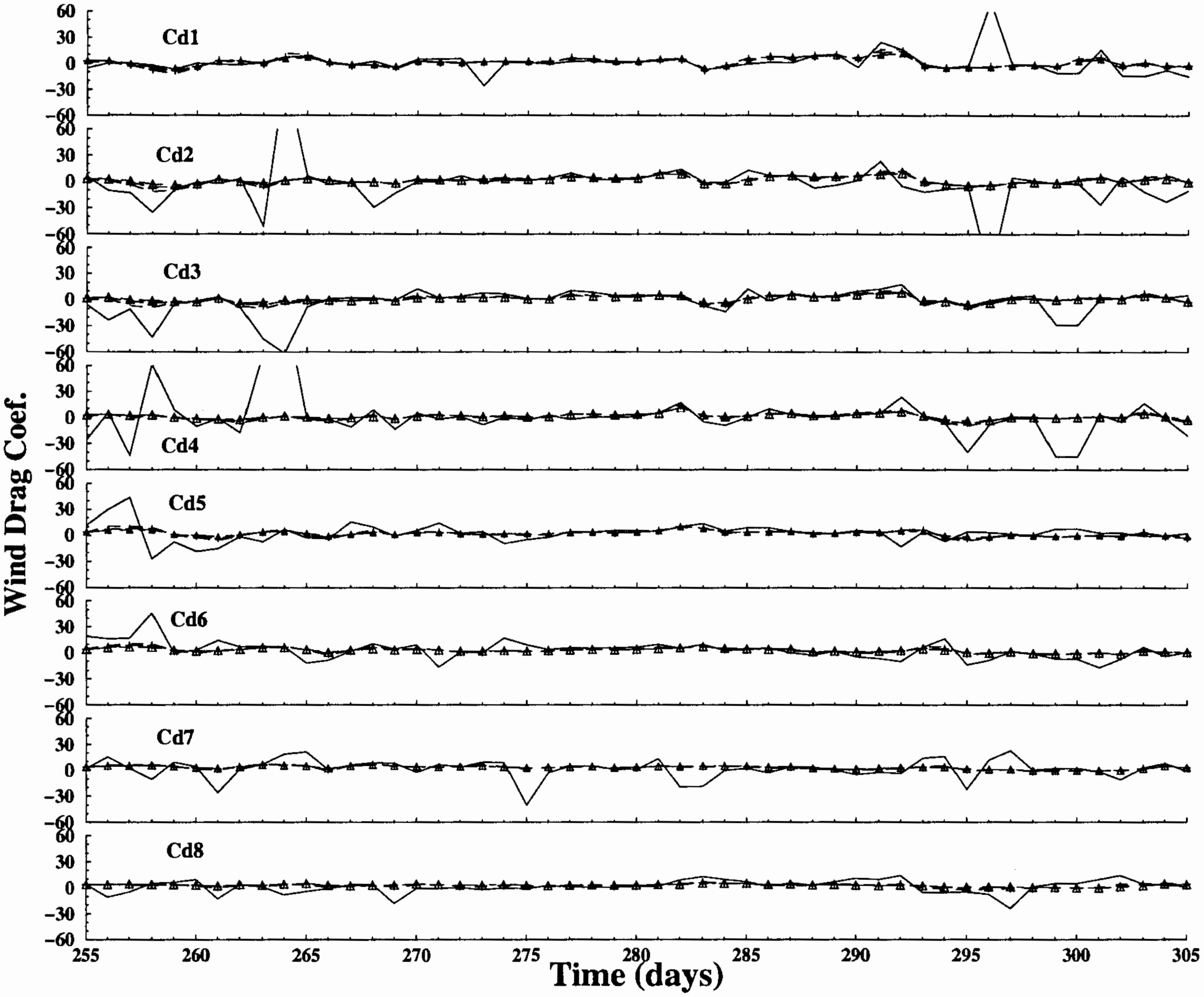

Figure 5.9. Time series of optimal values of C_d for the the data assimilation experiments with penalty terms. Solid line, PA_NoPT3; dashed line, PA_PT1; dashed line with plus, PA_PT2; dashed line with triangle, PA_PT3.

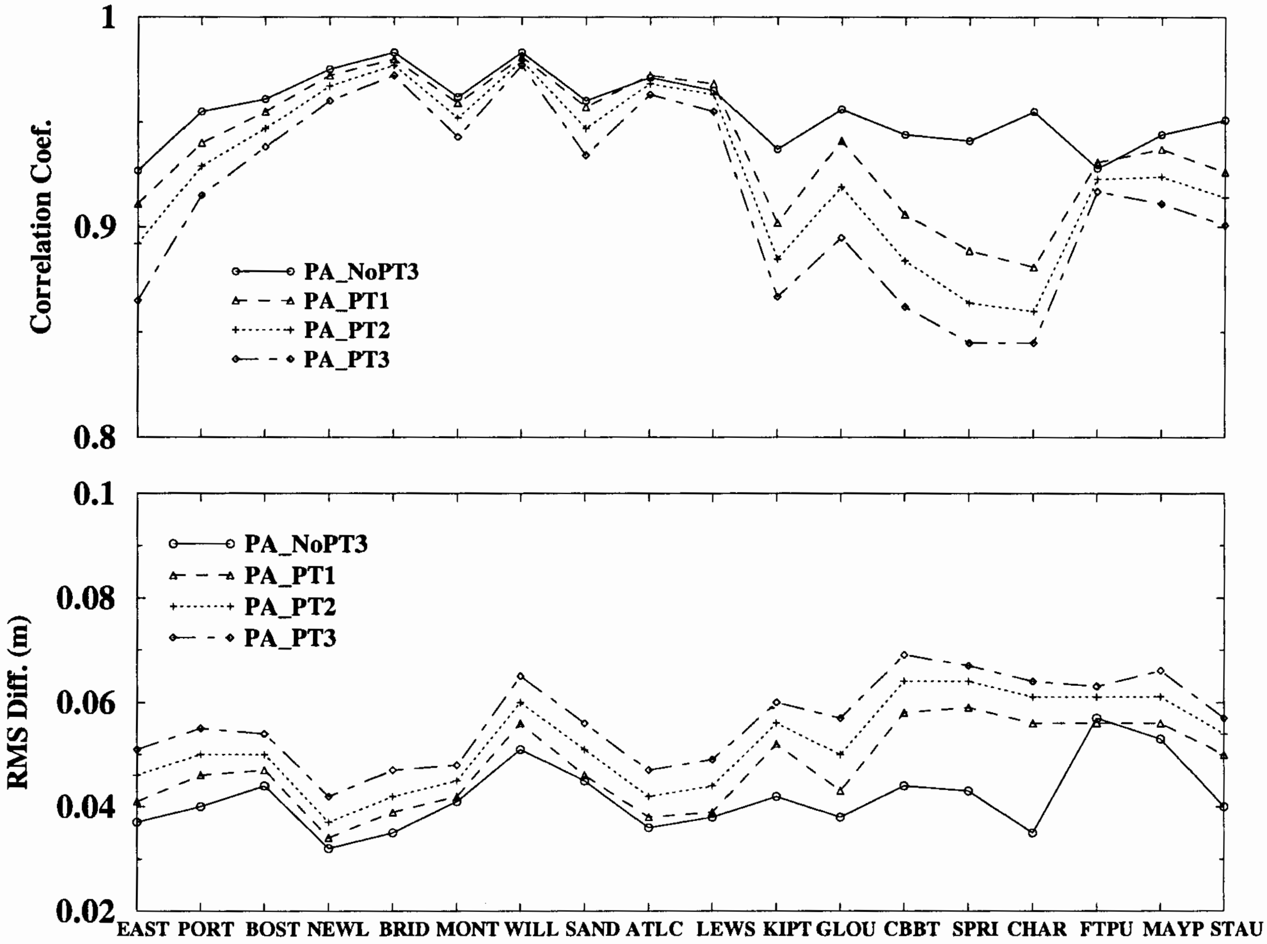

Figure 5.10. Correlation coefficients and RMS errors between the observed and simulated subtidal water levels from the data assimilation experiments with and without penalty terms.

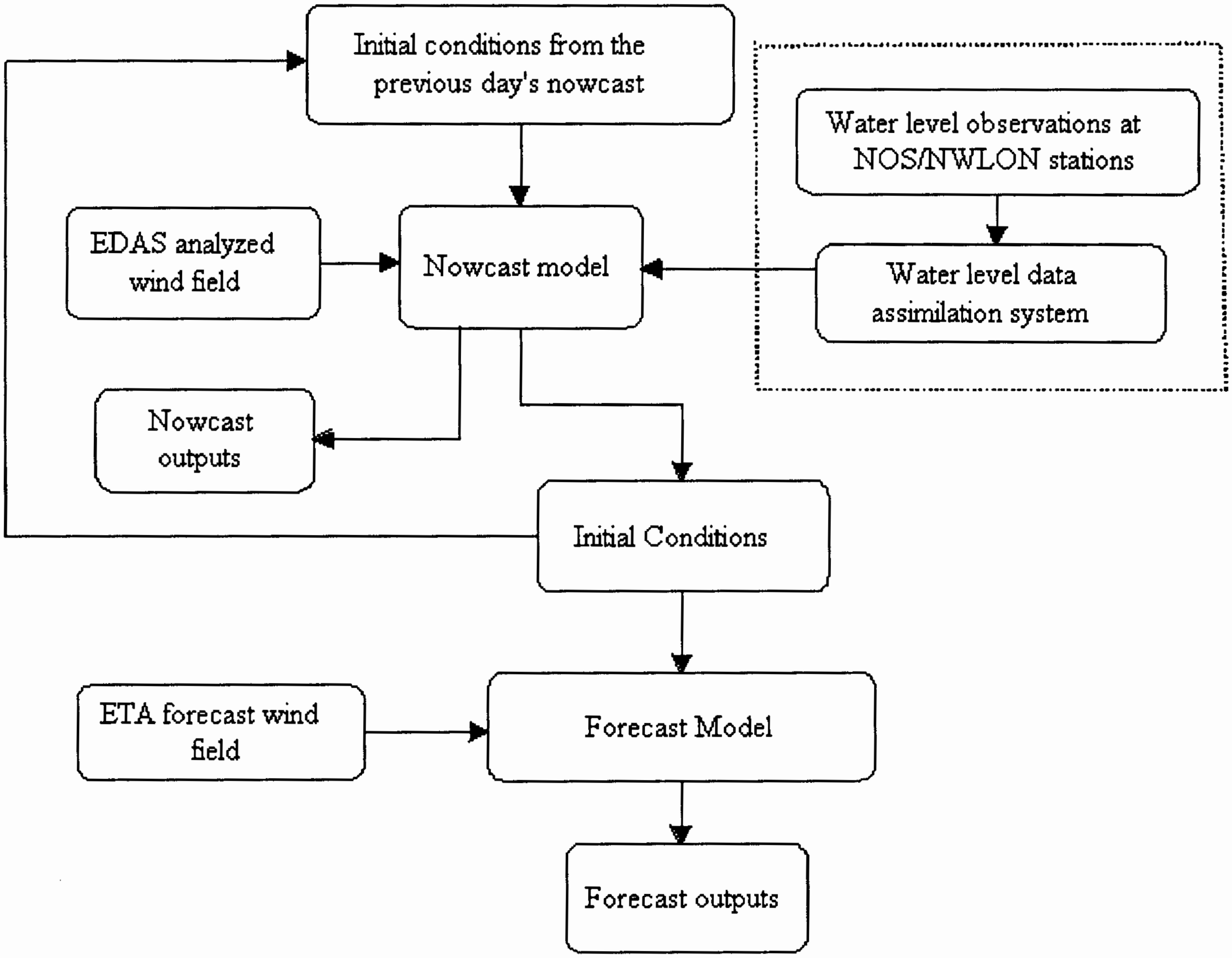

Figure 5.11. Flowchart of a 24-hour subtidal water level nowcast/forecast system.

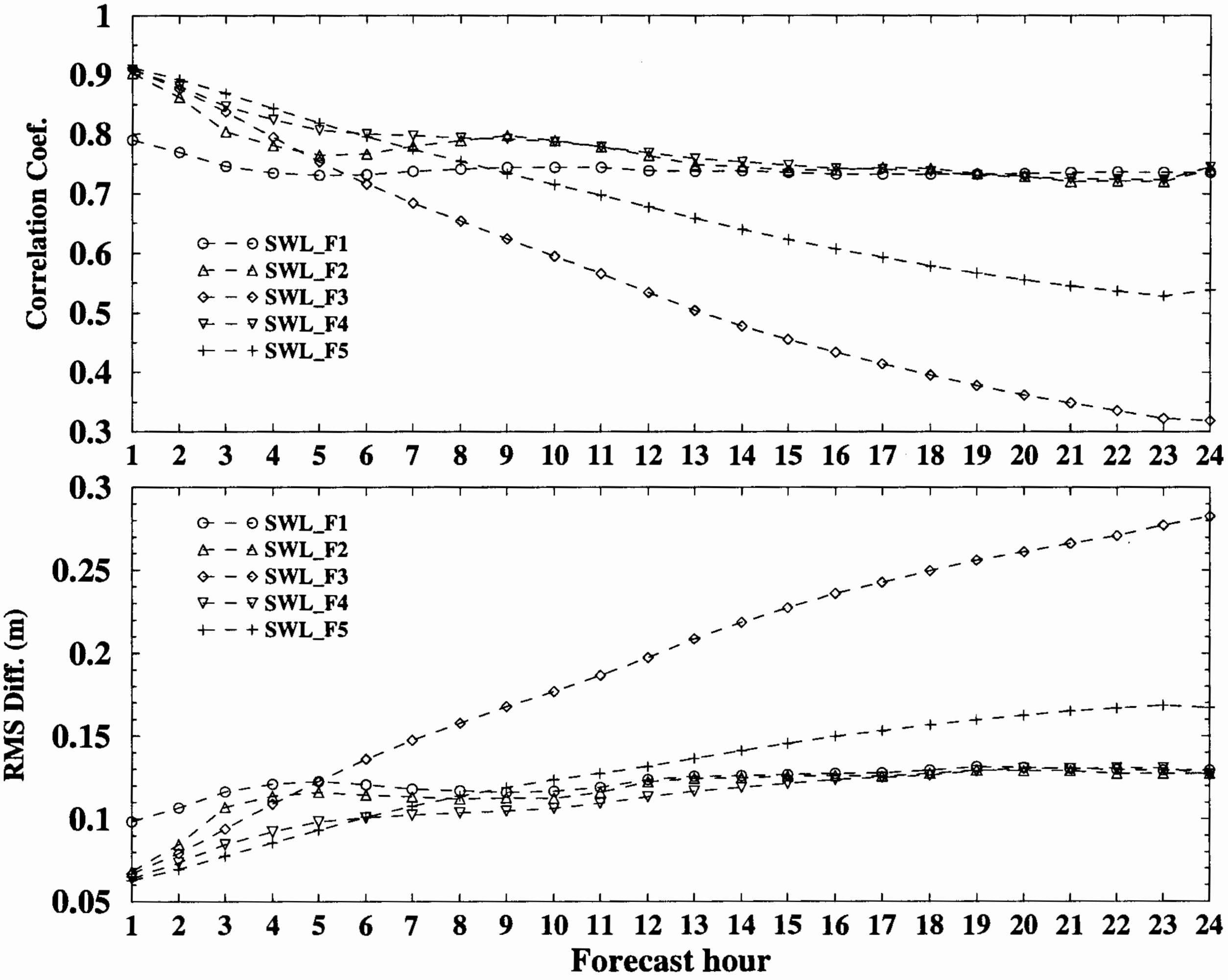

Figure 5.12. Average correlation coefficients and RMS errors for each forecast hour between the observed and forecasted subtidal water levels over 18 tide stations from the nowcast/forecast experiments.

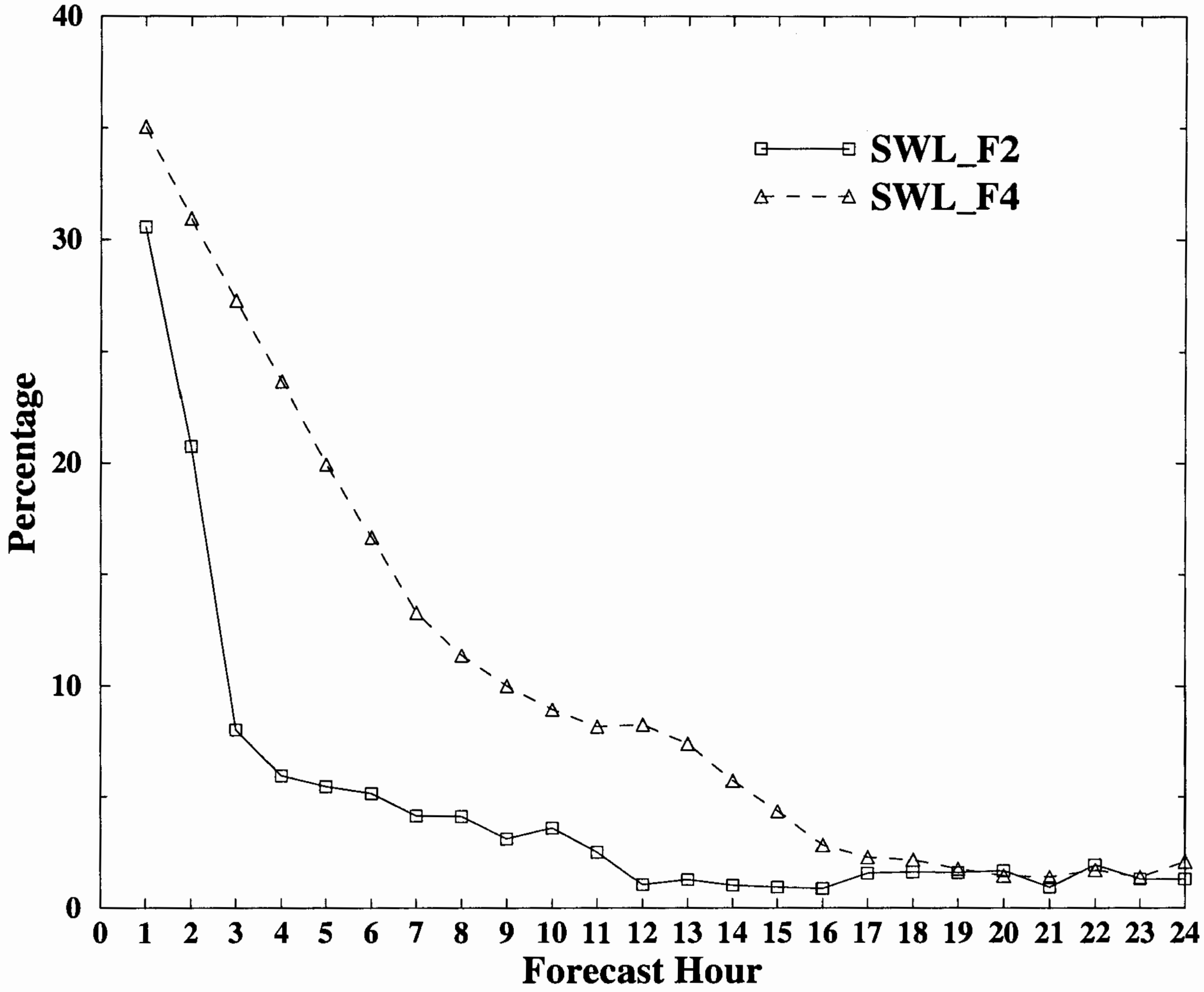

Figure 5.13. Average improvement in subtidal water level forecasts by applying water level data assimilation with and without penalty terms.

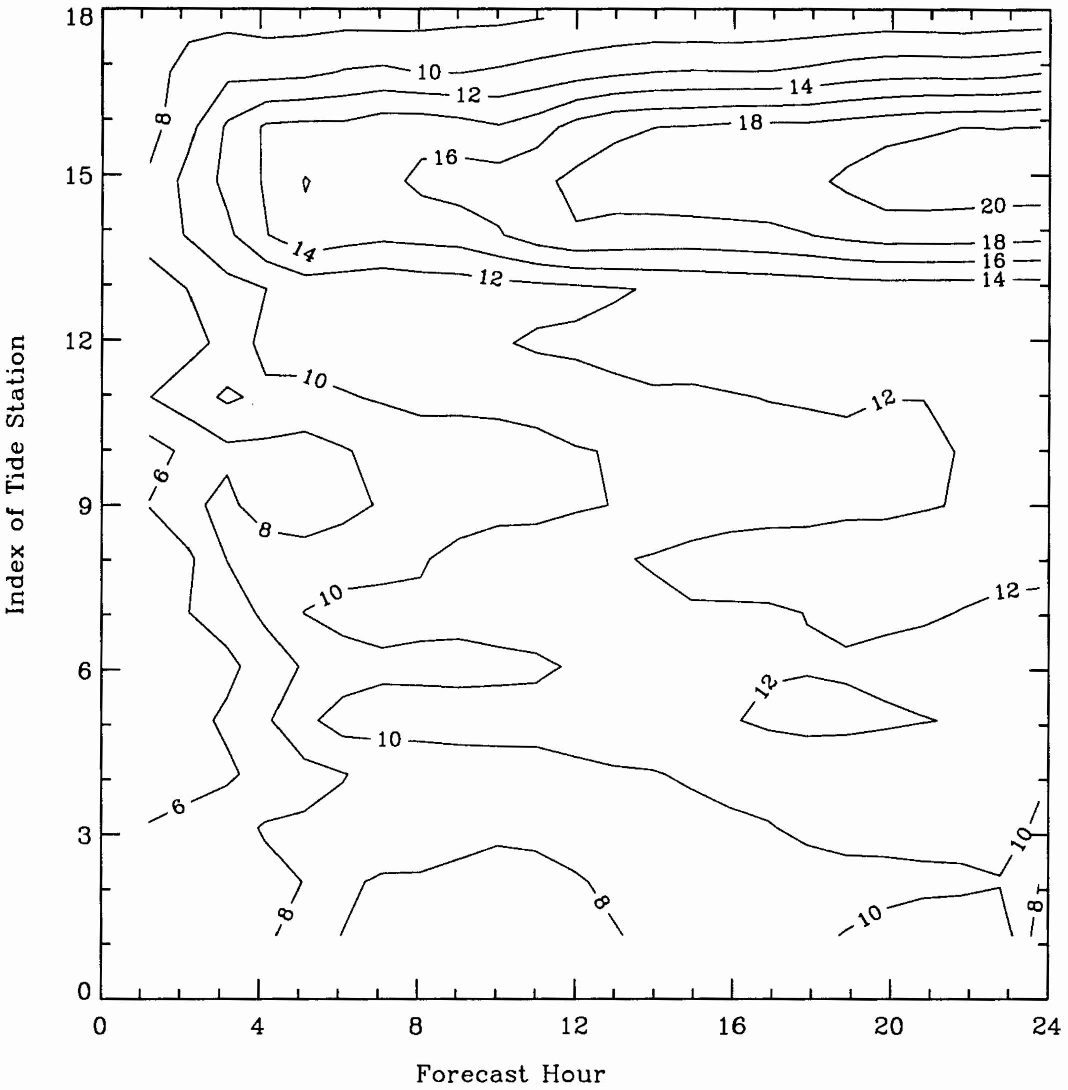

Figure 5.14. Contours of the RMS errors (in centimeters) as a function of the forecast hour and tide stations from the experiment SWL_F4.

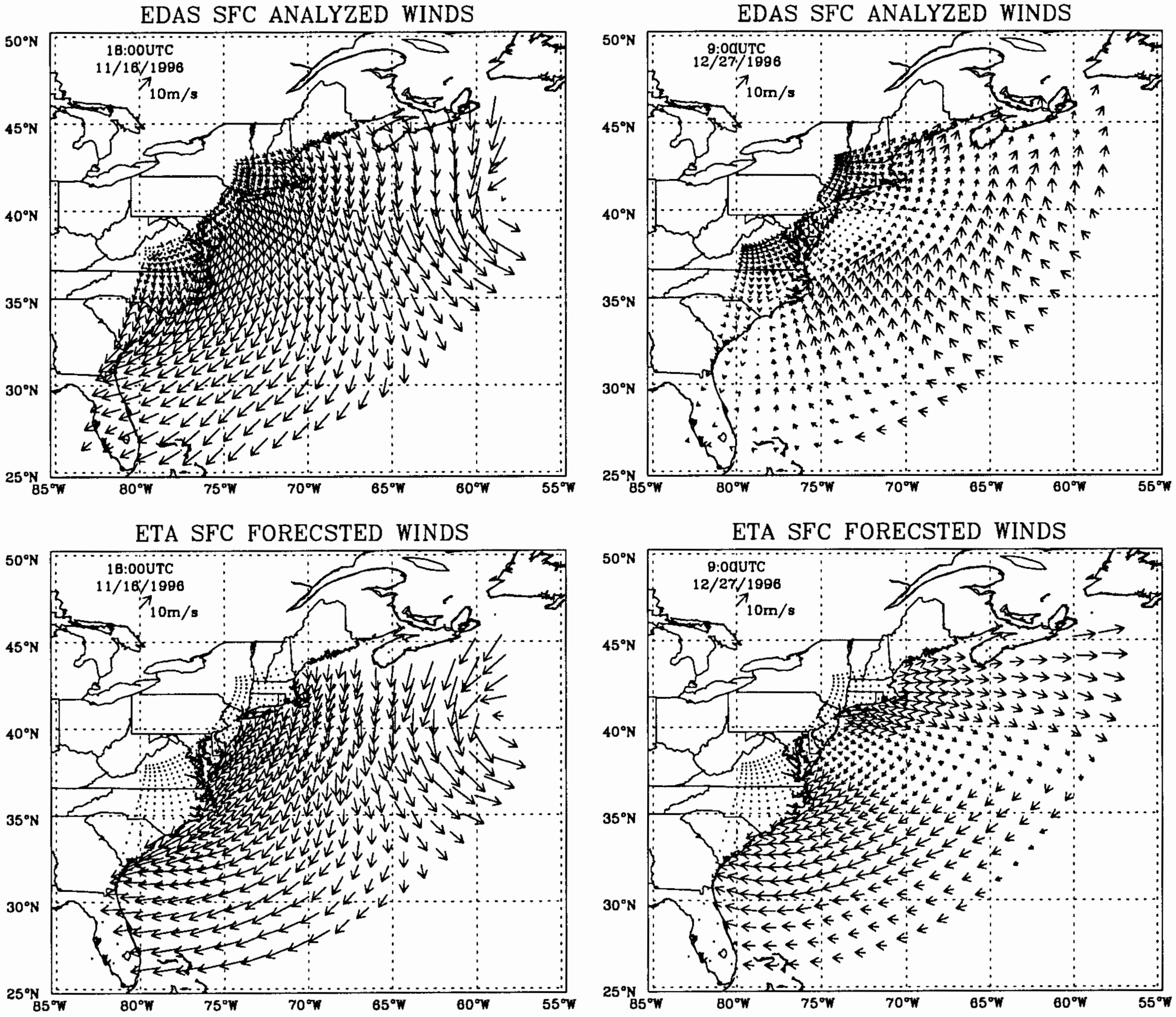

EDAS SFC ANALYZED WINDS

EDAS SFC ANALYZED WINDS

ETA SFC FORECSTED WINDS

ETA SFC FORECSTED WINDS

Figure 5.15. Comparison between the EDAS analyzed wind and ETA forecasted wind fields. The upper panels are EDAS analyzed winds and the lower panels are ETA forecasted winds.

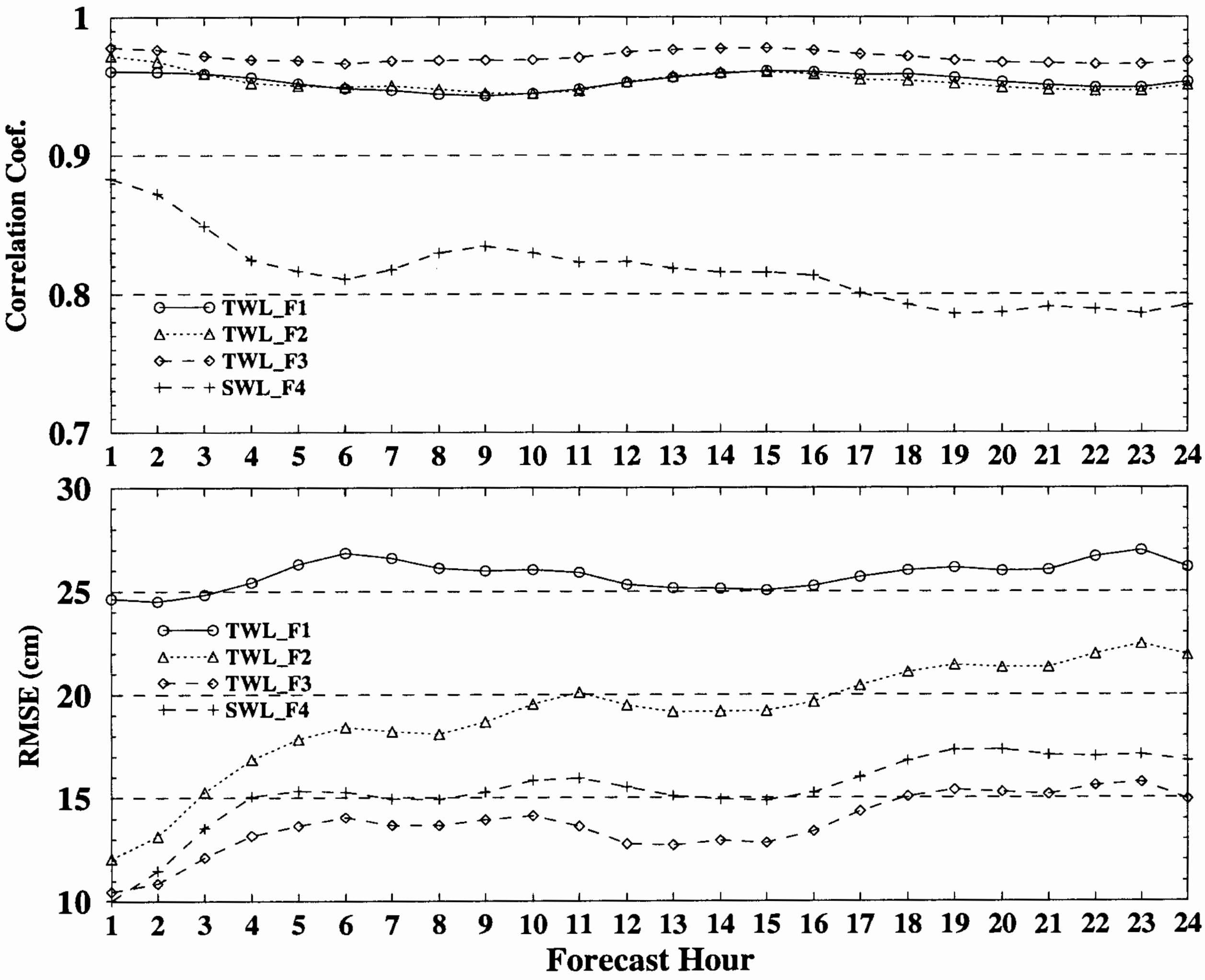

Figure 5.16. Average correlation coefficients and RMS errors of each forecast hour between the observed and forecasted water levels over 18 tide stations from the total water level nowcast/forecast experiments.

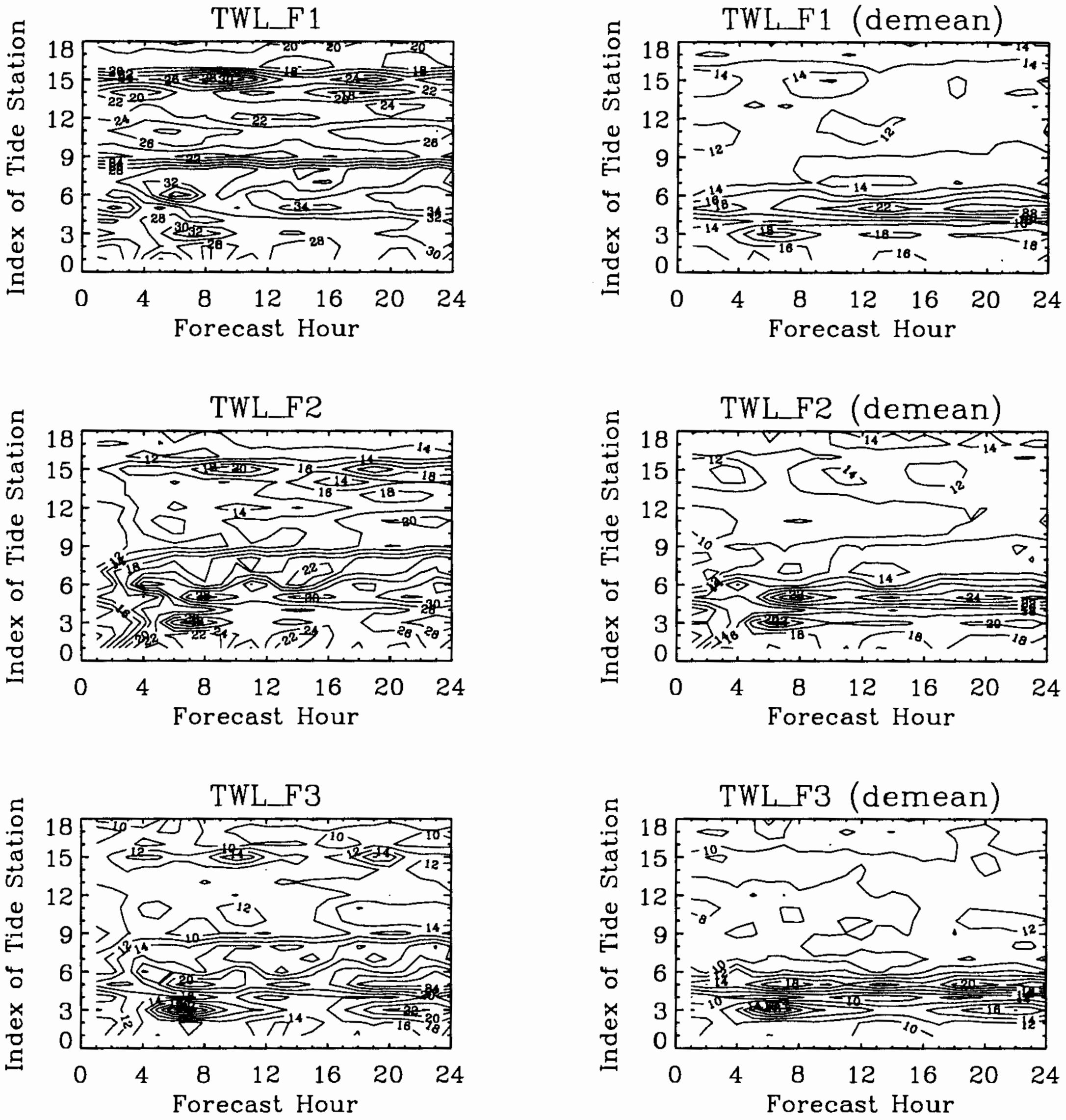

Figure 5.17. RMS error contours (in centimeters) of 24-hour total water level forecasts at different locations. The left panels represent RMS errors and the right panels represent RMS errors after the mean value was removed.

6. CONCLUSIONS

A water level data assimilation system for the East Coast of the United States has been developed to improve water level simulation and forecasts through adjustment of the open boundary conditions and surface wind drag coefficients. The system uses the two-dimensional Princeton Ocean Model with an orthogonal curvilinear grid. The adjoint technique is used to derive the gradient of the cost function. The correctness and performance of the data assimilation system are verified with identical twin experiments. The results show that gradient of the cost function can be efficiently computed with the adjoint approach. The true solutions of the control variable can be accurately recovered by assimilating pseudo-observations, even if the first guess values of the control variables are quite different from the true solution. The identical twin experiments also show that water level observational errors affect the convergence rate and performance of the minimization procedure.

Using data assimilation to compute the optimal tidal forcing along the boundary led to better results than using the tidal open boundary conditions from Schwiderski's global model. For this case, RMS errors at coastal stations are less than 7 cm.

Subtidal water levels were also assimilated to compute optimal surface wind drag coefficients, the results of which showed improvement even with one control variable. The most accurate simulated subtidal water levels were obtained with 16 control variables (using x- and y-direction pairs in 8 regions). In this case, the correlation coefficients at 18 water level stations were greater than 0.93, and the RMS errors were less than 5.3 cm. This experiment demonstrates that both the magnitude and direction of the wind stress need to be adjusted in order to minimize the cost function. Penalty terms should also be included in the cost function to assure the smoothness of the estimated optimal wind drag coefficient in space and time. Results from the experiments with the penalty terms indicate that the estimated optimal values of C_d are smoother in space and time than those without the penalty terms. However, the RMS error differences between the simulated subtidal water levels with and without the penalty terms are very small. Thus, adding the penalty terms leads to smoother solutions that still preserve the physical features of subtidal water levels.

The subtidal water level nowcast/forecast experiments demonstrated that most of the improvement in water level forecasts by applying water level data assimilation into the nowcast/forecast system occurred within the first 6 hours, with no significant differences thereafter. This indicates that the impact of the initial conditions from the nowcast on the next day's forecast is limited within 6 hours. The optimal values of C_d from the previous day's water level data assimilation cannot be directly applied in the next day's water level forecast due to changes in the surface wind field. These values can only be reasonably extended about 3-6 hours into the forecast. More experiments should be performed on how to extend the optimal values of C_d of the previous day to the next day's water level forecast.

For total water level forecasts, the best results were obtained from an experiment that simply adds astronomical tidal predictions to the optimal simulated subtial water levels. The average RMS errors of 24-hour water level forecasts over 18 stations are less than 16 cm, and the average correlation coefficients are greater than 0.96. However, such forecasts can only be made where observations are available. For the model forecasted total water levels (TWL_F2), The RMS errors of the 24-hour forecasts are in the range of 12-22 cm. In conclusion, tidal open boundary conditions and surface wind drag coefficients can be well estimated by assimilation of water level data along the coastal stations, thereby improving nowcast/forecast water level simulations.

Due to limitations in the number and spatial distribution of available water level observations (the real-time water level data are available at only 18 water level gauge stations within the model domain), a large number of control variables cannot be used in the data assimilation process. Sea surface height (SSH) data from satellite altimeters should help to alleviate this limitation. Combining water level gauge observations that are long-term in time with altimetry data that cover large spatial areas would improve the resolution of the wind drag coefficients, and thus the accuracy of the nowcast/forecast results.

ACKNOWLEDGEMENTS

The authors wish to thank Drs. Frank Aikman, Tom Eisler and Ed Myers for their valuable comments on the manuscript during the internal reviews. Special thanks to Dr. Kurt Hess for his constructive comments and editorial review. The lead author, Aijun Zhang, conducted this work while a UCAR visiting scientist.

REFERENCES

Aikman, F., G. L. Mellor, T. Ezer, D. Sheinin, P. Chen, L. Breaker, K. Bosley, and D. B. Rao, 1996. Towards an operational nowcast/forecast system for the U. S. East Coast. ***Modern Approaches to Data Assimilation in Ocean Modeling***, edited by P. Malanotte-Rizzoli, Elsevier Oceanographic Series 61, Amsterdam, the Netherlands, 347-376.

Baptista, A.M., M. Wilkin, P. Pearson, P. Turner, C. McCandlish, P.Barrett, S. Das, W. Sommerfield, M. Qi, N. Nangia, D. Jay, D. Long, C. Pu, J.Hunt, Z. Yang, E. Myers, J. Darland and A. Farrenkopf, 1998. Towards a Multi-Purpose Forecast System for the Columbia River Estuary. **Ocean Community Conference '98**, Baltimore, Maryland.

Bennett, A. F., and P. C. McIntosh, 1982. Open ocean modeling as an inverse problem: tidal theory. **J. Phys. Oceanogr.**,12, 1004-1018.

Bennett, A. F., 1985. Array design by inverse method. **Progress in Oceanography**, 15, Pergamon, 129-156.

Black, T. L., 1994. The new NMC mesoscale eta model: Description and forecast examples. Weather Forecasting, 9, 265-278.

Blumberg, A. F., and G. L. Mellor, 1987. A description of a three-dimensional coastal ocean circulation model. in: N.S. Heaps (Editor), **Three Dimensional Coastal Ocean Models**, Coastal and Estuarine Sciences 4, American. Geophysical Union, Washington D. C., pp1-16.

Cacuci, D. G., 1988. The forward and adjoint methods of sensitivity analysis. ***Uncertainty Analysis***, Yigal Ronen (Edts), CRC Press, 282pp.

Courtier, P., and O. Talagrand, 1990. Variational assimilation of meteorological observations with the direct and adjoint shallow-water equations. **Tellus**, 42A, 531-549.

Das, S. K., and R. W. Lardner, 1991. On the estimation of parameters of hydraulic models by assimilation of periodic tidal data. **J. Geophys. Res.**, Vol. 96, C8, 15187-15196.

Egbert, G. D., A. F. Bennett, and M.G.G. Foreman, 1994. TOPEX/POSEIDON tides estimated using a global inverse model. **J. Geophys. Res.**, 99(c12), 24821-24852.

Gilbert, J. C., and C. Lemarechal, 1989. Some numerical experiments with variable-storage quasi-Newton algorithms. **Mathematical Programming**, 45, 407-435.

Gross, T. F., K.T. Bosley, and K.W. Hess, 2000. The Chesapeake Bay operational forecast system (CBOFS): technical documentation. **NOAA Technical Report OCS/CO-OPS 1**, 69pp.

Hall, M. C. G., D. G. Cacuci, and M. E. Schlesinger, 1982. Sensitivity analysis of a radiative-convective model by adjoint method. **J. Atmos. Sci.**, 39, 2038-2050.

Lardner, R. W., 1993. Optimal control of open boundary conditions for a numerical tidal model. **Comput. Methods Appl. Mech. Eng.**, 102, 367-387.

Lardner, R. W., A. H. Al-Rabeh,and N. Gunay, 1993. Optimal estimation of parameters for a two-dimensional hydrodynamical model of the Arabian Gulf. **J. Geophys. Res.**, 98, 18229-18242.

Lardner, R. W., and Y. Song, 1995. Optimal estimation of eddy viscosity and friction coefficients for a quasi-three-dimensional numerical tidal model. **Atmosphere-Ocean**, 33(3), 581-611.

Large, W. G., and S. Pond, 1981. Open ocean momentum flux measurements in moderate to strong winds. **J. Phys. Oceanogr.**, Vol.11, 324-336.

Lawson, L. M., Y. H. Spitz, E. E. Hofmann, and R. B. Long, 1995. A data assimilation technique applied to a predator-prey model. **Bulletin of Mathematical Biology**, 57, 593-617.

Liu, D., and J. Nocedal, 1989. On the limited memory BFGS method for large scale optimization. **Mathematical Programming**, B 45, 503-528.

Malanotte-Rizzoli, P., and E. Tziperman, 1996. The Oceanographic data assimilation problem: overview, motivation and purposes. ***Modern Approaches to Data Assimilation in Ocean Modeling***. Edited by Malanotte-Rizzoli, Elsevier Science, 3-17.

Mellor, G. L., 1996. **User's guide for a three dimensional, primitive equation, numerical ocean model**. Princeton University, 40pp.

Nash, S. G., and J. Nocedal, 1989. A numerical study of the limited memory BFGS method and the truncated Newton method for large scale optimization. **Tech. Rep. NAM 2**, Northwestern University, Evanston, IL.

National Geophysical Data Center, 1985. Worldwide gridded bathymetry- DBDB5 5 minute latitude/longitude grid. **Data announcement 85-MGG-01**, NOAA/NGDC, Boulder, CO.

National Geophysical Data Center, 1988. NOS Hydrographic data base-expanded, digital bathymetric data for U.S. coastal waters. **Data announcement 87-MGG-12**, NOAA/NGDC, Boulder, CO.

Panchang, V. G., and J. J. O'Brien, 1989. On the determination of hydraulic model parameters using the adjoint state formulation. **Modeling Marine Systems**. Edited by A. M. Davies, CRC Press, Boca Racon, 6-18.

Parker, B. B., 1997. Development of model-based regional nowcasting/forecasting systems. In: **Estuarine and Coastal Modeling. Proceedings of the Fifth International Conference**, M. L. Spaulding and A. F. Blumberg (eds), ASCE, N.Y., 355-373.

Rogers, E., D. G. Deaven, and G. J. DiMego, 1995. The regional analysis system for the operational eta model: Original 80-km configuration and recent changes. **Weather forecasting**, 10, 810-825.

Sasaki, Y., 1970. Some basic formalisms in numerical variational analysis. **Monthly Weather Review**, Vol.98, No.12, 875-883.

Schmalz, R. A., 2000. Three-dimensional hydrodynamic model developments for a Galveston Bay nowcast/forecast system. **NOAA Technical Report NOS CS 9**, 167pp.

Schwiderski, E. W., 1980. On charting global ocean tides. **Rev. Geophys. And Space Phys.**, 18, 243-268.

Seiler, U., 1993. Estimation of open boundary conditions with the adjoint method. **J. Geophys. Res.**, 98, 22855-22870.

Wei, E. J.and M. Chen, 2001. Hydrodynamic model development for the port of New York/New Jersey water level and current nowcast/forecast model system. NOAA Technical Report NOS CS 12, 44pp.

Yu, L., and J. J. O'Brien, 1991. Variational estimation of the wind stress drag coefficient and the oceanic eddy viscosity profile. **J. Phys. Oceanogr.**, Vol. 21, 709-719.

Yu, L., and J. J. O'Brien, 1992. On the initial condition in parameter estimation. **J. Phys. Oceanogr.**, 22, 1361-1364.

Zhang, A., 2000. Assimilation of water level data into a coastal hydrodynamic model by an adjoint variational optimal technique. **Ph.D. dissertation**, Institute of Oceanology, Chinese Academy of Sciences, 166pp.

Zou, X., I. M. Navon, and F. X. Le Dimet, 1992. Incomplete observations and control of gravity waves in variational data assimilation. **Tellus**, 44A, 273-296.

Zou, X., A. Barcilon, I. M. Navon, J. Whitaker, and D. G. Cacuci, 1993. An adjoint sensitivity study of blocking in a two-layer isentropic model. **Mon. Wea. Rev.**, 12, 2833-2857.

APPENDIX A. VARIATIONAL OF LINEAR TERMS OF THE COST FUNCTION

$$T1 = \sum_{n=2}^{N}\sum_{i=2}^{IM-1}\sum_{j=3}^{JM-1}\lambda_{hi,j}^{n}\delta h_{i,j}^{n}$$

$$T2 = -\sum_{n=2}^{N}\sum_{i=2}^{IM-1}\sum_{j=3}^{JM-1}\lambda_{hi,j}^{n}\delta \overline{h}_{i,j}^{n-1} = -\sum_{n=1}^{N-1}\sum_{i=2}^{IM-1}\sum_{j=3}^{JM-1}\lambda_{hi,j}^{n+1}\delta \overline{h}_{i,j}^{n}$$

$$T3 = \sum_{n=2}^{N}\sum_{i=2}^{IM-1}\sum_{j=3}^{JM-1}O_{i,j}A_{i+1,j}\lambda_{hi,j}^{n}\delta U_{i+1,j}^{n-1} = \sum_{n=2}^{N-1}\sum_{i=3}^{IM}\sum_{j=3}^{JM-1}O_{i-1,j}A_{i,j}\lambda_{hi-1,j}^{n+1}\delta U_{i,j}^{n}$$

$$T4 = -\sum_{n=2}^{N}\sum_{i=2}^{IM-1}\sum_{j=3}^{JM-1}O_{i,j}A_{i,j}\lambda_{hi,j}^{n}\delta U_{i,j}^{n-1} = -\sum_{n=1}^{N-1}\sum_{i=2}^{IM-1}\sum_{j=3}^{JM-1}O_{i,j}A_{i,j}\lambda_{hi,j}^{n+1}\delta U_{i,j}^{n}$$

$$T5 = \sum_{n=2}^{N}\sum_{i=2}^{IM-1}\sum_{j=3}^{JM-1}O_{i,j}B_{i,j+1}\lambda_{hi,j}^{n}\delta V_{i,j+1}^{n-1} = \sum_{n=1}^{N-1}\sum_{i=2}^{IM-1}\sum_{j=4}^{JM}O_{i,j-1}B_{i,j}\lambda_{hi,j-1}^{n+1}\delta V_{i,j}^{n}$$

$$T6 = -\sum_{n=2}^{N}\sum_{i=2}^{IM-1}\sum_{j=3}^{JM-1}O_{i,j}B_{i,j}\lambda_{hi,j}^{n}\delta V_{i,j}^{n-1} = -\sum_{n=1}^{N-1}\sum_{i=2}^{IM-1}\sum_{j=3}^{JM-1}O_{i,j}B_{i,j}\lambda_{hi,j}^{n+1}\delta V_{i,j}^{n}$$

$$T7 = \sum_{n=2}^{N}\sum_{i=2}^{IM-1}\sum_{j=2}^{JM-1}\lambda_{ui,j}^{n}\delta U_{i,j}^{n}$$

$$T8 = -\sum_{n=2}^{N}\sum_{i=2}^{IM-1}\sum_{j=2}^{JM-1}\lambda_{ui,j}^{n}\delta \overline{U}_{i,j}^{n-1} = -\sum_{n=1}^{N-1}\sum_{i=2}^{IM-1}\sum_{j=2}^{JM-1}\lambda_{ui,j}^{n+1}\delta \overline{U}_{i,j}^{n}$$

$$T9 = -\sum_{n=2}^{N}\sum_{i=2}^{IM-1}\sum_{j=2}^{JM-1}\frac{P_{i,j}}{4}f_{i,j}H_{i,j}\lambda_{ui,j}^{n}\delta V_{i,j}^{n-1} = -\sum_{n=1}^{N-1}\sum_{i=2}^{IM-1}\sum_{j=2}^{JM-1}\frac{P_{i,j}}{4}f_{i,j}H_{i,j}\lambda_{ui,j}^{n+1}\delta V_{i,j}^{n}$$

$$T10 = -\sum_{n=2}^{N}\sum_{i=2}^{IM-1}\sum_{j=2}^{JM-1}\frac{P_{i,j}}{4}f_{i,j}H_{i,j}\lambda_{ui,j}^{n}\delta V_{i,j+1}^{n-1} = -\sum_{n=1}^{N-1}\sum_{i=2}^{IM-1}\sum_{j=3}^{JM}\frac{P_{i,j-1}}{4}f_{i,j-1}H_{i,j-1}\lambda_{ui,j-1}^{n+1}\delta V_{i,j}^{n}$$

$$T11 = -\sum_{n=2}^{N}\sum_{i=2}^{IM-1}\sum_{j=2}^{JM-1}\frac{P_{i,j}}{4}f_{i-1,j}H_{i-1,j}\lambda_{ui,j}^{n}\delta V_{i-1,j+1}^{n-1} = -\sum_{n=1}^{N-1}\sum_{i=1}^{IM-2}\sum_{j=3}^{JM}\frac{P_{i+1,j-1}}{4}f_{i,j-1}H_{i,j-1}\lambda_{ui+1,j-1}^{n+1}\delta V_{i,j}^{n}$$

$$T12 = -\sum_{n=2}^{N}\sum_{i=2}^{IM-1}\sum_{j=2}^{JM-1}\frac{P_{i,j}}{4}f_{i-1,j}H_{i-1,j}\lambda_{ui,j}^{n}\delta V_{i-1,j}^{n-1} = -\sum_{n=1}^{N-1}\sum_{i=1}^{IM-2}\sum_{j=2}^{JM-1}\frac{P_{i+1,j}}{4}f_{i,j}H_{i,j}\lambda_{ui+1,j}^{n+1}\delta V_{i,j}^{n}$$

$$T13 = \sum_{n=2}^{N}\sum_{i=2}^{IM-1}\sum_{j=2}^{JM-1}Q_{i,j}(1-2\alpha)\lambda_{ui,j}^{n}\delta h_{i,j}^{n-1} = \sum_{n=1}^{N-1}\sum_{i=2}^{IM-1}\sum_{j=2}^{JM-1}Q_{i,j}(1-2\alpha)\lambda_{ui,j}^{n+1}\delta h_{i,j}^{n}$$

$$T14 = -\sum_{n=2}^{N}\sum_{i=2}^{IM-1}\sum_{j=2}^{JM-1}Q_{i,j}(1-2\alpha)\lambda_{ui,j}^{n}\delta h_{i-1,j}^{n-1} = -\sum_{n=1}^{N-1}\sum_{i=1}^{IM-2}\sum_{j=2}^{JM-1}Q_{i+1,j}(1-2\alpha)\lambda_{ui+1,j}^{n+1}\delta h_{i,j}^{n}$$

$$T15 = \sum_{n=2}^{N}\sum_{i=2}^{IM-1}\sum_{j=2}^{JM-1}Q_{i,j}\alpha\lambda_{ui,j}^{n}\delta h_{i,j}^{n}$$

$$T16 = -\sum_{n=2}^{N}\sum_{i=2}^{IM-1}\sum_{j=2}^{JM-1} Q_{i,j}\alpha\lambda_{ui,j}^{n}\delta h_{i-1,j}^{n} = -\sum_{n=2}^{N}\sum_{i=1}^{IM-2}\sum_{j=2}^{JM-1} Q_{i+1,j}\alpha\lambda_{ui+1,j}^{n}\delta h_{i,j}^{n}$$

$$T17 = \sum_{n=2}^{N}\sum_{i=2}^{IM-1}\sum_{j=2}^{JM-1} Q_{i,j}\alpha\lambda_{ui,j}^{n}\delta \overline{h}_{i,j}^{n-1} = \sum_{n=1}^{N-1}\sum_{i=2}^{IM-1}\sum_{j=2}^{JM-1} Q_{i,j}\alpha\lambda_{ui,j}^{n+1}\delta \overline{h}_{i,j}^{n}$$

$$T18 = -\sum_{n=2}^{N}\sum_{i=2}^{IM-1}\sum_{j=2}^{JM-1} Q_{i,j}\alpha\lambda_{ui,j}^{n}\delta \overline{h}_{i-1,j}^{n-1} = -\sum_{n=1}^{N-1}\sum_{i=1}^{IM-2}\sum_{j=2}^{JM-1} Q_{i+1,j}\alpha\lambda_{ui+1,j}^{n+1}\delta \overline{h}_{i,j}^{n}$$

$$T19 = \sum_{n=2}^{N}\sum_{i=2}^{IM-1}\sum_{j=2}^{JM-1} P_{i,j}C_{b}\lambda_{ui,j}^{n}\delta \overline{U}_{i,j}^{n-1} = \sum_{n=1}^{N-1}\sum_{i=2}^{IM-1}\sum_{j=2}^{JM-1} P_{i,j}C_{b}\lambda_{ui,j}^{n+1}\delta \overline{U}_{i,j}^{n}$$

$$T20 = \sum_{n=2}^{N}\sum_{i=2}^{IM-1}\sum_{j=3}^{JM-1} \lambda_{vi,j}^{n}\delta V_{i,j}^{n}$$

$$T21 = -\sum_{n=2}^{N}\sum_{i=2}^{IM-1}\sum_{j=3}^{JM-1} \lambda_{vi,j}^{n}\delta \overline{V}_{i,j}^{n-1} = -\sum_{n=1}^{N-1}\sum_{i=2}^{IM-1}\sum_{j=3}^{JM-1} \lambda_{vi,j}^{n+1}\delta \overline{V}_{i,j}^{n}$$

$$T22 = \sum_{n=2}^{N}\sum_{i=2}^{IM-1}\sum_{j=3}^{JM-1} \frac{R_{i,j}}{4} f_{i,j}H_{i,j}\lambda_{vi,j}^{n}\delta U_{i,j}^{n-1} = \sum_{n=1}^{N-1}\sum_{i=2}^{IM-1}\sum_{j=3}^{JM-1} \frac{R_{i,j}}{4} f_{i,j}H_{i,j}\lambda_{vi,j}^{n+1}\delta U_{i,j}^{n}$$

$$T23 = \sum_{n=2}^{N}\sum_{i=2}^{IM-1}\sum_{j=3}^{JM-1} \frac{R_{i,j}}{4} f_{i,j}H_{i,j}\lambda_{vi,j}^{n}\delta U_{i+1,j}^{n-1} = \sum_{n=1}^{N-1}\sum_{i=3}^{IM}\sum_{j=3}^{JM-1} \frac{R_{i-1,j}}{4} f_{i-1,j}H_{i-1,j}\lambda_{vi-1,j}^{n+1}\delta U_{i,j}^{n}$$

$$T24 = \sum_{n=2}^{N}\sum_{i=2}^{IM-1}\sum_{j=3}^{JM-1} \frac{R_{i,j}}{4} f_{i,j-1}H_{i,j-1}\lambda_{vi,j}^{n}\delta U_{i+1,j-1}^{n-1} = \sum_{n=1}^{N-1}\sum_{i=3}^{IM}\sum_{j=2}^{JM-2} \frac{R_{i-1,j+1}}{4} f_{i-1,j}H_{i-1,j}\lambda_{vi-1,j+1}^{n+1}\delta U_{i,j}^{n}$$

$$T25 = \sum_{n=2}^{N}\sum_{i=2}^{IM-1}\sum_{j=3}^{JM-1} \frac{R_{i,j}}{4} f_{i,j-1}H_{i,j-1}\lambda_{vi,j}^{n}\delta U_{i,j-1}^{n-1} = \sum_{n=1}^{N-1}\sum_{i=2}^{IM-1}\sum_{j=2}^{JM-2} \frac{R_{i,j+1}}{4} f_{i,j}H_{i,j}\lambda_{vi,j+1}^{n+1}\delta U_{i,j}^{n}$$

$$T26 = \sum_{n=2}^{N}\sum_{i=2}^{IM-1}\sum_{j=3}^{JM-1} S_{i,j}(1-2\alpha)\lambda_{vi,j}^{n}\delta h_{i,j}^{n-1} = \sum_{n=1}^{N-1}\sum_{i=2}^{IM-1}\sum_{j=3}^{JM-1} S_{i,j}(1-2\alpha)\lambda_{vi,j}^{n+1}\delta h_{i,j}^{n}$$

$$T27 = -\sum_{n=2}^{N}\sum_{i=2}^{IM-1}\sum_{j=3}^{JM-1} S_{i,j}(1-2\alpha)\lambda_{vi,j}^{n}\delta h_{i,j-1}^{n-1} = -\sum_{n=1}^{N-1}\sum_{i=2}^{IM-1}\sum_{j=2}^{JM-2} S_{i,j+1}(1-2\alpha)\lambda_{vi,j+1}^{n+1}\delta h_{i,j}^{n}$$

$$T28 = \sum_{n=2}^{N}\sum_{i=2}^{IM-1}\sum_{j=3}^{JM-1} S_{i,j}\alpha\lambda_{vi,j}^{n}\delta h_{i,j}^{n}$$

$$T29 = -\sum_{n=2}^{N}\sum_{i=2}^{IM-1}\sum_{j=3}^{JM-1} S_{i,j}\alpha\lambda_{vi,j}^{n}\delta h_{i,j-1}^{n} = -\sum_{n=2}^{N}\sum_{i=2}^{IM-1}\sum_{j=2}^{JM-2} S_{i,j+1}\alpha\lambda_{vi,j+1}^{n}\delta h_{i,j}^{n}$$

$$T30 = \sum_{n=2}^{N}\sum_{i=2}^{IM-1}\sum_{j=3}^{JM-1} S_{i,j}\alpha\lambda_{vi,j}^{n}\delta \overline{h}_{i,j}^{n-1} = \sum_{n=1}^{N-1}\sum_{i=2}^{IM-1}\sum_{j=3}^{JM-1} S_{i,j}\alpha\lambda_{vi,j}^{n+1}\delta \overline{h}_{i,j}^{n}$$

$$T31 = -\sum_{n=2}^{N}\sum_{i=2}^{IM-1}\sum_{j=3}^{JM-1} S_{i,j}\alpha\lambda_{vi,j}^{n}\delta \overline{h}_{i,j-1}^{n-1} = -\sum_{n=1}^{N-1}\sum_{i=2}^{IM-1}\sum_{j=2}^{JM-2} S_{i,j+1}\alpha\lambda_{vi,j+1}^{n+1}\delta \overline{h}_{i,j}^{n}$$

$$T32 = \sum_{n=2}^{N}\sum_{i=2}^{IM-1}\sum_{j=3}^{JM-1} R_{i,j}C_{b}\lambda_{vi,j}^{n}\delta \overline{V}_{i,j}^{n-1} = \sum_{n=1}^{N-1}\sum_{i=2}^{IM-1}\sum_{j=3}^{JM-1} R_{i,j}C_{b}\lambda_{vi,j}^{n+1}\delta \overline{V}_{i,j}^{n}$$

$$T33 = \sum_{n=2}^{N} \sum_{i=2}^{IM-1} \sum_{j=1}^{JM-1} \lambda_{\bar{h}\,i,j}^{n} \delta \bar{h}_{i,j}^{n}$$

$$T34 = -\sum_{n=2}^{N} \sum_{i=2}^{IM-1} \sum_{j=2}^{JM-1} \lambda_{\bar{h}\,i,j}^{n} \delta h_{i,j}^{n-1} = -\sum_{n=1}^{N-1} \sum_{i=2}^{IM-1} \sum_{j=2}^{JM-1} \lambda_{\bar{h}\,i,j}^{n+1} \delta h_{i,j}^{n}$$

$$T35 = -0.5\beta \sum_{n=2}^{N} \sum_{i=2}^{IM-1} \sum_{j=2}^{JM-1} \lambda_{\bar{h}\,i,j}^{n} \delta h_{i,j}^{n}$$

$$T36 = -0.5\beta \sum_{n=2}^{N} \sum_{i=2}^{IM-1} \sum_{j=2}^{JM-1} \lambda_{\bar{h}\,i,j}^{n} \delta \bar{h}_{i,j}^{n-1} = -0.5\beta \sum_{n=1}^{N-1} \sum_{i=2}^{IM-1} \sum_{j=2}^{JM-1} \lambda_{\bar{h}\,i,j}^{n+1} \delta \bar{h}_{i,j}^{n}$$

$$T37 = \beta \sum_{n=2}^{N} \sum_{i=2}^{IM-1} \sum_{j=2}^{JM-1} \lambda_{\bar{h}\,i,j}^{n} \delta h_{i,j}^{n-1} = \beta \sum_{n=1}^{N-1} \sum_{i=2}^{IM-1} \sum_{j=2}^{JM-1} \lambda_{\bar{h}\,i,j}^{n+1} \delta h_{i,j}^{n}$$

$$T38 = \sum_{n=2}^{N} \sum_{i=2}^{IM-1} \sum_{j=2}^{JM-1} \lambda_{\bar{u}\,i,j}^{n} \delta \bar{U}_{i,j}^{n}$$

$$T39 = -\sum_{n=2}^{N} \sum_{i=2}^{IM-1} \sum_{j=2}^{JM-1} \lambda_{\bar{u}\,i,j}^{n} \delta U_{i,j}^{n-1} = -\sum_{n=1}^{N-1} \sum_{i=2}^{IM-1} \sum_{j=2}^{JM-1} \lambda_{\bar{u}\,i,j}^{n+1} \delta U_{i,j}^{n}$$

$$T40 = -0.5\beta \sum_{n=2}^{N} \sum_{i=2}^{IM-1} \sum_{j=2}^{JM-1} \lambda_{\bar{u}\,i,j}^{n} \delta U_{i,j}^{n}$$

$$T41 = -0.5\beta \sum_{n=2}^{N} \sum_{i=2}^{IM-1} \sum_{j=2}^{JM-1} \lambda_{\bar{u}\,i,j}^{n} \delta \bar{U}_{i,j}^{n-1} = -0.5\beta \sum_{n=1}^{N-1} \sum_{i=2}^{IM-1} \sum_{j=2}^{JM-1} \lambda_{\bar{u}\,i,j}^{n+1} \delta \bar{U}_{i,j}^{n}$$

$$T42 = \beta \sum_{n=2}^{N} \sum_{i=2}^{IM-1} \sum_{j=2}^{JM-1} \lambda_{\bar{u}\,i,j}^{n} \delta U_{i,j}^{n-1} = \beta \sum_{n=1}^{N-1} \sum_{i=2}^{IM-1} \sum_{j=2}^{JM-1} \lambda_{\bar{u}\,i,j}^{n+1} \delta U_{i,j}^{n}$$

$$T43 = \sum_{n=2}^{N} \sum_{i=2}^{IM-1} \sum_{j=2}^{JM-1} \lambda_{\bar{v}\,i,j}^{n} \delta \bar{V}_{i,j}^{n}$$

$$T44 = -\sum_{n=2}^{N} \sum_{i=2}^{IM-1} \sum_{j=2}^{JM-1} \lambda_{\bar{v}\,i,j}^{n} \delta V_{i,j}^{n-1} = -\sum_{n=1}^{N-1} \sum_{i=2}^{IM-1} \sum_{j=2}^{JM-1} \lambda_{\bar{v}\,i,j}^{n+1} \delta V_{i,j}^{n}$$

$$T45 = -0.5\beta \sum_{n=2}^{N} \sum_{i=2}^{IM-1} \sum_{j=2}^{JM-1} \lambda_{\bar{v}\,i,j}^{n} \delta V_{i,j}^{n}$$

$$T46 = -0.5\beta \sum_{n=2}^{N} \sum_{i=2}^{IM-1} \sum_{j=2}^{JM-1} \lambda_{\bar{v}\,i,j}^{n} \delta \bar{V}_{i,j}^{n-1} = -0.5\beta \cdot \sum_{n=1}^{N-1} \sum_{i=2}^{IM-1} \sum_{j=2}^{JM-1} \lambda_{\bar{v}\,i,j}^{n+1} \delta \bar{V}_{i,j}^{n}$$

$$T47 = \beta \cdot \sum_{n=2}^{N} \sum_{i=2}^{IM-1} \sum_{j=2}^{JM-1} \lambda_{\bar{v}\,i,j}^{n} \delta V_{i,j}^{n-1} = \beta \cdot \sum_{n=1}^{N-1} \sum_{i=2}^{IM-1} \sum_{j=2}^{JM-1} \lambda_{\bar{v}\,i,j}^{n+1} \delta V_{i,j}^{n}$$

APPENDIX B. VARIATIONAL OF THE NONLINEAR TERMS

$$\begin{aligned}
\delta F_{1i,j} = {} & \frac{U_{i+1,j}^{n-1} + U_{i,j}^{n-1}}{8}\left[(H_{i+1,j} + H_{i,j})\delta U_{i+1,j}^{n-1} + (H_{i,j} + H_{i-1,j})\delta U_{i,j}^{n-1}\right] \\
& + \frac{1}{8}\left[(H_{i+1,j} + H_{i,j})U_{i+1,j}^{n-1} + (H_{i,j} + H_{i-1,j})U_{i,j}^{n-1}\right](\delta U_{i+1,j}^{n-1} + \delta U_{i,j}^{n-1}) \\
& - \frac{2H_{i,j}A_M}{\Delta x_{i,j}}(\delta \overline{U}_{i+1,j}^{n-1} - \delta \overline{U}_{i,j}^{n-1}) \\
= {} & \frac{1}{8}\left[(H_{i+1,j} + H_{i,j})U_{i+1,j}^{n-1} + (H_{i,j} + H_{i-1,j})U_{i,j}^{n-1} + (U_{i+1,j}^{n-1} + U_{i,j}^{n-1})(H_{i+1,j} + H_{i,j})\right]\delta U_{i+1,j}^{n-1} \\
& + \frac{1}{8}\left[(H_{i+1,j} + H_{i,j})U_{i+1,j}^{n-1} + (H_{i,j} + H_{i-1,j})U_{i,j}^{n-1} + (U_{i+1,j}^{n-1} + U_{i,j}^{n-1})(H_{i,j} + H_{i-1,j})\right]\delta U_{i,j}^{n-1} \\
& - \frac{2H_{i,j}A_M}{\Delta x_{i,j}}\delta \overline{U}_{i+1,j}^{n-1} \\
& + \frac{2H_{i,j}A_M}{\Delta x_{i,j}}\delta \overline{U}_{i,j}^{n-1}
\end{aligned} \tag{B.1}$$

$$\begin{aligned}
\delta F_{2i,j} = {} & \frac{U_{i,j}^{n-1} + U_{i,j-1}^{n-1}}{8}(H_{i,j} + H_{i,j-1})\delta V_{i,j}^{n-1} \\
& + \frac{U_{i,j}^{n-1} + U_{i,j-1}^{n-1}}{8}(H_{i-1,j} + H_{i-1,j-1})\delta V_{i-1,j}^{n-1} \\
& + \frac{1}{8}\left[(H_{i,j} + H_{i,j-1})V_{i,j}^{n-1} + (H_{i-1,j} + H_{i-1,j-1})V_{i-1,j}^{n-1}\right]\delta U_{i,j}^{n-1} \\
& + \frac{1}{8}\left[(H_{i,j} + H_{i,j-1})V_{i,j}^{n-1} + (H_{i-1,j} + H_{i-1,j-1})V_{i-1,j}^{n-1}\right]\delta U_{i,j-1}^{n-1}
\end{aligned} \tag{B.2}$$

$$\delta F_{3i,j} = \frac{\overline{H}_{i,j}\overline{A}_M}{\Delta \overline{y}_{i,j}}\delta \overline{U}_{i,j}^{n-1} - \frac{\overline{H}_{i,j}\overline{A}_M}{\Delta \overline{y}_{i,j}}\delta \overline{U}_{i,j-1}^{n-1} + \frac{\overline{H}_{i,j}\overline{A}_M}{\Delta \overline{x}_{i,j}}\delta \overline{V}_{i,j}^{n-1} - \frac{\overline{H}_{i,j}\overline{A}_M}{\Delta \overline{x}_{i,j}}\delta \overline{V}_{i-1,j}^{n-1} \tag{B.3}$$

$$\begin{aligned}
\delta F_{4i,j} = {} & \frac{V_{i-1,j}^{n-1} + V_{i,j}^{n-1}}{8}(H_{i,j} + H_{i-1,j})\delta U_{i,j}^{n-1} \\
& + \frac{V_{i-1,j}^{n-1} + V_{i,j}^{n-1}}{8}(H_{i,j-1} + H_{i-1,j-1})\delta U_{i,j-1}^{n-1} \\
& + \frac{1}{8}\left[(H_{i,j} + H_{i-1,j})U_{i,j}^{n-1} + (H_{i,j-1} + H_{i-1,j-1})U_{i,j-1}^{n-1}\right]\delta V_{i-1,j}^{n-1} \\
& + \frac{1}{8}\left[(H_{i,j} + H_{i-1,j})U_{i,j}^{n-1} + (H_{i,j-1} + H_{i-1,j-1})U_{i,j-1}^{n-1}\right]\delta V_{i,j}^{n-1}
\end{aligned} \tag{B.4}$$

$$\begin{aligned}
\delta F_{5_{i,j}} &= \frac{V_{i,j+1}^{n-1}+V_{i,j}^{n-1}}{8}\left((H_{i,j+1}+H_{i,j})\delta V_{i,j+1}^{n-1}+(H_{i,j}+H_{i,j-1})\delta V_{i,j}^{n-1}\right)\\
&\quad +\frac{1}{8}\left[(H_{i,j+1}+H_{i,j})V_{i,j+1}^{n-1}+(H_{i,j}+H_{i,j-1})V_{i,j}^{n-1}\right]\left(\delta V_{i,j+1}^{n-1}+\delta V_{i,j}^{n-1}\right)\\
&\quad -2H_{i,j}A_M\,\frac{\delta\overline{V}_{i,j+1}^{n-1}-\delta\overline{V}_{i,j}^{n-1}}{\Delta y_{i,j}}\\
&= \frac{1}{8}\left[(H_{i,j+1}+H_{i,j})V_{i,j+1}^{n-1}+(H_{i,j}+H_{i,j-1})V_{i,j}^{n-1}+(V_{i,j+1}^{n-1}+V_{i,j}^{n-1})(H_{i,j}+H_{i,j-1})\right]\delta V_{i,j}^{n-1}\\
&\quad +\frac{1}{8}\left[(H_{i,j+1}+H_{i,j})V_{i,j+1}^{n-1}+(H_{i,j}+H_{i,j-1})V_{i,j}^{n-1}+(V_{i,j+1}^{n-1}+V_{i,j}^{n-1})(H_{i,j+1}+H_{i,j})\right]\delta V_{i,j+1}^{n-1}\\
&\quad -\frac{2H_{i,j}A_M}{\Delta y_{i,j}}\,\delta\overline{V}_{i,j+1}^{n-1}\\
&\quad +\frac{2H_{i,j}A_M}{\Delta y_{i,j}}\,\delta\overline{V}_{i,j}^{n-1}
\end{aligned} \tag{B.5}$$

$$\begin{aligned}
\delta F_{6_{i,j}} &= \frac{\Delta y_{i+1,j}-\Delta y_{i-1,j}}{4\Delta x\Delta y}\,\delta V_{i,j+1}^{n-1}+\frac{\Delta y_{i+1,j}-\Delta y_{i-1,j}}{4\Delta x\Delta y}\,\delta V_{i,j}^{n-1}\\
&\quad -\frac{\Delta x_{i,j+1}-\Delta x_{i,j-1}}{4\Delta x\Delta y}\,\delta U_{i+1,j}^{n-1}-\frac{\Delta x_{i,j+1}-\Delta x_{i,j-1}}{4\Delta x\Delta y}\,\delta U_{i,j}^{n-1}]
\end{aligned} \tag{B.6}$$

$$\begin{aligned}
\delta F_{x_{i,j}} &= \delta F_{1_{i,j}}\Delta y_{i,j}-\delta F_{1_{i-1,j}}\Delta y_{i-1,j}+(\delta F_{2_{i,j+1}}-\delta F_{3_{i,j+1}})\Delta\overline{x}_{i,j+1}-(\delta F_{2_{i,j}}-\delta F_{3_{i,j}})\Delta\overline{x}_{i,j}\\
&\quad -\frac{ARU_{i,j}}{4}\left[\delta F_{6_{i,j}}H_{i,j}\left(V_{i,j+1}^{n-1}+V_{i,j}^{n-1}\right)+\delta F_{6_{i-1,j}}H_{i-1,j}\left(V_{i-1,j+1}^{n-1}+V_{i-1,j}^{n-1}\right)\right]\\
&\quad -\frac{ARU_{i,j}}{4}\left[F_{6_{i,j}}H_{i,j}\left(\delta V_{i,j+1}^{n-1}+\delta V_{i,j}^{n-1}\right)+F_{6_{i-1,j}}H_{i-1,j}\left(\delta V_{i-1,j+1}^{n-1}+\delta V_{i-1,j}^{n-1}\right)\right]
\end{aligned} \tag{B.7}$$

$$\begin{aligned}
\delta F_{y_{i,j}} &= \delta F_{5_{i,j}}\Delta x_{i,j}-\delta F_{5_{i,j-1}}\Delta x_{i,j-1}+(\delta F_{4_{i+1,j}}-\delta F_{3_{i+1,j}})\Delta\overline{y}_{i+1,j}-(\delta F_{4_{i,j}}-\delta F_{3_{i,j}})\Delta\overline{y}_{i,j}\\
&\quad +\frac{ARV_{i,j}}{4}\left[\delta F_{6_{i,j}}H_{i,j}\left(U_{i+1,j}^{n-1}+U_{i,j}^{n-1}\right)+\delta F_{6_{i,j-1}}H_{i,j-1}\left(U_{i+1,j-1}^{n-1}+U_{i,j-1}^{n-1}\right)\right]\\
&\quad +\frac{ARV_{i,j}}{4}\left[F_{6_{i,j}}H_{i,j}\left(\delta U_{i+1,j}^{n-1}+\delta U_{i,j}^{n-1}\right)+F_{6_{i,j-1}}H_{i,j-1}\left(\delta U_{i+1,j-1}^{n-1}+\delta U_{i,j-1}^{n-1}\right)\right]
\end{aligned} \tag{B.8}$$

$$
\begin{aligned}
&\sum_{n=2}^{N}\sum_{i=2}^{IM-1}\sum_{j=2}^{JM-1} L_{i,j}\lambda_{u_{i,j}}^{n}\delta F_{x_{i,j}} = \\
&\quad \sum_{n=2}^{N}\sum_{i=2}^{IM-1}\sum_{j=2}^{JM-1}(L_{i,j}\lambda_{u_{i,j}}^{n} - L_{i+1,j}\lambda_{u_{i+1,j}}^{n})\Delta y_{i,j}\delta F_{1_{i,j}} \\
&\quad + \sum_{n=2}^{N}\sum_{i=2}^{IM-1}\sum_{j=3}^{JM-1}(L_{i,j-1}\lambda_{u_{i,j-1}}^{n} - L_{i,j}\lambda_{u_{i,j}}^{n})\Delta \overline{x}_{i,j}\delta F_{2_{i,j}} - \sum_{n=2}^{N}\sum_{i=2}^{IM-1} L_{i,2}\lambda_{u_{i,2}}^{n}\Delta \overline{x}_{i,2}\delta F_{2_{i,2}} \\
&\quad - \sum_{n=2}^{N}\sum_{i=2}^{IM-1}\sum_{j=3}^{JM-1}(L_{i,j-1}\lambda_{u_{i,j-1}}^{n} - L_{i,j}\lambda_{u_{i,j}}^{n})\Delta \overline{x}_{i,j}\delta F_{3_{i,j}} + \sum_{n=2}^{N}\sum_{i=2}^{IM-1} L_{i,2}\lambda_{u_{i,2}}^{n}\Delta \overline{x}_{i,j}\delta F_{3_{i,2}} \\
&\quad - \sum_{n=2}^{N}\sum_{i=2}^{IM-1}\sum_{j=2}^{JM-1} \frac{L_{i,j}\lambda_{u_{i,j}}^{n} ARU_{i,j} + L_{i+1,j}\lambda_{u_{i+1,j}}^{n} ARU_{i+1,j}}{4} H_{i,j}\left(V_{i,j+1}^{n-1} + V_{i,j}^{n-1}\right)\delta F_{6_{i,j}} \\
&\quad - \sum_{n=1}^{N-1}\sum_{i=2}^{IM-1}\sum_{j=3}^{JM} \frac{L_{i,j-1}\lambda_{u_{i,j-1}}^{n+1} ARU_{i,j-1}}{4} F_{6_{i,j-1}} H_{i,j-1}\delta V_{i,j}^{n} \\
&\quad - \sum_{n=1}^{N-1}\sum_{i=1}^{IM-2}\sum_{j=3}^{JM} \frac{L_{i+1,j-1}\lambda_{u_{i+1,j-1}}^{n+1} ARU_{i+1,j-1}}{4} F_{6_{i,j-1}} H_{i,j-1}\delta V_{i,j}^{n} \\
&\quad - \sum_{n=1}^{N-1}\sum_{i=2}^{IM-1}\sum_{j=2}^{JM-1} \frac{L_{i,j}\lambda_{u_{i,j}}^{n+1} ARU_{i,j}}{4} F_{6_{i,j}} H_{i,j}\delta V_{i,j}^{n} \\
&\quad - \sum_{n=1}^{N-1}\sum_{i=1}^{IM-2}\sum_{j=2}^{JM-1} \frac{L_{i+1,j}\lambda_{u_{i+1,j}}^{n+1} ARU_{i+1,j}}{4} F_{6_{i,j}} H_{i,j}\delta V_{i,j}^{n}
\end{aligned}
\tag{B.9}
$$

$$
\begin{aligned}
&\sum_{n=2}^{N}\sum_{i=2}^{IM-1}\sum_{j=3}^{JM-1} M_{i,j}\lambda_{v_{i,j}}^{n}\delta F_{y_{i,j}} = \\
&\quad \sum_{n=2}^{N}\sum_{i=2}^{IM-1}\sum_{j=3}^{JM-1}(M_{i,j}\lambda_{v_{i,j}}^{n} - M_{i,j+1}\lambda_{v_{i,j+1}}^{n})\Delta x_{i,j}\delta F_{5_{i,j}} - \sum_{n=2}^{N}\sum_{i=2}^{IM-1} M_{i,3}\lambda_{v_{i,3}}^{n}\Delta x_{i,2}\delta F_{5_{i,2}} \\
&\quad + \sum_{n=2}^{N}\sum_{i=2}^{IM}\sum_{j=3}^{JM-1}(M_{i-1,j}\lambda_{v_{i-1,j}}^{n} - M_{i,j}\lambda_{v_{i,j}}^{n})\Delta \overline{y}_{i,j}\delta F_{4_{i,j}} \\
&\quad - \sum_{n=2}^{N}\sum_{i=2}^{IM-1}\sum_{j=3}^{JM-1}(M_{i-1,j}\lambda_{v_{i-1,j}}^{n} - M_{i,j}\lambda_{v_{i,j}}^{n})\Delta \overline{y}_{i,j}\delta F_{3_{i,j}} \\
&\quad + \sum_{n=2}^{N}\sum_{i=2}^{IM-1}\sum_{j=3}^{JM-1} \frac{M_{i,j}\lambda_{v_{i,j}}^{n} ARV_{i,j} + M_{i,j+1}\lambda_{v_{i,j+1}}^{n} ARV_{i,j+1}}{4} H_{i,j}\left(U_{i+1,j}^{n-1} + U_{i,j}^{n-1}\right)\delta F_{6_{i,j}} \\
&\quad + \sum_{n=2}^{N}\sum_{i=2}^{IM-1} M_{i,3}\lambda_{v_{i,3}}^{n}\frac{ARV_{i,3}}{4} H_{i,2}\left(U_{i+1,2}^{n-1} + U_{i,2}^{n-1}\right)\delta F_{6_{i,2}} \\
&\quad + \sum_{n=1}^{N-1}\sum_{i=3}^{IM}\sum_{j=3}^{JM-1} M_{i-1,j}\lambda_{v_{i-1,j}}^{n+1}\frac{ARV_{i-1,j}}{4} F_{6_{i-1,j}} H_{i-1,j}\delta U_{i,j}^{n} \\
&\quad + \sum_{n=1}^{N-1}\sum_{i=2}^{IM-1}\sum_{j=3}^{JM-1} M_{i,j}\lambda_{v_{i,j}}^{n+1}\frac{ARV_{i,j}}{4} F_{6_{i,j}} H_{i,j}\delta U_{i,j}^{n} \\
&\quad + \sum_{n=2}^{N}\sum_{i=3}^{IM}\sum_{j=2}^{JM-2} M_{i-1,j+1}\lambda_{v_{i-1,j+1}}^{n+1}\frac{ARV_{i-1,j+1}}{4} F_{6_{i-1,j}} H_{i-1,j}\delta U_{i,j}^{n} \\
&\quad + \sum_{n=1}^{N-1}\sum_{i=2}^{IM-1}\sum_{j=2}^{JM-2} M_{i,j+1}\lambda_{v_{i,j+1}}^{n+1}\frac{ARV_{i,j+1}}{4} F_{6_{i,j}} H_{i,j}\delta U_{i,j}^{n}
\end{aligned}
\tag{B.10}
$$

Inserting Eqn. (B.1) - (B.8) into Eqn. (B.9) and (B.10), $\Psi_{\text{nonlinear terms}}$ are derived from the nonlinear horizontal advection and diffusion terms in Eqn. (3.6) as,

$\Psi_{\text{nonlinear term}} =$

$$
\begin{aligned}
&\sum_{n=2}^{N}\sum_{i=2}^{IM-1}\sum_{j=2}^{JM-1} L_{i,j}\lambda_{u i,j}^{n}\delta F_{x i,j} + \sum_{n=3}^{N}\sum_{i=2}^{IM-1}\sum_{j=2}^{JM-1} M_{i,j}\lambda_{v i,j}^{n}\delta F_{y_{i,j}} \\
&= \sum_{n=1}^{N-1}\sum_{i=2}^{IM-1}\sum_{j=2}^{JM-1} (L_{i,j}\lambda_{u i,j}^{n+1} - L_{i+1,j}\lambda_{u i+1,j}^{n+1})\Delta y_{i,j}\frac{2H_{i,j}A_M}{\Delta x_{i,j}}\delta\overline{U}_{i,j}^{n} \\
&-\sum_{n=1}^{N-1}\sum_{i=3}^{IM-1}\sum_{j=2}^{JM-1} (L_{i-1,j}\lambda_{u i-1,j}^{n+1} - L_{i,j}\lambda_{u i,j}^{n+1})\Delta y_{i-1,j}\frac{2H_{i-1,j}A_M}{\Delta x_{i-1,j}}\delta\overline{U}_{i,j}^{n} \\
&-\sum_{n=1}^{N-1}\sum_{i=2}^{IM-1}\sum_{j=3}^{JM-1} (L_{i,j-1}\lambda_{u i,j-1}^{n+1} - L_{i,j}\lambda_{u i,j}^{n+1})\Delta \overline{x}_{i,j}\frac{\overline{H}_{i,j}A_M}{\Delta \overline{y}_{i,j}}\delta\overline{U}_{i,j}^{n} \\
&+\sum_{n=1}^{N-1}\sum_{i=2}^{IM-1}\sum_{j=2}^{JM-1} (L_{i,j}\lambda_{u i,j}^{n+1} - L_{i,j+1}\lambda_{u i,j+1}^{n+1})\Delta \overline{x}_{i,j+1}\frac{\overline{H}_{i,j+1}A_M}{\Delta \overline{y}_{i,j+1}}\delta\overline{U}_{i,j}^{n} \\
&-\sum_{n=1}^{N-1}\sum_{i=2}^{IM-1}\sum_{j=3}^{JM-1} (M_{i-1,j}\lambda_{v i-1,j}^{n+1} - M_{i,j}\lambda_{v i,j}^{n+1})\Delta \overline{y}_{i,j}\frac{\overline{H}_{i,j}A_M}{\Delta \overline{y}_{i,j}}\delta\overline{U}_{i,j}^{n} \\
&+\sum_{n=1}^{N-1}\sum_{i=2}^{IM-1}\sum_{j=2}^{JM-2} (M_{i-1,j+1}\lambda_{v i-1,j+1}^{n+1} - M_{i,j+1}\lambda_{v i,j+1}^{n+1})\Delta \overline{y}_{i,j+1}\frac{\overline{H}_{i,j+1}A_M}{\Delta \overline{y}_{i,j+1}}\delta\overline{U}_{i,j}^{n} \\
&+\sum_{n=1}^{N-1}\sum_{i=2}^{IM-1} L_{i,2}\lambda_{u i,2}^{n+1}\Delta \overline{x}_{i,2}\frac{\overline{H}_{i,2}\overline{A}_M}{\Delta \overline{y}_{i,2}}\delta\overline{U}_{i,2}^{n} - \sum_{n=2}^{N}\sum_{i=2}^{IM-1} L_{i,2}\lambda_{u i,2}^{n+1}\Delta \overline{x}_{i,2}\frac{\overline{H}_{i,2}\overline{A}_M}{\Delta \overline{y}_{i,2}}\delta\overline{U}_{i,1}^{n} \\
&-\sum_{n=1}^{N-1}\sum_{i=2}^{IM-1}\sum_{j=3}^{JM-1} (L_{i,j-1}\lambda_{u i,j-1}^{n+1} - L_{i,j}\lambda_{u i,j}^{n+1})\Delta \overline{x}_{i,j}\frac{\overline{H}_{i,j}A_M}{\Delta \overline{x}_{i,j}}\delta\overline{V}_{i,j}^{n} \\
&+\sum_{n=1}^{N-1}\sum_{i=1}^{IM-2}\sum_{j=3}^{JM-1} (L_{i+1,j-1}\lambda_{u i+1,j-1}^{n+1} - L_{i+1,j}\lambda_{u i+1,j}^{n+1})\Delta \overline{x}_{i+1,j}\frac{\overline{H}_{i+1,j}A_M}{\Delta \overline{x}_{i+1,j}}\delta\overline{V}_{i,j}^{n} \\
&-\sum_{n=1}^{N-1}\sum_{i=2}^{IM-2}\sum_{j=4}^{JM} (M_{i,j-1}\lambda_{v i,j-1}^{n+1} - M_{i,j}\lambda_{v i,j}^{n+1})\Delta x_{i,j-1}\frac{2H_{i,j-1}A_M}{\Delta y_{i,j-1}}\delta\overline{V}_{i,j}^{n} \\
&+\sum_{n=1}^{N-1}\sum_{i=2}^{IM-1}\sum_{j=3}^{JM-1} (M_{i,j}\lambda_{v i,j}^{n+1} - M_{i,j+1}\lambda_{v i,j+1}^{n+1})\Delta x_{i,j}\frac{2H_{i,j}A_M}{\Delta y_{i,j}}\delta\overline{V}_{i,j}^{n} \\
&-\sum_{n=1}^{N-1}\sum_{i=2}^{IM-1}\sum_{j=3}^{JM-1} (M_{i-1,j}\lambda_{v i-1,j}^{n+1} - M_{i,j}\lambda_{v i,j}^{n+1})\Delta \overline{y}_{i,j}\frac{\overline{H}_{i,j}A_M}{\Delta \overline{x}_{i,j}}\delta\overline{V}_{i,j}^{n} \\
&+\sum_{n=1}^{N-1}\sum_{i=1}^{IM-2}\sum_{j=3}^{JM-1} (M_{i,j}\lambda_{v i,j}^{n+1} - M_{i+1,j}\lambda_{v i+1,j}^{n+1})\Delta \overline{y}_{i+1,j}\frac{\overline{H}_{i+1,j}A_M}{\Delta \overline{x}_{i+1,j}}\delta\overline{V}_{i,j}^{n} \\
&+\sum_{n=1}^{N-1}\sum_{i=2}^{IM-1} L_{i,2}\lambda_{u i,2}^{n+1}\Delta \overline{x}_{i,2}\frac{\overline{H}_{i,2}\overline{A}_M}{\Delta \overline{x}_{i,2}}\delta\overline{V}_{i,2}^{n} - \sum_{n=2}^{N}\sum_{i=1}^{IM-2} L_{i+1,2}\lambda_{u i+1,2}^{n+1})\Delta \overline{x}_{i+1,2}\frac{\overline{H}_{i+1,2}\overline{A}_M}{\Delta \overline{x}_{i+1,2}}\delta\overline{V}_{i,2}^{n}
\end{aligned}
\tag{B.11}
$$

$$+\sum_{n=1}^{N-1}\sum_{i=2}^{IM-1} M_{i,3}\lambda_{vi,3}^{n+1}\Delta x_{i,2}\frac{2H_{i,2}A_M}{\Delta y_{i,2}}\delta\overline{V}_{i,3}^{n}-\sum_{n=1}^{N-1}\sum_{i=2}^{IM-1} M_{i,3}\lambda_{vi,3}^{n+1}\Delta x_{i,2}\frac{2H_{i,2}A_M}{\Delta y_{i,2}}\delta\overline{V}_{i,2}^{n}$$

$$+\sum_{n=1}^{N-1}\sum_{i=3}^{IM-1}\sum_{j=2}^{JM-1}(L_{i-1,j}\lambda_{ui-1,j}^{n+1}-L_{i,j}\lambda_{ui,j}^{n+1})\Delta y_{i-1,j}\{\frac{1}{8}\left(\begin{array}{l}(H_{i,j}+H_{i-1,j})U_{i,j}^{n}+(H_{i-1,j}+H_{i-2,j})U_{i-1,j}^{n}+\\(U_{i,j}^{n}+U_{i-1,j}^{n})(H_{i,j}+H_{i-1,j})\end{array}\right)\delta U_{i,j}^{n}$$

$$+\sum_{n=1}^{N-1}\sum_{i=2}^{IM-2}\sum_{j=2}^{JM-1}(L_{i,j}\lambda_{ui,j}^{n+1}-L_{i+1,j}\lambda_{ui+1,j}^{n+1})\Delta y_{i,j}\{\frac{1}{8}\left(\begin{array}{l}(H_{i+1,j}+H_{i,j})U_{i+1,j}^{n}+\\(H_{i,j}+H_{i-1,j})U_{i,j}^{n}+(U_{i+1,j}^{n}+U_{i,j}^{n})(H_{i,j}+H_{i-1,j})\end{array}\right)\delta U_{i,j}^{n}$$

$$+\sum_{n=2}^{N}\sum_{i=2}^{IM-1}\sum_{j=3}^{JM-1}(L_{i,j-1}\lambda_{ui,j-1}^{n+1}-L_{i,j}\lambda_{ui,j}^{n+1})\Delta\overline{x}_{i,j}\frac{1}{8}[(H_{i,j}+H_{i,j-1})V_{i,j}^{n}+(H_{i-1,j}+H_{i-1,j-1})V_{i-1,j}^{n}]\delta U_{i,j}^{n}$$

$$+\sum_{n=2}^{N}\sum_{i=2}^{IM-1}\sum_{j=2}^{JM-2}(L_{i,j}\lambda_{ui,j}^{n+1}-L_{i,j+1}\lambda_{ui,j+1}^{n+1})\Delta\overline{x}_{i,j+1}\frac{1}{8}[(H_{i,j+1}+H_{i,j})V_{i,j+1}^{n}+(H_{i-1,j+1}+H_{i-1,j})V_{i-1,j+1}^{n}]\delta U_{i,j}^{n}$$

$$+\sum_{n=2}^{N}\sum_{i=3}^{IM}\sum_{j=2}^{JM-1}\frac{L_{i-1,j}\lambda_{ui-1,j}^{n+1}ARU_{i-1,j}+L_{i,j}\lambda_{ui,j}^{n+1}ARU_{i,j}}{4}H_{i-1,j}(V_{i-1,j+1}^{n}+V_{i-1,j}^{n})\frac{1}{4\Delta x_{i-1,j}\Delta y_{i-1,j}}(\Delta x_{i-1,j+1}-\Delta x_{i-1,j-1})\delta U_{i,j}^{n}$$

$$+\sum_{n=2}^{N}\sum_{i=2}^{IM-1}\sum_{j=2}^{JM-1}\frac{L_{i,j}\lambda_{ui,j}^{n+1}ARU_{i,j}+L_{i+1,j}\lambda_{ui+1,j}^{n+1}ARU_{i+1,j}}{4}H_{i,j}(V_{i,j+1}^{n}+V_{i,j}^{n})\frac{1}{4\Delta x_{i,j}\Delta y_{i,j}}(\Delta x_{i,j+1}-\Delta x_{i,j-1})\delta U_{i,j}^{n}$$

$$+\sum_{n=1}^{N-1}\sum_{i=2}^{IM-1}\sum_{j=3}^{JM-1}(M_{i-1,j}\lambda_{vi-1,j}^{n+1}-M_{i,j}\lambda_{vi,j}^{n+1})\Delta\overline{y}_{i,j}\frac{V_{i-1,j}^{n}+V_{i,j}^{n}}{8}\left(H_{i,j}+H_{i-1,j}\right)\delta U_{i,j}^{n}$$

$$+\sum_{n=1}^{N-1}\sum_{i=2}^{IM-1}\sum_{j=2}^{JM-2}(M_{i-1,j+1}\lambda_{vi-1,j+1}^{n+1}-M_{i,j+1}\lambda_{vi,j+1}^{n+1})\Delta\overline{y}_{i,j+1}\frac{V_{i-1,j+1}^{n}+V_{i,j+1}^{n}}{8}\left(H_{i,j}+H_{i-1,j}\right)\delta U_{i,j}^{n}$$

$$-\sum_{n=1}^{N-1}\sum_{i=3}^{IM}\sum_{j=3}^{JM-1}\frac{M_{i-1,j}\lambda_{vi-1,j}^{n+1}ARV_{i-1,j}+M_{i-1,j+1}\lambda_{vi-1,j+1}^{n+1}ARV_{i-1,j+1}}{4}H_{i-1,j}(U_{i,j}^{n}+U_{i-1,j}^{n})\frac{1}{4\Delta x_{i-1,j}\Delta y_{i-1,j}}(\Delta x_{i-1,j+1}-\Delta x_{i-1,j-1})\delta U_{i,j}^{n}$$

$$-\sum_{n=2}^{N}\sum_{i=2}^{IM-1}\sum_{j=3}^{JM-1}\frac{M_{i,j}\lambda_{vi,j}^{n}ARV_{i,j}+M_{i,j+1}\lambda_{vi,j+1}^{n}ARV_{i,j+1}}{4}H_{i,j}(U_{i+1,j}^{n-1}+U_{i,j}^{n-1})\frac{1}{4\Delta x_{i,j}\Delta y_{i,j}}(\Delta x_{i,j+1}-\Delta x_{i,j-1})\delta U_{i,j}^{n}$$

$$+\sum_{n=1}^{N-1}\sum_{i=3}^{IM}\sum_{j=3}^{JM-1}M_{i-1,j}\lambda_{vi-1,j}^{n+1}\frac{ARV_{i-1,j}}{4}F_{6i-1,j}H_{i-1,j}\delta U_{i,j}^{n}$$

$$+\sum_{n=1}^{N-1}\sum_{i=2}^{IM-1}\sum_{j=3}^{JM-1}M_{i,j}\lambda_{vi,j}^{n+1}\frac{ARV_{i,j}}{4}F_{6i,j}H_{i,j}\delta U_{i,j}^{n}$$

$$+\sum_{n=2}^{N}\sum_{i=3}^{IM}\sum_{j=2}^{JM-2}M_{i-1,j+1}\lambda_{vi-1,j+1}^{n+1}\frac{ARV_{i-1,j+1}}{4}F_{6i-1,j}H_{i-1,j}\delta U_{i,j}^{n}$$

$$+\sum_{n=1}^{N-1}\sum_{i=2}^{IM-1}\sum_{j=2}^{JM-2}M_{i,j+1}\lambda_{vi,j+1}^{n+1}\frac{ARV_{i,j+1}}{4}F_{6i,j}H_{i,j}\delta U_{i,j}^{n}$$

$$-\sum_{n=2}^{N}\sum_{i=2}^{IM-1}L_{i,2}\lambda_{ui,2}^{n+1}\Delta\overline{x}_{i,2}\frac{1}{8}[(H_{i,2}+H_{i,1})V_{i,2}^{n}+(H_{i-1,2}+H_{i-1,1})V_{i-1,2}^{n}]\delta U_{i,2}^{n}$$

$$-\sum_{n=2}^{N}\sum_{i=2}^{IM-1}L_{i,2}\lambda_{ui,2}^{n+1}\Delta\overline{x}_{i,2}\frac{1}{8}[(H_{i,2}+H_{i,1})V_{i,2}^{n}+(H_{i-1,2}+H_{i-1,1})V_{i-1,2}^{n}]\delta U_{i,1}^{n}$$

$$-\sum_{n=2}^{N}\sum_{i=3}^{IM-1}\frac{M_{i-1,3}\lambda_{vi-1,3}^{n}ARV_{i-1,3}}{4}H_{i-1,2}(U_{i,2}^{n-1}+U_{i-1,2}^{n-1})\frac{1}{4\Delta x_{i-1,j}\Delta y_{i-1,j}}(\Delta x_{i-1,3}-\Delta x_{i-1,1})\delta U_{i,2}^{n}$$

$$-\sum_{n=2}^{N}\sum_{i=2}^{IM-1}\frac{M_{i,3}\lambda_{vi,3}^{n}ARV_{i,3}}{4}H_{i,2}(U_{i+1,2}^{n-1}+U_{i,2}^{n-1})\frac{1}{4\Delta x_{i,2}\Delta y_{i,2}}(\Delta x_{i,3}-\Delta x_{i,1})\delta U_{i,2}^{n}$$

$$+\sum_{n=1}^{N-1}\sum_{i=2}^{IM-1}\sum_{j=3}^{JM-1}(L_{i,j-1}\lambda_{ui,j-1}^{n+1}-L_{i,j}\lambda_{ui,j}^{n+1})\Delta\overline{x}_{i,j}\frac{U_{i,j}^{n}+U_{i,j-1}^{n}}{8}(H_{i,j}+H_{i,j-1})\delta V_{i,j}^{n}$$

$$+\sum_{n=2}^{N}\sum_{i=1}^{IM-2}\sum_{j=3}^{JM-1}(L_{i+1,j-1}\lambda_{ui+1,j-1}^{n+1}-L_{i+1,j}\lambda_{ui+1,j}^{n+1})\Delta\overline{x}_{i+1,j}\frac{U_{i+1,j}^{n}+U_{i+1,j-1}^{n}}{8}(H_{i,j}+H_{i,j-1})\delta V_{i,j}^{n}$$

$$-\sum_{n=2}^{N}\sum_{i=2}^{IM-1}\sum_{j=3}^{JM}\frac{L_{i,j-1}\lambda_{ui,j-1}^{n+1}ARU_{i,j-1}+L_{i+1,j-1}\lambda_{ui+1,j-1}^{n+1}ARU_{i+1,j-1}}{4}H_{i,j-1}(V_{i,j}^{n}+V_{i,j-1}^{n})\frac{1}{4\Delta x_{i,j-1}\Delta y_{i,j-1}}(\Delta y_{i+1,j-1}-\Delta y_{i-1,j-1})\delta V_{i,j}^{n}$$

$$-\sum_{n=2}^{N}\sum_{i=2}^{IM-1}\sum_{j=2}^{JM-1}\frac{L_{i,j}\lambda_{ui,j}^{n+1}ARU_{i,j}+L_{i+1,j}\lambda_{ui+1,j}^{n+1}ARU_{i+1,j}}{4}H_{i,j}(V_{i,j+1}^{n}+V_{i,j}^{n})\frac{1}{4\Delta x_{i,j}\Delta y_{i,j}}(\Delta y_{i+1,j}-\Delta y_{i-1,j})\delta V_{i,j}^{n}$$

$$+\sum_{n=1}^{N-1}\sum_{i=2}^{IM-1}\sum_{j=3}^{JM-1}(M_{i,j}\lambda_{vi,j}^{n+1}-M_{i,j+1}\lambda_{vi,j+1}^{n+1})\Delta x_{i,j}\{\frac{1}{8}\left(\begin{matrix}(H_{i,j+1}+H_{i,j})V_{i,j+1}^{n}+(H_{i,j}+H_{i,j-1})V_{i,j}^{n}+\\(V_{i,j+1}^{n}+V_{i,j}^{n})(H_{i,j}+H_{i,j-1})\end{matrix}\right)\}\delta V_{i,j}^{n}$$

$$+\sum_{n=1}^{N-1}\sum_{i=2}^{IM-2}\sum_{j=4}^{JM}(M_{i,j-1}\lambda_{vi,j-1}^{n+1}-M_{i,j}\lambda_{vi,j}^{n+1})\Delta x_{i,j-1}\{\frac{1}{8}\left(\begin{matrix}(H_{i,j}+H_{i,j-1})V_{i,j}^{n}+\\(H_{i,j-1}+H_{i,j-2})V_{i,j-1}^{n}+(V_{i,j}^{n}+V_{i,j-1}^{n})(H_{i,j}+H_{i,j-1})\end{matrix}\right)\}\delta V_{i,j}^{n}$$

$$+\sum_{n=1}^{N-1}\sum_{i=1}^{IM-2}\sum_{j=3}^{JM-1}(M_{i,j}\lambda_{vi,j}^{n+1}-M_{i+1,j}\lambda_{vi+1,j}^{n+1})\Delta\overline{y}_{i+1,j}\frac{1}{8}\Big((H_{i+1,j}+H_{i,j})U_{i+1,j}^{n}+(H_{i+1,j-1}+H_{i,j-1})U_{i+1,j-1}^{n}\Big)\delta V_{i,j}^{n}$$

$$+\sum_{n=1}^{N-1}\sum_{i=2}^{IM-1}\sum_{j=3}^{JM-1}(M_{i-1,j}\lambda_{vi-1,j}^{n+1}-M_{i,j}\lambda_{vi,j}^{n+1})\Delta\overline{y}_{i,j}\frac{1}{8}\Big((H_{i,j}+H_{i-1,j})U_{i,j}^{n}+(H_{i,j-1}+H_{i-1,j-1})U_{i,j-1}^{n}\Big)\delta V_{i,j}^{n}$$

$$+\sum_{n=1}^{N-1}\sum_{i=2}^{IM-1}\sum_{j=4}^{JM}\frac{M_{i,j-1}\lambda_{vi,j-1}^{n+1}ARV_{i,j-1}+M_{i,j}\lambda_{vi,j}^{n+1}ARV_{i,j}}{4}H_{i,j-1}(U_{i+1,j-1}^{n}+U_{i,j-1}^{n})\frac{1}{4\Delta x_{i,j-1}\Delta y_{i,j-1}}(\Delta y_{i+1,j-1}-\Delta y_{i-1,j-1})\delta V_{i,j}^{n}$$

$$+\sum_{n=1}^{N-1}\sum_{i=2}^{IM-1}\sum_{j=3}^{JM}\frac{M_{i,j}\lambda_{vi,j}^{n+1}ARV_{i,j}+M_{i,j+1}\lambda_{vi,j+1}^{n+1}ARV_{i,j+1}}{4}H_{i,j}(U_{i+1,j}^{n}+U_{i,j}^{n})\frac{1}{4\Delta x_{i,j}\Delta y_{i,j}}(\Delta y_{i+1,j}-\Delta y_{i-1,j})\delta V_{i,j}^{n}$$

$$-\sum_{n=1}^{N-1}\sum_{i=2}^{IM-1}\sum_{j=3}^{JM}\frac{L_{i,j-1}\lambda_{ui,j-1}^{n+1}ARU_{i,j-1}}{4}F_{6i,j-1}H_{i,j-1}\delta V_{i,j}^{n}$$

$$-\sum_{n=1}^{N-1}\sum_{i=2}^{IM-1}\sum_{j=2}^{JM-1}\frac{L_{i,j}\lambda_{ui,j}^{n+1}ARU_{i,j}}{4}F_{6i,j}H_{i,j}\delta V_{i,j}^{n}$$

$$-\sum_{n=1}^{N-1}\sum_{i=1}^{IM-2}\sum_{j=3}^{JM}\frac{L_{i+1,j-1}\lambda_{ui+1,j-1}^{n+1}ARU_{i+1,j-1}}{4}F_{6i,j-1}H_{i,j-1}\delta V_{i,j}^{n}$$

$$-\sum_{n=1}^{N-1}\sum_{i=2}^{IM-1}\sum_{j=2}^{JM-1}\frac{L_{i+1,j}\lambda_{ui+1,j}^{n+1}ARU_{i+1,j}}{4}F_{6i,j}H_{i,j}\delta V_{i,j}^{n}$$

$$-\sum_{n=1}^{N-1}\sum_{i=2}^{IM-1}L_{i,2}\lambda_{ui,2}^{n+1}\Delta\overline{x}_{i,2}\frac{U_{i,2}^{n}+U_{i,1}^{n}}{8}(H_{i,2}+H_{i,1})\delta V_{i,2}^{n}$$

$$-\sum_{n=2}^{N}\sum_{i=1}^{IM-2}L_{i+1,2}\lambda_{ui+1,2}^{n+1}\Delta\overline{x}_{i+1,2}\frac{U_{i+1,2}^{n}+U_{i+1,1}^{n}}{8}(H_{i,2}+H_{i,1})\delta V_{i,2}^{n}$$

$$-\sum_{n=1}^{N-1}\sum_{i=2}^{IM-1} M_{i,3}\lambda_{v\,i,3}^{n+1})\Delta x_{i,2}\frac{1}{8}\begin{pmatrix}(H_{i,3}+H_{i,2})V_{i,3}^{n}+(H_{i,2}+H_{i,1})V_{i,2}^{n}+\\(V_{i,3}^{n}+V_{i,2}^{n})(H_{i,2}+H_{i,1})\end{pmatrix}\delta V_{i,2}^{n}$$

$$-\sum_{n=1}^{N-1}\sum_{i=2}^{IM-2} M_{i,3}\lambda_{v\,i,3}^{n+1})\Delta x_{i,2}\frac{1}{8}\begin{pmatrix}(H_{i,2}+H_{i,1})V_{i,2}^{n}+\\(H_{i,3}+H_{i,2})V_{i,3}^{n}+(V_{i,3}^{n}+V_{i,2}^{n})(H_{i,3}+H_{i,2})\end{pmatrix}\delta V_{i,3}^{n}$$

$$+\sum_{n=2}^{N}\sum_{i=2}^{IM-1}\frac{M_{i,3}\lambda_{v\,i,3}^{\;n}ARV_{i,3}}{4}H_{i,2}(U_{i+1,2}^{n-1}+U_{i,2}^{n-1})\frac{1}{4\Delta x_{i,j}\Delta y_{i,j}}(\Delta y_{i+1,2}-\Delta y_{i-1,2})\delta V_{i,3}^{n}$$

$$+\sum_{n=2}^{N}\sum_{i=2}^{IM-1}\frac{M_{i,3}\lambda_{v\,i,3}^{\;n}ARV_{i,3}}{4}H_{i,2}(U_{i+1,2}^{n-1}+U_{i,2}^{n-1})\frac{1}{4\Delta x_{i,j}\Delta y_{i,j}}(\Delta y_{i+1,2}-\Delta y_{i-1,2})\delta V_{i,2}^{n}$$

APPENDIX C. COEFFICIENTS OF $F_{\bar{u}}$, $F_{\bar{v}}$, F_u, F_v

$$\begin{aligned}
F_{\bar{u}} = {} & (L_{i,j}\lambda_{u\,i,j}^{n+1} - L_{i+1,j}\lambda_{u\,i+1,j}^{n+1})\Delta y_{i,j}\frac{2H_{i,j}A_M}{\Delta x_{i,j}} - (L_{i-1,j}\lambda_{u\,i-1,j}^{n+1} - L_{i,j}\lambda_{u\,i,j}^{n+1})\Delta y_{i-1,j}\frac{2H_{i-1,j}A_M}{\Delta x_{i-1,j}} \\
& -(L_{i,j-1}\lambda_{u\,i,j-1}^{n+1} - L_{i,j}\lambda_{u\,i,j}^{n+1})\Delta\bar{x}_{i,j}\frac{\overline{H}_{i,j}A_M}{\Delta\bar{y}_{i,j}} + (L_{i,j}\lambda_{u\,i,j}^{n+1} - L_{i,j+1}\lambda_{u\,i,j+1}^{n+1})\Delta\bar{x}_{i,j+1}\frac{\overline{H}_{i,j+1}A_M}{\Delta\bar{y}_{i,j+1}} \\
& -(M_{i-1,j}\lambda_{v\,i-1,j}^{n+1} - M_{i,j}\lambda_{v\,i,j}^{n+1})\Delta\bar{y}_{i,j}\frac{\overline{H}_{i,j}A_M}{\Delta\bar{y}_{i,j}} + (M_{i-1,j+1}\lambda_{v\,i-1,j+1}^{n+1} - M_{i,j+1}\lambda_{v\,i,j+1}^{n+1})\Delta\bar{y}_{i,j+1}\frac{\overline{H}_{i,j+1}A_M}{\Delta\bar{y}_{i,j+1}}
\end{aligned} \tag{C.1}$$

$$\begin{aligned}
F_{\bar{v}} = {} & -(L_{i,j-1}\lambda_{u\,i,j-1}^{n+1} - L_{i,j}\lambda_{u\,i,j}^{n+1})\Delta\bar{x}_{i,j}\frac{\overline{H}_{i,j}A_M}{\Delta\bar{x}_{i,j}} + (L_{i+1,j-1}\lambda_{u\,i+1,j-1}^{n+1} - L_{i+1,j}\lambda_{u\,i+1,j}^{n+1})\Delta\bar{x}_{i+1,j}\frac{\overline{H}_{i+1,j}A_M}{\Delta\bar{x}_{i+1,j}} \\
& -(M_{i,j-1}\lambda_{v\,i,j-1}^{n+1} - M_{i,j}\lambda_{v\,i,j}^{n+1})\Delta x_{i,j-1}\frac{2H_{i,j-1}A_M}{\Delta y_{i,j-1}} + (M_{i,j}\lambda_{v\,i,j}^{n+1} - M_{i,j+1}\lambda_{v\,i,j+1}^{n+1})\Delta x_{i,j}\frac{2H_{i,j}A_M}{\Delta y_{i,j}} \\
& -(M_{i-1,j}\lambda_{v\,i-1,j}^{n+1} - M_{i,j}\lambda_{v\,i,j}^{n+1})\Delta\bar{y}_{i,j}\frac{\overline{H}_{i,j}A_M}{\Delta\bar{x}_{i,j}} + (M_{i,j}\lambda_{v\,i,j}^{n+1} - M_{i+1,j}\lambda_{v\,i+1,j}^{n+1})\Delta\bar{y}_{i+1,j}\frac{\overline{H}_{i+1,j}A_M}{\Delta\bar{x}_{i+1,j}}
\end{aligned} \tag{C.2}$$

$$\begin{aligned}
F_u = {} & (L_{i-1,j}\lambda_{u\,i-1,j}^{n+1} - L_{i,j}\lambda_{u\,i,j}^{n+1})\Delta y_{i-1,j}\{\frac{1}{8}\left(\begin{array}{l} (H_{i,j} + H_{i-1,j})U_{i,j}^n + (H_{i-1,j} + H_{i-2,j})U_{i-1,j}^n + \\ (U_{i,j}^n + U_{i-1,j}^n)(H_{i,j} + H_{i-1,j}) \end{array}\right) \\
& + (L_{i,j}\lambda_{u\,i,j}^{n+1} - L_{i+1,j}\lambda_{u\,i+1,j}^{n+1})\Delta y_{i,j}\{\frac{1}{8}\left(\begin{array}{l} (H_{i+1,j} + H_{i,j})U_{i+1,j}^n + \\ (H_{i,j} + H_{i-1,j})U_{i,j}^n + (U_{i+1,j}^n + U_{i,j}^n)(H_{i,j} + H_{i-1,j}) \end{array}\right)
\end{aligned} \tag{C.3}$$

$$\begin{aligned}
& +(L_{i,j-1}\lambda_{u\,i,j-1}^{n+1} - L_{i,j}\lambda_{u\,i,j}^{n+1})\Delta\bar{x}_{i,j}\frac{1}{8}[(H_{i,j} + H_{i,j-1})V_{i,j}^n + (H_{i-1,j} + H_{i-1,j-1})V_{i-1,j}^n] \\
& +(L_{i,j}\lambda_{u\,i,j}^{n+1} - L_{i,j+1}\lambda_{u\,i,j+1}^{n+1})\Delta\bar{x}_{i,j+1}\frac{1}{8}[(H_{i,j+1} + H_{i,j})V_{i,j+1}^n + (H_{i-1,j+1} + H_{i-1,j})V_{i-1,j+1}^n] \\
& +\frac{L_{i-1,j}\lambda_{u\,i-1,j}^{n+1}ARU_{i-1,j} + L_{i,j}\lambda_{u\,i,j}^{n+1}ARU_{i,j}}{4}H_{i-1,j}(V_{i-1,j+1}^n + V_{i-1,j}^n)\frac{1}{4\Delta x_{i-1,j}\Delta y_{i-1,j}}(\Delta x_{i-1,j+1} - \Delta x_{i-1,j-1}) \\
& +\frac{L_{i,j}\lambda_{u\,i,j}^{n+1}ARU_{i,j} + L_{i+1,j}\lambda_{u\,i+1,j}^{n+1}ARU_{i+1,j}}{4}H_{i,j}(V_{i,j+1}^n + V_{i,j}^n)\frac{1}{4\Delta x_{i,j}\Delta y_{i,j}}(\Delta x_{i,j+1} - \Delta x_{i,j-1}) \\
& +(M_{i-1,j}\lambda_{v\,i-1,j}^{n+1} - M_{i,j}\lambda_{v\,i,j}^{n+1})\Delta\bar{y}_{i,j}\frac{V_{i-1,j}^n + V_{i,j}^n}{8}(H_{i,j} + H_{i-1,j}) \\
& +(M_{i-1,j+1}\lambda_{v\,i-1,j+1}^{n+1} - M_{i,j+1}\lambda_{v\,i,j+1}^{n+1})\Delta\bar{y}_{i,j+1}\frac{V_{i-1,j+1}^n + V_{i,j+1}^n}{8}(H_{i,j} + H_{i-1,j})
\end{aligned}$$

$$
\begin{aligned}
&-\frac{M_{i-1,j}\lambda_{vi-1,j}^{n+1}ARV_{i-1,j}+M_{i-1,j+1}\lambda_{vi-1,j+1}^{n+1}ARV_{i-1,j+1}}{4}H_{i-1,j}(U_{i,j}^{n}+U_{i-1,j}^{n})\frac{1}{4\Delta x_{i-1,j}\Delta y_{i-1,j}}(\Delta x_{i-1,j+1}-\Delta x_{i-1,j-1})\\
&-\frac{M_{i,j}\lambda_{vi,j}^{n}ARV_{i,j}+M_{i,j+1}\lambda_{vi,j+1}^{n}ARV_{i,j+1}}{4}H_{i,j}(U_{i+1,j}^{n-1}+U_{i,j}^{n-1})\frac{1}{4\Delta x_{i,j}\Delta y_{i,j}}(\Delta x_{i,j+1}-\Delta x_{i,j-1})\\
&+M_{i-1,j}\lambda_{vi-1,j}^{n+1}\frac{ARV_{i-1,j}}{4}F_{6i-1,j}H_{i-1,j}+M_{i,j}\lambda_{vi,j}^{n+1}\frac{ARV_{i,j}}{4}F_{6i,j}H_{i,j}\\
&+M_{i-1,j+1}\lambda_{vi-1,j+1}^{n+1}\frac{ARV_{i-1,j+1}}{4}F_{6i-1,j}H_{i-1,j}+M_{i,j+1}\lambda_{vi,j+1}^{n+1}\frac{ARV_{i,j+1}}{4}F_{6i,j}H_{i,j}
\end{aligned}
$$

$$
\begin{aligned}
F_{v}={}&(L_{i,j-1}\lambda_{ui,j-1}^{n+1}-L_{i,j}\lambda_{ui,j}^{n+1})\Delta\bar{x}_{i,j}\frac{U_{i,j}^{n}+U_{i,j-1}^{n}}{8}(H_{i,j}+H_{i,j-1})\\
&+(L_{i+1,j-1}\lambda_{ui+1,j-1}^{n+1}-L_{i+1,j}\lambda_{ui+1,j}^{n+1})\Delta\bar{x}_{i+1,j}\frac{U_{i+1,j}^{n}+U_{i+1,j-1}^{n}}{8}(H_{i,j}+H_{i,j-1})\\
&-\frac{L_{i,j-1}\lambda_{ui,j-1}^{n+1}ARU_{i,j-1}+L_{i+1,j-1}\lambda_{ui+1,j-1}^{n+1}ARU_{i+1,j-1}}{4}H_{i,j-1}(V_{i,j}^{n}+V_{i,j-1}^{n})\frac{1}{4\Delta x_{i,j-1}\Delta y_{i,j-1}}(\Delta y_{i+1,j-1}-\Delta y_{i-1,j-1})\\
&-\frac{L_{i,j}\lambda_{ui,j}^{n+1}ARU_{i,j}+L_{i+1,j}\lambda_{ui+1,j}^{n+1}ARU_{i+1,j}}{4}H_{i,j}(V_{i,j+1}^{n}+V_{i,j}^{n})\frac{1}{4\Delta x_{i,j}\Delta y_{i,j}}(\Delta y_{i+1,j}-\Delta y_{i-1,j})\\
&+(M_{i,j}\lambda_{vi,j}^{n+1}-M_{i,j+1}\lambda_{vi,j+1}^{n+1})\Delta x_{i,j}\frac{1}{8}\begin{pmatrix}(H_{i,j+1}+H_{i,j})V_{i,j+1}^{n}+(H_{i,j}+H_{i,j-1})V_{i,j}^{n}+\\(V_{i,j+1}^{n}+V_{i,j}^{n})(H_{i,j}+H_{i,j-1})\end{pmatrix}\\
&+(M_{i,j-1}\lambda_{vi,j-1}^{n+1}-M_{i,j}\lambda_{vi,j}^{n+1})\Delta x_{i,j-1}\frac{1}{8}\begin{pmatrix}(H_{i,j}+H_{i,j-1})V_{i,j}^{n}+\\(H_{i,j-1}+H_{i,j-2})V_{i,j-1}^{n}+(V_{i,j}^{n}+V_{i,j-1}^{n})(H_{i,j}+H_{i,j-1})\end{pmatrix}\\
&+(M_{i,j}\lambda_{vi,j}^{n+1}-M_{i+1,j}\lambda_{vi+1,j}^{n+1})\Delta\bar{y}_{i+1,j}\frac{1}{8}\left((H_{i+1,j}+H_{i,j})U_{i+1,j}^{n}+(H_{i+1,j-1}+H_{i,j-1})U_{i+1,j-1}^{n}\right)\\
&+(M_{i-1,j}\lambda_{vi-1,j}^{n+1}-M_{i,j}\lambda_{vi,j}^{n+1})\Delta\bar{y}_{i,j}\frac{1}{8}\left((H_{i,j}+H_{i-1,j})U_{i,j}^{n}+(H_{i,j-1}+H_{i-1,j-1})U_{i,j-1}^{n}\right)\\
&+\frac{M_{i,j-1}\lambda_{vi,j-1}^{n+1}ARV_{i,j-1}+M_{i,j}\lambda_{vi,j}^{n+1}ARV_{i,j}}{4}H_{i,j-1}(U_{i+1,j-1}^{n}+U_{i,j-1}^{n})\frac{1}{4\Delta x_{i,j-1}\Delta y_{i,j-1}}(\Delta y_{i+1,j-1}-\Delta y_{i-1,j-1})\\
&+\frac{M_{i,j}\lambda_{vi,j}^{n+1}ARV_{i,j}+M_{i,j+1}\lambda_{vi,j+1}^{n+1}ARV_{i,j+1}}{4}H_{i,j}(U_{i+1,j}^{n}+U_{i,j}^{n})\frac{1}{4\Delta x_{i,j}\Delta y_{i,j}}(\Delta y_{i+1,j}-\Delta y_{i-1,j})\\
&-\frac{L_{i,j-1}\lambda_{ui,j-1}^{n+1}ARU_{i,j-1}}{4}F_{6i,j-1}H_{i,j-1}-\frac{L_{i,j}\lambda_{ui,j}^{n+1}ARU_{i,j}}{4}F_{6i,j}H_{i,j}\\
&-\frac{L_{i+1,j-1}\lambda_{ui+1,j-1}^{n+1}ARU_{i+1,j-1}}{4}F_{6i,j-1}H_{i,j-1}-\frac{L_{i+1,j}\lambda_{ui+1,j}^{n+1}ARU_{i+1,j}}{4}F_{6i,j}H_{i,j}=0
\end{aligned}
\tag{C.4}
$$